POLITECNICO

MILANO 1863

SCUOLA DI INGEGNERIA INDUSTRIALE
E DELL'INFORMAZIONE

Investigation of Laguerre expansion basis for modelling of bridge aeroelastic forces

TESI DI LAUREA MAGISTRALE IN
MECHANICAL ENGINEERING - INGEGNERIA MECCANICA

Author: **Giacomo Bacci**

Student ID: 10596221
Advisor: Prof. Tommaso Argentini (PoliMi)
Co-advisors: Prof. Ole Andre Øiseth (NTNU)
Academic Year: 2021-22

Abstract

Great progress has been made in recent years to develop aerodynamic models capable of reproducing suspended bridges dynamics behaviour with great accuracy. However, simplified and easy-to-evaluate models are still required for preliminary design and in reliability assessment of cable supported bridges.

The goal of the present work is to develop an effective linear model for the approximation of self-excited forces on bridge decks. The model is designed using a set of orthonormal Laguerre functions as basis to express the linear kernel of a Volterra series expansion for the aerodynamic forces.

A model training procedure is developed and tested on a first-order simulated system. Then, the strengths and weaknesses of the framework are explored on real data tests. The data used for testing are from the Norwegian University of Science and Technology wind tunnel in Trondheim, Norway.

The designed model is then compared with a well-established model for experimental data interpolation: the rational functions model. The Laguerre expansion model proved to be effective and capable of foreseeing wind action with similar performances to rational functions in time domain and for most of the tested frequency range in frequency domain. The force prediction model is then inserted in a simulated dynamic model of a deck section. With time series simulations the Laguerre model led to correct structural dynamic behaviour forecast, compared to classic identification methods. Agreement in the predicted instability limits was found comparing the use of the Laguerre model and rational functions model as force prediction frameworks.

Keywords: Aeroelasticity, Wind Engineering, Bridge aerodynamics, Linear model, Laguerre filters, Orthonormal functions, Aerodynamic forces, Flutter instability

Abstract in lingua italiana

Numerosi progressi sono stati fatti negli ultimi anni nello sviluppo di modelli aerodimici in grado di approssimare con precisione il comportamento dinamico di ponti sospesi. Nonostante ciò, rimane fondamentale la presenza di modelli semplificati e di facile calcolo per la fase di design preliminare e di analisi dell'affidabilità per progetti di ponti di grande luce. L'obbiettivo di questo progetto è quello di sviluppare un modello lineare e di semplice calcolo per la modellazione delle forze aeroelastiche. Ciò è stato realizzato utilizzando le funzioni ortonormali di Laguerre come base per esprimere l'espansione di Volterra, fermata al primo ordine, delle forze aerodinamiche.

É stata sviluppata una procedura di training del modello e testata su un sistema del primo ordine simulato.

In seguito i punti di forza e le debolezze dell'algoritmo sono state esplorate su un set di dati reali. I dati utilizzati provengono da test nella galleria del vento della Norwegian University of Science and Technology di Trondheim, in Norvegia.

Il modello identificato è poi stato paragonato con un modello normalmente utilizzato per interpolare i dati sperimentali: il modello delle rational functions. Il modello di espansione di Laguerre ha dato prova di essere in grado di prevedere in maniera efficace l'azione del vento sulla struttura, con prestazioni simili al modello delle rational functions nel tempo e per la maggior parte delle frequenze testate.

Il modello per la previsione delle forze aerodinamiche qui identificato è stato poi accoppiato con il modello dinamico completo di una sezione di ponte. Analizzato attraverso simulazioni nel tempo, il modello di Laguerre è stato in grado di fornire una previsione corretta del comportamento dinamico della struttura, in accordo con metodi di calcolo tradizionali. I limiti di stabilità calcolati sono in accordo con quelli trovati inserendo il modello delle rational functions come modello di calcolo delle forze aerodinamiche.

Parole chiave: Aeroelasticità, Ingegneria del vento, Ponti sospesi, Modello lineare, Filtri di Laguerre, Funzioni ortonormali, Forze aerodinamiche, instabilità flutter

Contents

Introduction

Wind-induced dynamic response is one of the major concerns in long-span bridge design. Self-excited forces acting on girder, cables and towers can induce vibrations that can damage or weaken the structure. Thus, the study of the interaction between bridge components and the wind has been an important research topic in structural engineering in recent years. Great progress has been done to develop models that can reproduce the bridge dynamic as accurate as possible. However, simplified models are still convenient for preliminary design when assessing the reliability of cable supported bridges. Self-excited forces on bridge decks are commonly modelled in frequency domain with experimentally determined aerodynamic derivatives that are function of reduced frequency and depend on the geometry of the girder [13, 17, 18]. The aerodynamic derivatives are usually determined by wind tunnel experiments on section models at discrete reduced frequencies. To have a continuous time representation and remove the dependency on frequency, the experimental data can be interpolated in the tested frequency range by a particular dynamic model. What is often done in literature is least-squares fitting a rational function model in frequency domain that is then expressed back in time domain via inverse Fourier transforming [13, 16]. However, this is not the only way of doing and alternative methods have been investigated to reduce computational effort or to better capture nonlinear behaviour of particular section geometries.

Skyvulstad et al. [20] investigated the use of a Volterra series model for nonlinear bridge aerodynamic modelling in time domain. A Volterra series can be imagined as a Taylor series expansion with a memory and it is used to construct a non-linear model that expands linear convolutions to higher order convolutions [25]. One problem with Volterra series model is the rapid increase of computational burden with the number of inputs, order of the kernels considered and memory length. To mitigate this issue one possibility is to use parameterized kernels expanded by basis functions with few coefficients. As innovation in bridge aerodynamic, Skyvulstad et al. [20] used Laguerrian expansion basis for Volterra kernels estimation. As shown in the following, the number of Laguerrian coefficients to be identified is independent on memory length, which can be set arbitrarily long. Moreover, Laguerrian filters are orthonormal functions and the filters coefficients become orthogonal

for white noise inputs, which makes the identification process better conditioned. Furthermore, these functions decay to zero, which is the case for most physical system impulse response functions. This property makes them also good low-pass filters that suppress higher-order noise making the kernels smoother than traditional identification methods.

In the cited work Laguerrian expansion technique is used to identify Volterra kernels to estimate nonlinear motion-induced forces on bridge profiles. The present work proposes to investigate the feasibility of a Volterra series model stopped at the first order.

Hence, the intention of the author is to verify the practicality of a linear model with the kernel estimated with a Laguerrian expansion basis to predict wind induced self-excited forces on bridge decks.

Once the linear Laguerrian model has been identified, its performance are evaluated comparing the results with the well established rational functions approximation model for bridge aerodynamics.

The theory needed for calculations is presented in Chapter 1. Then the work is introduced with a general overview of orthonormal functions used as expansion basis, the Laguerrian expansion model is introduced and the identification method is explained with a simple example on a first order system.

The model is tested on real data from state-of-the-art wind tunnel experiments carried out by Bergerud and Torød [1] in the wind tunnel of the Norwegian University of Science and Technology (NTNU). With these data the capability of the model to predict self-excited forces in time domain is checked, comparing the predicted force time history and the experimentally measured one. The possibility to identify an optimal calibration of the parametric model is verified checking how the goodness of the identification varies with the two model parameters: the number of filters considered and the filters decay factor. Furthermore, the presence of a possible dependency of the model on the girder geometry is investigated using experimental data from different sections tested in the experimental campaign. Moreover, the model forecasting performance is been analyzed in frequency domain, identifying the system transfer functions and comparing them with the experimentally derived aerodynamic derivatives.

The presented model has been then compared with the rational function model fitted to experimental data. The comparison has been done in time domain, and frequency domain, comparing their forecasting performances.

Finally, with numerical simulation of a two degrees of freedom (2 Dof) deck section, the use of the Laguerrian linear model for predicting aeroelastic dynamic behaviour of the girder has been investigated. The model has been also used to predict flutter stability limit and its prediction is compared with the one calculated with the rational functions model.

1 | Wind Induced Self-excited Forces

1.1. Quasi Steady Theory

Self-excited forces are generated by the motion of a body immersed in a flow of fluid. They can be described following two approaches: unsteady models, which take in to account how the motion of the structure itself influences the flow around it, and steady models, that use force coefficients measured on a static model.

The most important steady model is the Quasi Steady Theory (QST), that assumes that the aeroelastic forces on the girder are the same as the static forces measured in still air tests [16]. This theory correctly depicts the aerodynamic forces if the reduced velocity $V^* = \frac{V}{fB}$ is greater than 10 - 20. This means that the time B/V needed by a fluid particle, travelling at speed V, to move through the length of the bridge deck (B) is at least a tenth of the deck's vibration period $T = \frac{1}{f}$. According to QST the aerodynamic forces consisting in drag, lift and moment are expressed as:

$$
\begin{aligned}
F_D &= \frac{1}{2}\rho V_{Rel}^2 BL C_D(\alpha) \\
F_L &= \frac{1}{2}\rho V_{Rel}^2 BL C_L(\alpha) \\
M &= \frac{1}{2}\rho V_{Rel}^2 B^2 L C_M(\alpha)
\end{aligned}
\tag{1.1}
$$

Here the air density is ρ, B and L are the deck width and length respectively and α is the angle of attack: the angle between the wind relative velocity and the deck during its motion. The coefficients C_D, C_L, C_M are the static coefficients for drag, lift and moment respectively, function of the angle α between the relative velocity V_{Rel} and the deck. They can be determined with static wind tunnel experiments measuring the forces acting on the deck for different angles of attack and constant wind velocity. V_{Rel} represents the wind velocity relative to the deck, which can be computed taking into account the mean wind velocity (V_m), the deck velocity components ($\dot{x}, \dot{y}$) and the horizontal turbulence

component v and vertical turbulence component w. However, according to the choice of reference point for the measurement of the deck speed components, different relative velocities may be defined. Indeed, if a reference point P, distant B_1 from the centre G of the section is chosen, as in Figure 1.1, the relative velocity is defined as in Equation 1.2, and the angle of attack of the relative wind speed is defined as in Equation 1.3.

$$V_{Rel}^2 = (V_m + v - \dot{x})^2 + (w - \dot{y} - B_1\dot{\theta})^2 \tag{1.2}$$

$$\psi = tan^{-1}\left(\frac{w - \dot{y} - B_1\dot{\theta}}{V_m + v - \dot{x}}\right) \tag{1.3}$$

The angle of attack between the relative wind velocity and the deck, will be given by Equation 1.4, where θ is the angle of absolute rotation of the deck.

$$\alpha = \psi + \theta \tag{1.4}$$

The forces components and the sign conventions for forces and angles are shown in Figure 1.1. The choice of not considering the reference point in the center of the section allows to include in the modelling the angular speed of the deck $\dot{\theta}$ and therefore to introduce damping in the system.
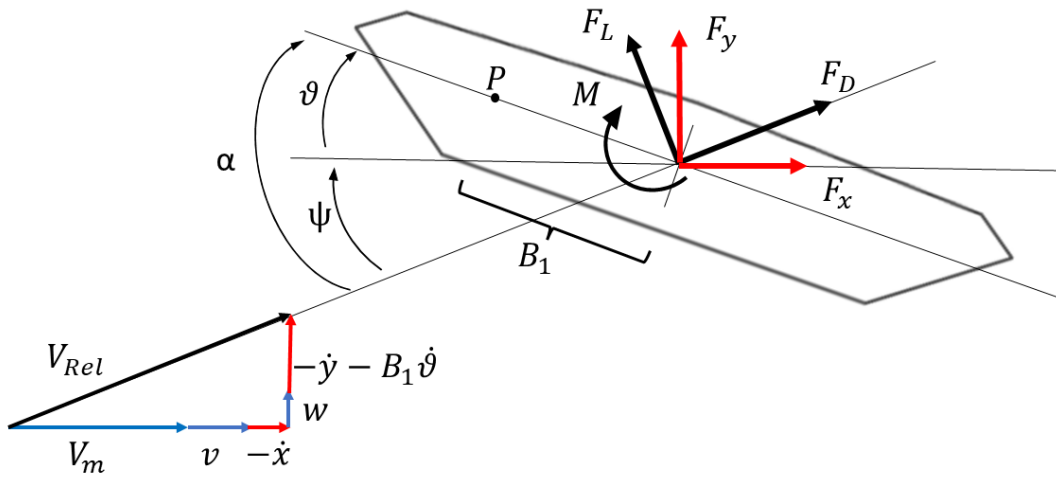

Figure 1.1: Absolute and apparent reference reference frames with sign conventions for forces and angles. It is also shown the vectorial sum for the relative velocity.

The problem can be simply modelled as in Figure 1.2, where y, x and θ stand for vertical, horizontal and torsional displacement components. The bridge has its natural vibration modes defined as vertical, horizontal and torsional motions, to understand the deck behaviour under turbulent wind action is sufficient to consider the fist vertical, horizontal and torsional modes. The elastic links represent the structural damping and stiffness on the three degrees of freedom granting the same natural frequencies as the first modes of the real structure. Lift, drag and pitch moment are converted to global reference system, using the angle of attack ϕ. Hence, the the equations of motion of the bridge deck section in Equation 1.5 are obtained.

$$m_x\ddot{x} + r_x\dot{x} + k_x x = F_x = F_D cos(\psi) - F_L sin(\psi)$$
$$m_y\ddot{y} + r_y\dot{y} + k_y y = F_y = F_D sin(\psi) - F_L cos(\psi) \tag{1.5}$$
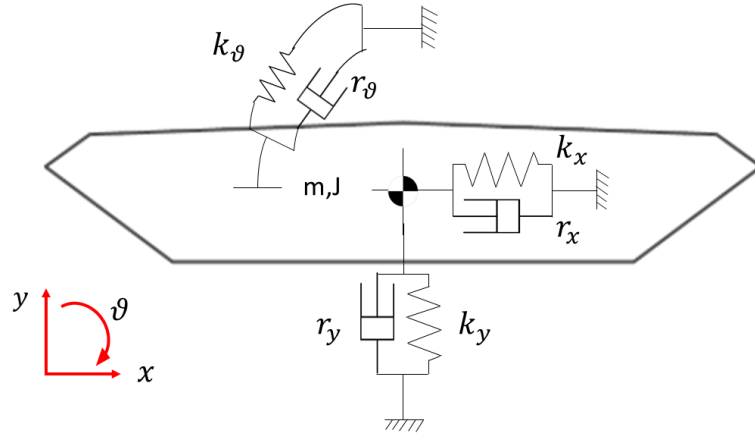$$J_G\ddot{\theta} + r_\theta\dot{\theta} + k_\theta = F_\theta = M$$

Figure 1.2: Elastically suspended deck section.

Substituting the expressions for the relative wind speed and the angle of attack (Equa-

tions 1.2 and 1.3) into Equation 1.5 the following non linear system is obtained:

$$m_x\ddot{x} + r_x\dot{x} + k_x x = \frac{1}{2}\rho BL\left((V_m + v - \dot{x})^2 + (w - \dot{y} - B_{1x}\dot{\theta})^2\right)(C_D(\alpha)cos(\psi) - C_L(\alpha)sin(\psi))$$

$$m_y\ddot{y} + r_y\dot{y} + k_y y = \frac{1}{2}\rho BL\left((V_m + v - \dot{x})^2 + (w - \dot{y} - B_{1y}\dot{\theta})^2\right)(C_D(\alpha)sin(\psi) - C_L(\alpha)cos(\psi))$$

$$J_G\ddot{\theta} + r_\theta\dot{\theta} + k_\theta = \frac{1}{2}\rho BL\left((V_m + v - \dot{x})^2 + (w - \dot{y} - B_{1\theta}\dot{\theta})^2\right)C_M(\alpha)$$

$$(1.6)$$

where:

$$\alpha = \theta + \psi = \theta + tan^{-1}\left(\frac{w - \dot{y} - B_1\dot{\theta}}{V_m + v - \dot{x}}\right) \tag{1.7}$$

The distance B_1 can assume different values according to the considered component of the aerodynamic forces (B_{1y} for F_y, B_{1x} for F_x and $B_{1\theta}$ for M). In this case the formulation is referred to as the Corrected Quasi Steady Theory (QSTC) (see Subsection 1.2.2 for details). Moreover, the non linear model expressed in Equation 1.6 can be expressed in matrix form using the state vector $\boldsymbol{X} = [x, y, \theta]^T$ as in Equation 1.8.

$$\boldsymbol{M_s}\ddot{\boldsymbol{X}} + \boldsymbol{R_s}\dot{\boldsymbol{X}} + \boldsymbol{K_s}\boldsymbol{X} = \boldsymbol{F}_{QST}\left(\boldsymbol{X}, \dot{\boldsymbol{X}}, V_m, v(t), w(t)\right) \tag{1.8}$$

Where

$$\boldsymbol{M_s} = \begin{bmatrix} m_x & & \\ & m_y & \\ & & J_G \end{bmatrix} ; \ \boldsymbol{R_s} = \begin{bmatrix} r_x & & \\ & r_y & \\ & & r_\theta \end{bmatrix} ; \ \boldsymbol{K_s} = \begin{bmatrix} k_x & & \\ & k_y & \\ & & k_\theta \end{bmatrix}$$

With the hypothesis of small variations of the parameters $\boldsymbol{X}, \dot{\boldsymbol{X}}, v(t), w(t)$, the above formulation of the self-excited forces can be linearised around an equilibrium position. The static equilibrium position can be found solving the static problem in Equation 1.9.

$$\boldsymbol{K_s}\boldsymbol{X} = \boldsymbol{F}_{static}\left(\boldsymbol{X}, V_m\right) \tag{1.9}$$

$$\boldsymbol{X}_0 = \begin{bmatrix} x_0 \\ y_0 \\ \theta_0 \end{bmatrix} ; \ \dot{\boldsymbol{X}} = \begin{bmatrix} 0 \\ 0 \\ 0 \end{bmatrix} ; \boldsymbol{b}_0 = \begin{bmatrix} v(t) \\ w(t) \end{bmatrix} = \begin{bmatrix} 0 \\ 0 \end{bmatrix}$$

Hence, the linear expression of the quasi-steady forces can be obtained by linearisation

around the equilibrium position:

$$\boldsymbol{F}_{QST}(\boldsymbol{X}, \dot{\boldsymbol{X}}, V_m, \boldsymbol{b}) = \boldsymbol{F}_{QST}(\boldsymbol{X}_0, \dot{\boldsymbol{X}}_0, \boldsymbol{b}_0) + \left.\frac{\partial \boldsymbol{F}_{QST}}{\partial \boldsymbol{X}}\right|_0 (\boldsymbol{X} - \boldsymbol{X}_0) + \left.\frac{\partial \boldsymbol{F}_{QST}}{\partial \dot{\boldsymbol{X}}}\right|_0 \dot{\boldsymbol{X}} + \left.\frac{\partial \boldsymbol{F}_{QST}}{\partial \boldsymbol{b}}\right|_0 \boldsymbol{b}$$

$$(1.10)$$

The different terms of the force components in Equations 1.6, 1.7 need, therefore, to be linearised around x_0, y_0, θ_0. This can be done assuming that the mean wind velocity is significantly larger than the turbulence components: $V_m >> w$, $V_m >> v$. This might be slightly inaccurate on top of the gusts, but in general it is an acceptable engineering approximation. It can be also assumed that the horizontal velocity of the structure is considerably smaller than the mean wind speed $V_m >> \dot{x}$. Finally, it is assumed that the angle of attack of the relative wind speed is sufficiently small that $tan(\psi) \simeq \psi$. Under all these assumptions and some passages shown in Appendix A, the linearised expression of the quasi-steady forces is rewritten in matrix form as in Equation (1.11).

$$\boldsymbol{F}_{QST} = \boldsymbol{F}_{QST}^{st} + \boldsymbol{R}_{ae}\dot{\bar{\boldsymbol{X}}} + \boldsymbol{K}_{ae}\bar{\boldsymbol{X}} + \boldsymbol{A}_m\boldsymbol{b} \tag{1.11}$$

Here the state vector $\bar{\boldsymbol{X}} = [\bar{x}, \bar{y}, \bar{\theta}]^T$ of displacements from the equilibrium position is defined, and the aerodynamic forces $\boldsymbol{F}_{QST}$ can be divided in static aerodynamic forces $\boldsymbol{F}_{QST}^{st}$, which are not dependent on the motion of the section and are shown in Equation (1.12a). And components function of the position $\bar{\boldsymbol{X}}$ and the velocity $\dot{\bar{\boldsymbol{X}}}$. These latter components are obtained multiplying the position and velocity by the damping, stiffness and admittance matrices shown in Equation (1.12).

$$\boldsymbol{F}_{QST}^{st} = \frac{1}{2}\rho BLV_m^2 \begin{bmatrix} C_{D0} \\ C_{L0} \\ BC_{M0} \end{bmatrix} \tag{1.12a}$$

$$\boldsymbol{R}_{ae} = -\frac{1}{2}BLV_m \begin{bmatrix} 2C_{D0} & C_D' - C_{L0} & B_{1x}(C_D' - C_{L0}) \\ 2C_{L0} & C_L' - C_{D0} & B_{1y}(C_L' - C_{D0}) \\ 2C_{M0}B & BC_M' & B_{1\theta}BC_M' \end{bmatrix} \tag{1.12b}$$

$$\boldsymbol{K}_{ae} = \frac{1}{2}\rho BLV_m^2 \begin{bmatrix} 0 & 0 & C_D' \\ 0 & 0 & C_L' \\ 0 & 0 & BC_M' \end{bmatrix} \tag{1.12c}$$

$$\boldsymbol{A}_m = \frac{1}{2}\rho BLV_m \begin{bmatrix} 2C_{D0} & C_D' - C_{L0} \\ 2C_{L0} & C_L' - C_{D0} \\ 2C_{M0}B & BC_M' \end{bmatrix} \tag{1.12d}$$

The linearised quasi-steady force can be introduced in the equation of motion in Equation 1.8 obtaining the linearised form in Equation 1.13.

$$\boldsymbol{M_s}\ddot{\bar{\boldsymbol{X}}} + (\boldsymbol{R_s} + \boldsymbol{R_{ae}})\dot{\bar{\boldsymbol{X}}} + (\boldsymbol{K_s} + \boldsymbol{K_{ae}})\bar{\boldsymbol{X}} = \boldsymbol{A_m}\boldsymbol{b} \tag{1.13}$$

The matrices $\boldsymbol{R_{ae}}$ and $\boldsymbol{K_{ae}}$ represent the aerodynamic damping and stiffness, that multiplied by $\dot{\bar{\boldsymbol{X}}}$ and $\bar{\boldsymbol{X}}$ give the self-excited aerodynamic forces. While the matrix $\boldsymbol{A_m}$ multiplied by $\boldsymbol{b}$ gives the buffeting forces function of the incoming turbulence. The action of the wind on the bridge is therefore capable of modifying the overall damping and stiffness of the structure. When matrix $\boldsymbol{K_{ae}}$ changes, also the natural frequencies of the structure change, compared to the still air condition, causing phenomena of instability: see Section 1.4.

1.2.   Aerodynamic Derivatives

As previously said, however, the QST is valid only for high reduced velocities $V^* > 10-20$. Therefore, for lower reduced velocity the way the structure itself influences the flow around it has to be taken in to account. In literature this is done by the unsteady aerodynamic models. These models modify the aerodynamic part of Equation (1.11) introducing in the dimensionless coefficients C_L, C_D, C_M the dependence on the wind velocity and the frequency of motion.

Among the unsteady models, the most common representation of self-excited aerodynamic forces is with dimensionless aerodynamic derivatives (ADs). They are also function of the external geometry of the girder and need to be determined experimentally by wind tunnel tests. The first to develop a theoretical formulation for the ADs was Theodorsen [24] applied to thin airfoils. Some years later, Scanlan and Tomko [17] expanded the model applying it to bridge engineering, resulting in 18 ADs to account for horizontal, vertical and torsional movement of the bridge section. There exist different notations to express the ADs, one is the one given by Scanlan and used in this work. An alternative notation, that is used at Politecnico di Milano, is shown in Appendix C.

The matrices from Equation (1.11) are therefore reformulated as shown in Equation (1.15) to introduce the dependency from the reduced circular frequency of motion $K = \frac{B\omega}{V} = \frac{2\pi}{V^*}$. The coordinate reference system considered is the same as Figure 1.1. The aerodynamic self-excited forces are therefore obtained as function of time, frequency of motion and wind speed.

$$\boldsymbol{F_{ae}}(t) = \boldsymbol{R_{ae}}(K)\dot{\boldsymbol{X}}(t) + \boldsymbol{K_{ae}}(K)\boldsymbol{X}(t) \tag{1.14}$$

$$\boldsymbol{R}_{ae}(K) = \frac{1}{2}\rho V B K \begin{bmatrix} P_1^* & P_5^* & BP_2^* \\ H_5^* & H_1^* & BH_2^* \\ BA_5^* & BA_1^* & B^2A_2^* \end{bmatrix} \tag{1.15a}$$

$$\boldsymbol{K}_{ae}(K) = \frac{1}{2}\rho V^2 K^2 \begin{bmatrix} P_4^* & P_6^* & BP_3^* \\ H_6^* & H_4^* & BH_3^* \\ BA_6^* & BA_4^* & B^2A_3^* \end{bmatrix} \tag{1.15b}$$

Here V is the mean wind velocity (previously referred as V_m, from here on the subscript m will be omitted), ρ is the air density and B is the girder width. The vector $\boldsymbol{X}(t) = [x(t), y(t), \theta(t)]^T$ represent the horizontal, vertical and torsional displacement of the section, positive in the same direction of the forces depicted in Figure 1.1. $P_i^*, H_i^*, A_i^*, i \in \{1, 2, ...6\}$ are the dimensionless ADs expressed in function of the reduced frequency of motion. Normally the aerodynamic derivatives are found experimentally through wind tunnel tests and therefore are known only at discrete frequencies, therefore Equation 1.14 is strictly valid only for a single harmonic motion. However, the self-excited forces can be calculated for a more general motion under the assumption that the principle of superposition holds.

Couples of ADs represent the real and imaginary part of the transfer functions between the different degrees of freedom and the self excited force, this can be seen taking the Fourier transform of Equation 1.14, obtaining Equation 1.16 [13], where $i = \sqrt{-1}$ is the imaginary unit.

$$\boldsymbol{G_{F_{ae}}}(\omega) = \frac{1}{2}\rho V^2 K^2 \begin{bmatrix} (P_1^*i + P_4^*) & (P_5^*i + P_6^*) & B(P_2^*i + P_3^*) \\ (H_5^*i + H_6^*) & (H_1^*i + H_4^*) & B(H_2^*i + H_3^*) \\ B(A_5^*i + A_6^*) & B(A_1^*i + A_4^*) & B^2(A_2^*i + A_3^*) \end{bmatrix} \boldsymbol{X}(\omega) \tag{1.16}$$

Here $\boldsymbol{G_{F_{ae}}}(\omega) = \int_{-\infty}^{\infty} \boldsymbol{F}_{ae}(t)e^{-i\omega t}dt$ is the vector of the Fourier transform of the self-excited forces, while $\boldsymbol{X}(\omega) = [X(\omega), Y(\omega), \Theta(\omega)]^T$ is the Fourier transform of the vector $\boldsymbol{X}(t)$ of the motion histories. To be independent from the scale it is often useful to use dimensionless quantities. Equation 1.16 can be adimensionalised obtaining the vector $\tilde{\boldsymbol{G}}_{\boldsymbol{F}_{ae}}(\omega)$ of adimentional transfer functions in Equation (1.17).

$$\tilde{\boldsymbol{G}}_{\boldsymbol{F}_{ae}}(\omega) = K^2 \begin{bmatrix} (P_1^*i + P_4^*) & (P_5^*i + P_6^*) & (P_2^*i + P_3^*) \\ (H_5^*i + H_6^*) & (H_1^*i + H_4^*) & (H_2^*i + H_3^*) \\ (A_5^*i + A_6^*) & (A_1^*i + A_4^*) & (A_2^*i + A_3^*) \end{bmatrix} \tilde{\boldsymbol{X}}(\omega) \tag{1.17}$$

Where $\tilde{\boldsymbol{X}}(\omega) = [\frac{X(\omega)}{B}, \frac{Y(\omega)}{B}, \Theta(\omega)]^T$ is the vector of adimentional input motions in frequency.

If the experimental identification of the ADs is done also at high reduced velocities, where also the QST is valid, the matrix coefficients in $\boldsymbol{R}_{ae}(K)$ can be used to experimentally identify the values of B_{1x}, B_{1y} and $B_{1\theta}$ that differentiate the QST to the QSTC (Equation (1.6)). Comparing the expression for the damping matrix in Equation 1.15a with the one in Equation 1.12b, it can be obtained:

$$B_{1x} = \frac{P_2^*}{P_5^*} B \tag{1.18a}$$

$$B_{1y} = \frac{H_2^*}{H_1^*} B \tag{1.18b}$$

$$B_{1\theta} = \frac{A_2^*}{A_1^*} B \tag{1.18c}$$

The formulation that uses aerodynamic derivatives to correct the QST is commonly called Correct Quasi Steady Theory (QSTC) [3].

Aerodynamic derivatives can be identified experimentally from wind tunnel tests with two different methods: the free motion method and the forced motion method.

1.2.1. Free motion method

In free motion tests the model is suspended with springs and vibrates due to imposed initial conditions and the interaction with the wind flow. The vibration of the system is measured. The comparison between the measured decay at a given wind speed and the computed one allow to identify the ADs through least squares minimization. [4]. Free motion tests are considered to give a more realistic in wind vibration of the deck and are easier and cheaper to set up. However, is more difficult and easily subjected to errors to identify aerodynamic derivatives from this kind of test.

1.2.2. Forced motion method

Forced motion tests are more expensive but much more reliable. The section model is forced to vibrate along the three degrees of freedom and the self-excited forces are measured in real-time for a constant wind speed. This kind of tests are also suitable for higher wind velocities, higher motion amplitudes and higher turbulence intensities. A possible drawback might be that with this methodology less realistic bridge motion can be realized. But this obstacle is partially overcome with special vibration rigs capable of forcing the model with any desired motion. This kinds of rigs are for example installed

in the wind tunnels of NTNU and PoliMi and described in Section 3.2. There are several methods to identify ADs from a forced vibration test. One possibility is to study the phase angle between the self-excited forces and the forced motion. Another possibility is to consider the complex Fourier amplitudes of the self-excited forces and relate them to the aerodynamic derivatives. However, these methodologies can lead to inaccuracies due to errors in the phase angle estimation or due to spectral leakage [19].

A more reliable method is to use a time domain approach where the model of self-excited forces is fitted through least-squares to the experimental data [19]. Equation 1.14 can be rewritten in a more compact matrix form as in Equation 1.19. Where $\boldsymbol{F}_{ae}(t, V, K)$ represent the self-excited forces dependent on time, the wind speed and the reduced frequency of motion. The matrix $\boldsymbol{E}$ collects all the ADs and the matrix $\boldsymbol{Z}$ contains the motion histories and their time derivatives. The mentioned matrices are shown in Equation 1.20 and 1.21.

$$\boldsymbol{F}_{ae}(t, V, K) = \boldsymbol{Z}\boldsymbol{E} \tag{1.19}$$

$$\boldsymbol{E} = \frac{1}{2}\rho V^2 BK \begin{bmatrix} P_1^*/V & H_5^*/V & BA_5^*/V \\ P_5^*/V & H_1^*/V & BA_1^*/V \\ BP_2^*/V & BH_2^*/V & B^2A_2^*/V \\ KP_4^*/B & KH_6^*/B & KA_6^* \\ KP_6^*/B & KH_4^*/B & KA_4^* \\ KP_3^* & KH_3^* & BKA_3^* \end{bmatrix} \tag{1.20}$$

$$\boldsymbol{Z} = \begin{bmatrix} \dot{x}_1 & \dot{y}_1 & \dot{\theta}_1 & x_1 & y_1 & \theta_1 \\ \dot{x}_2 & \dot{y}_2 & \dot{\theta}_2 & x_2 & y_2 & \theta_2 \\ \vdots & \vdots & \vdots & \vdots & \vdots & \vdots \\ \dot{x}_n & \dot{y}_n & \dot{\theta}_n & x_n & y_n & \theta_n \end{bmatrix} \quad \boldsymbol{F}_{ae} = \begin{bmatrix} F_{ae,x_1} & F_{ae,y_1} & F_{ae,\theta_1} \\ F_{ae,x_2} & F_{ae,y_2} & F_{ae,\theta_2} \\ \vdots & \vdots & \vdots \\ F_{ae,x_n} & F_{ae,y_n} & F_{ae,\theta_n} \end{bmatrix} \tag{1.21}$$

The coefficients matrix $\boldsymbol{E}$ can then be found, and thus the ADs by minimizing the sum of squares as in Equation 1.22.

$$\boldsymbol{E} = (\boldsymbol{Z}^T\boldsymbol{Z})^{-1}\boldsymbol{Z}^T\boldsymbol{F}_{ae} \tag{1.22}$$

Once ADs are identified, the self-excited forces can be expressed with Equation 1.14 as function of time, wind speed and discrete reduced frequencies.

To have a continuous time domain description and to remove the dependency on the frequency of motion a new dynamic model has to be introduced. A model that is usually applied is the rational functions model (Section 1.3).

In the present work an alternative approach will be presented: approximating the system

transfer functions with a linear expansion of special orthonormal functions. These functions are called Laguerre filters and their application to bridge aerodynamic is exposed in Section 2.3.

1.3.   Rational Functions

The rational functions model is identified in frequency domain interpolating the experimental data of the aerodynamic derivatives for any reduced frequency of motion with a curve fit. Then the time domain representation is obtained through inverse Fourier transforming. Therefore the chosen expression must be suitable for this kind of domain change [14]. A formulation frequently used in literature [13, 18] is reported in Equation 1.23. As an example, in Equation 1.23a is reported the transfer function for the self-excited forces due to vertical motion. The rational functions are contained in the one by three vectors $\boldsymbol{a}_i^y$, $i \in [1, ...N]$, while d_l^y is the lag coefficient related to the lift force, in general more lag terms can be included, but for many cross sections one is usually considered sufficient $(N = 4)$ [18].

$$\boldsymbol{G}_{F_y^{ae}}(\omega) = \frac{1}{2}\rho V^2 \left[\boldsymbol{a}_1^y + \boldsymbol{a}_2^y \frac{i\omega B}{V} + \boldsymbol{a}_3^y (\frac{i\omega B}{V})^2 + \sum_{l=1}^{N-3} \boldsymbol{a}_{l+3}^y \frac{i\omega B/V}{i\omega B/V + d_l^y} \right] \qquad (1.23a)$$

$$F_y^{ae}(t) = \frac{1}{2}\rho V^2 \bigg(\boldsymbol{a}_1^y \boldsymbol{X}(t) + \frac{B}{V} \boldsymbol{a}_2^y \dot{\boldsymbol{X}}(t)$$

$$+ \sum_{l=1}^{N-3} \boldsymbol{a}_{l+3}^y \left(\boldsymbol{X}(t) - \frac{d_l^y V}{B} \int_0^t e^{-\frac{d_l^y V}{B}(t-\tau)} \boldsymbol{X}(\tau) d\tau \right) \bigg) \qquad (1.23b)$$

By taking the inverse Fourier transform of the transfer function in Equation 1.23a, and neglecting the added mass effect $(\boldsymbol{a}_3 \approx 0)$, the time domain expression of the self-excited lift force due to motion in all the three degrees of freedom can be obtained as in Equation 1.23b. Here $\boldsymbol{X}(t) = [x(t), y(t), \theta(t)]^T$ is the three by one vector containing the displacement of the three degrees of freedom in the instant t.

The rational function coefficients can be determined by non-linear least squares fit to experimental aerodynamic derivatives. The relation between rational functions and aerodynamic derivatives can be derived by the real and imaginary part of the transfer function in Equation 1.23a, considering only the lift force due to vertical motion, leading to Equation 1.24 [13].

In recent years algorithms have been developed to directly extract rational functions from forced vibration tests data [2] without passing from aerodynamic derivatives. This might

save some errors caused by fitting a model to another experimental model.

$$H_4^* = \frac{Re(F_{yy}(\omega))}{1/2\rho V^2 K^2} = \hat{V}^2 \left(a_1^{yy} + \sum_{l=1}^{N-3} a_{l+3}^{yy} \frac{1}{(d_l^{yy}\hat{V})^2 + 1} \right)$$

$$H_1^* = \frac{Im(F_{yy}(\omega))}{1/2\rho V^2 K^2} = \hat{V}^2 \left(a_2^{yy} + \hat{V}^2 \sum_{l=1}^{N-3} a_{l+3}^{yy} \frac{d_l^{yy}}{(d_l^{yy}\hat{V})^2 + 1} \right)$$

(1.24)

Equation 1.23b can be also reformulated in matrix form, to obtain a state-space representation of the problem. This representation is shown in Equation 1.25, where the self excited forces for each degree of freedom are represented as function of the rational functions.

$$\boldsymbol{F}^{ae} = \boldsymbol{A}_1 \boldsymbol{X}(t) + \boldsymbol{A}_2 \dot{\boldsymbol{X}}(t) + \boldsymbol{Z}(t)$$

$$\boldsymbol{A}_1 = \frac{1}{2}\rho V^2 \boldsymbol{a}_1, \quad \boldsymbol{A}_2 = \frac{1}{2}\rho V^2 \frac{B}{V} \boldsymbol{a}_2$$

$$\boldsymbol{Z}(t) = \frac{1}{2}\rho V^2 \sum_{l=1}^{N-3} \boldsymbol{a}_{l+3}^y \left(\boldsymbol{X}(t) - \frac{d_l V}{B} \int_0^t e^{-\frac{d_l V}{B}(t-\tau)} \boldsymbol{X}(\tau)d\tau \right)$$

(1.25)

Here $\boldsymbol{a}_i$, $i \in [1, ...4]$ are three by three matrices to give the forces on all the three degrees of freedom. The vector $\boldsymbol{Z}$ contains the time-history-dependent terms.

It is time consuming to calculate the convolution integrals numerically: it is therefore convenient to include them as unknowns in the system of equations [14]. The vector $\boldsymbol{Z}$ can be expressed as shown in Equation 1.26.

$$\boldsymbol{Z} = \boldsymbol{Q}\boldsymbol{\Delta}$$

$$\boldsymbol{Q} = \begin{bmatrix} \boldsymbol{A}_4 & \boldsymbol{A}_5 & \dots & \boldsymbol{A}_N \end{bmatrix}^T \quad \boldsymbol{\Delta} = \begin{bmatrix} \boldsymbol{\delta}_1^T, \boldsymbol{\delta}_2^T, \dots \boldsymbol{\delta}_{N-3}^T \end{bmatrix}^T$$

(1.26)

Here the components of vector $\boldsymbol{X}$ contain the convolution integrals as shown in Equation 1.27. Taking the derivative of this equation, these integrals can be modelled by first order differential equations obtaining Equation 1.28 [14].

$$\boldsymbol{\delta}_l = \left(\boldsymbol{X}(t) - \frac{d_l V}{B} \int_0^t e^{-\frac{d_l V}{B}(t-\tau)} \boldsymbol{X}(\tau)d\tau \right)$$

(1.27)

$$\dot{\boldsymbol{\delta}}_l = \boldsymbol{X}(t) - \frac{d_l V}{B} \boldsymbol{\delta}_l$$

(1.28)

Therefore from Equation 1.28 can be obtained the additional equation needed to introduce the convolution integrals as unknowns in the system. The representation of self-excited

forces with state-space matrices is then shown in Equation 1.29.

$$\boldsymbol{A_1 X} + \boldsymbol{A_2 \dot{X}} + \boldsymbol{Q \Delta} = \boldsymbol{F}^{ae}$$
$$\boldsymbol{E \dot{X}} + \boldsymbol{B \dot{\Delta}} + \boldsymbol{D \Delta} = 0$$

(1.29)

Where

$$\boldsymbol{E} = \begin{bmatrix} \boldsymbol{I} \\ \boldsymbol{I} \\ \vdots \\ \boldsymbol{I} \end{bmatrix}, \ \boldsymbol{B} = \begin{bmatrix} \boldsymbol{I} & & & \\ & \boldsymbol{I} & & \\ & & \ddots & \\ & & & \boldsymbol{I} \end{bmatrix}, \ \boldsymbol{D} = \frac{V}{B} \begin{bmatrix} d_1 \boldsymbol{I} & & & \\ & d_2 \boldsymbol{I} & & \\ & & \ddots & \\ & & & d_{N-3} \boldsymbol{I} \end{bmatrix}$$

(1.30)

and $\boldsymbol{I}$ is three by three identity matrix.

1.4.   Instability Conditions in Bridge Aerodynamics

Once a correct dynamic model has been defined, it can be used to identify the critical working conditions that might lead to unstable motions. If the reduced velocity is high enough to use the QST, to identify unstable conditions, the deck equations of motion in Equation (1.13) can be rewritten in homogeneous form as in Equation (1.31).

$$\boldsymbol{M_s \ddot{\bar{X}}} + (\boldsymbol{R_s} + \boldsymbol{R_{ae}}) \dot{\bar{X}} + (\boldsymbol{K_s} + \boldsymbol{K_{ae}}) \bar{X} = \boldsymbol{0}$$

(1.31)

It can be imposed $\bar{\boldsymbol{X}} = \bar{\bar{\boldsymbol{\Phi}}} e^{\lambda t}$ obtaining Equation (1.32) writing in compact form the matrices $\boldsymbol{R_t} = \boldsymbol{R_s} + \boldsymbol{R_{ae}}$ and $\boldsymbol{K_t} = \boldsymbol{K_s} + \boldsymbol{K_{ae}}$. The λ values for which the determinant of $(\lambda^2 \boldsymbol{M_s} + \lambda \boldsymbol{R_t} + \boldsymbol{K_t})$ is equal to zero identify the eigenvalues, while the corresponding $\bar{\bar{\boldsymbol{\Phi}}}$ are the eigenvectors.

$$(\lambda^2 \boldsymbol{M_s} + \lambda \boldsymbol{R_t} + \boldsymbol{K_t}) \bar{\bar{\boldsymbol{\Phi}}} = \boldsymbol{0}$$

(1.32)

However, if QST cannot be considered, the representation with aerodynamic derivatives must be introduced to consider the influence of the structure in the flow around it. Therefore, the stiffness and damping matrices will be expressed as in Equation (1.15) and will be function of λ as well. This will cause the eigenvalue problem to be solved in an iterative way.

To avoid this, the problem can be rewritten in a state-space form using the rational function model to interpolate the aerodynamic derivatives. The rational functions state-space form in Equation (1.29) is coupled with the equation of motion of the system in Equation (1.8), obtaining the system in Equation (1.33). This is then rearranged in a correct

state-space form as in Equation (1.34).

$$M\ddot{X} + (R_s - A_2)\dot{X} + (K_s - A_1)X - Q\Delta = 0$$
$$E\dot{X} + B\dot{\Delta} + D\Delta = 0$$

(1.33)

$$\begin{bmatrix} \dot{X} \\ \ddot{X} \\ \dot{\Delta} \end{bmatrix} = \begin{bmatrix} 0 & I & 0 \\ M^{-1}(A_1 - K_s) & M^{-1}(A_2 - R_s) & M^{-1}Q \\ 0 & -B^{-1}E & -B^{-1}D \end{bmatrix} \begin{bmatrix} X \\ \dot{X} \\ \Delta \end{bmatrix}$$

(1.34)

Hence, the eigenvalues of the system will be the eigenvalue of the matrix in Equation (1.34).

Instability occurs when one of the eigenvalues have positive real part. The associated eigenvectors identify the kind of instability: one or two degrees of freedom instability.

Suspended bridge decks do not suffer from 1 degree of freedom (1 D.o.f.) instability, which occurs when one of the diagonal terms of R_{ae} is negative and greater than the corresponding one in the R_s matrix, as absolute value. However, they are subjected to 2 d.o.f. instability, also called flutter instability. Flutter instability occurs when the equivalent stiffness matrix $K_{ae} + K_s$ is not symmetric, this is always the case in bridge aerodynamic, and is in condition to make the vertical and torsional frequencies coincide [24]. The wind speed at which one of the eigenvalues gets zero real part is called flutter critical speed. Above that velocity the bridge will be unstable.

Flutter instability is a major problem with very long suspended bridges. Indeed, increasing the span length, the ration between torsional and corresponding vertical frequencies decreases, and the aerodynamic forces can therefore more easily make them coincide. In bridge aerodynamic the wind speed that causes flutter instability is called flutter critical speed, and it is an important design parameter for bridge engineering.

2 | The Use of Orthonormal Basis for System Identification

2.1. Orthonormal Functions

A set of functions $v_1(\tau), v_2(\tau), \dots$ is said to be *orthonormal* in the range (a, b) if it satisfies the relation:

$$\int_a^b v_n(\tau) v_m(\tau)\, d\tau = \begin{cases} 1 & \text{if } m = n \\ 0 & \text{if } m \neq n \end{cases} \tag{2.1}$$

Then any generic real and continuous function $f(\tau)$ can be represented as a linear combination of these orthonormal functions:

$$f(\tau) = \sum_{n=1}^{\infty} c_n v_n(\tau) \tag{2.2}$$

$$c_n = \int_a^b f(\tau) v_n(\tau)\, d\tau \tag{2.3}$$

The expression for the coefficients of the linear combination is the one in Equation (2.3), this is because if Equation (2.2) is multiplied by $v_m(\tau)$ and integrated over (a, b) the following expression is obtained:

$$\int_a^b f(\tau) v_m(\tau)\, d\tau = \int_a^b \sum_{n=1}^{\infty} c_n v_n(\tau) v_m(\tau)\, d\tau$$

which leads in accordance to Equation (2.1) to:

$$\int_a^b f(\tau) v_n(\tau)\, d\tau = \begin{cases} c_m & \text{if } m = n \\ 0 & \text{if } m \neq n \end{cases}$$

A series of orthonormal functions $\{v_n(\tau)\}$, it is said to be *complete* if the following statements are true.

1. There exists no function $x(\tau)$ with $\int_a^b x^2(\tau)d\tau < \infty$ such that

$$\int_a^b x(\tau)v_n(\tau)d\tau = 0 \text{ for } n = 1, 2, ... \tag{2.4}$$

2. For any piece-wise continuous function $f(\tau)$ with $\int_a^b f^2(\tau)d\tau < \infty$ and $\epsilon > 0$, however small, it exist a integer N and a polynomial $\sum_{n=1}^N c_n v_n(\tau)$ such that

$$\int_a^b |f(\tau) - \sum_{n=1}^N c_n v_n(\tau)|^2 d\tau < \epsilon \tag{2.5}$$

The expansion in Equation (2.2) has, in theory an infinite number of terms. However, if the set is complete the function $f(\tau)$ can be approximated arbitrarly closely by a finite summation $\sum_{n=1}^N c_n v_n(\tau)$ with an increasing number of terms N. With the orthonormalization in time or frequency domain [8] it is possible to manipulate series of real and continuous functions to obtain series that are complete and satisfy the orthonormal properties in Equation (2.1).

2.2. Orthonormal Functions for Impulse Response approximation

A complete orthonormal sets $\{v_n(\tau)\}$ seen above can therefore be used to express exactly (with an infinite summation) or to approximate, any kind of continuous real functions. It is interesting to use them to express the unit-impulse response of linear systems $h(t)$, as in Equation (2.6).

$$h(t) = \sum_{n=1}^\infty c_n v_n(t) \text{ with } 0 \le t < \infty \tag{2.6}$$

In theory the summation in Equation (2.6) requires an infinite number of terms. However, if the impulse response $h(\tau)$ satisfies the condition in Equation (2.7), thanks to properties of complete sets (Equation 2.5), it can be approximated arbitrarily closely by a linear combination of orthonormal functions $\sum_{n=1}^N c_n v_n(\tau)$ with an increasing number of terms.

$$\int_a^b h^2(\tau)d\tau < \infty \tag{2.7}$$

The condition on the impulse response expressed in Equation (2.7) is the condition for a system to be L^2 stable. That means a system with all poles strictly on the left-half

complex plane. For this class of systems the accuracy of the approximation of the impulse response increases with the number of terms considered.

The coefficients of the expansion can be found minimizing the cost functions in Equation (2.8). Because of the orthonormal properties of the set $\{v_n(\tau)\}$, seen in Section 2.1, the optimal solution is given by Equation (2.9).

$$C = \int_0^\infty (h(\tau) - \sum_{n=1}^N c_n v_n(\tau))^2 d\tau \tag{2.8}$$

$$c_n = \int_0^\infty h(t) v_n(t) dt \tag{2.9}$$

The same orthonormal function expansion can be done in frequency domain. The transfer function of the system is the Fourier transform of the impulse response function. However, as seen previously, the impulse response function can be written as linear combination of orthonormal functions as in Equation (2.10). Here $i = \sqrt{-1}$ is the imaginary unit.

$$H(\omega) = \int_{-\infty}^\infty h(t) e^{-i\omega} dt =$$
$$= \int_{-\infty}^\infty \sum_{n=1}^N c_n v_n(t) e^{-i\omega} dt \tag{2.10}$$

$$H(\omega) = \sum_{n=1}^N c_n V_n(\omega) \tag{2.11}$$

Bringing the summation out of the integrals, as it doesn't depend on time, it can be seen how also the transfer function of the system in frequency domain can be written as a summation of orthonormal functions as in Equation 2.11. In this case these functions $V_n(\omega)$ are the Fourier transform of the orthonormal set $\{v_n(\tau)\}$ considered in time domain.

2.3. Laguerre Functions

An interesting example is the series known as Laguerre functions $\{l_n(\tau)\}$ given in [8, 21, 22] as orthonormalization of the sequence $(p\tau)^n e^{-p\tau}$ for $n = 0, 1, 2, ...$ in the range $0 \leq \tau < \infty$. This set satisfies the orthonormal and complete properties defined in Equation (2.1) and (2.4). The set of Laguerre functions is defined as in Equation (2.12) in continuous time-domain, where n is the order of the function and $p > 0$ is the decay rate. The higher is the value of p, the shorter is the settling time of the function, as shown in Figure 2.2. Figure 2.1 shows Laguerre functions of different orders, note that the number of crossings

of the horizontal axis is equal to the order n.

$$l_0(\tau) = \sqrt{2p}\, e^{-p\tau}$$
$$l_1(\tau) = \sqrt{2p}(-2p\tau + 1)e^{-p\tau}$$
$$\vdots = \vdots \tag{2.12}$$
$$l_n(\tau) = \sqrt{2p} \sum_{k=0}^{n} (-1)^k (2p\tau)^{n-k} \frac{n!}{k![(n-k)!]^2}\, e^{-p\tau}$$

It can be seen how this set is a particularly suitable basis for estimation of transfer functions of damped dynamical systems as its functions have an inbuilt exponential decay.
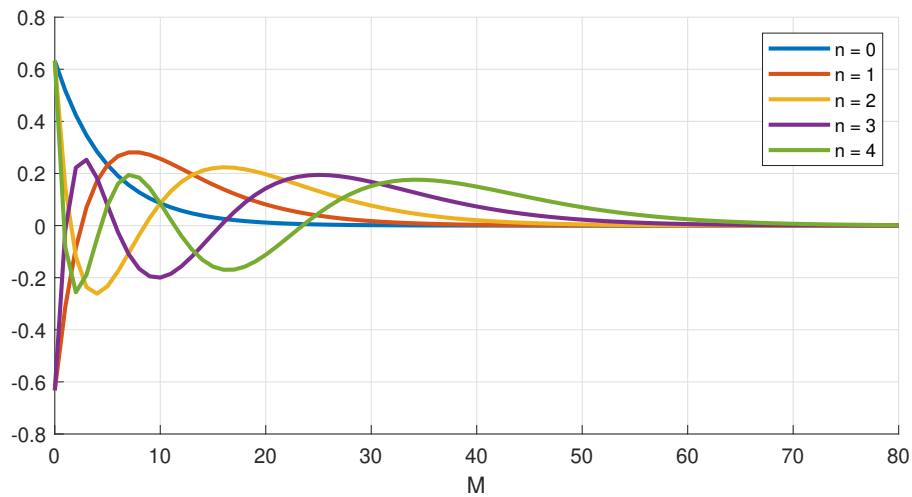

Figure 2.1: Laguerre functions $l_n(\tau)$ $n = 0, 1, 2, 3, 4$, $p = 0.2$
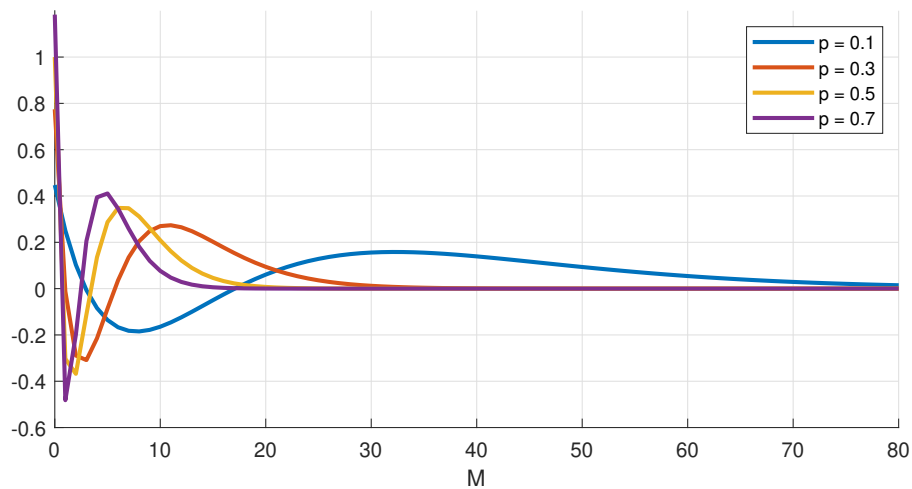
Figure 2.2: Second order Laguerre function $l_2(\tau)$ for different p values.

Applying the Laplace transform to Equation (2.12), the set of Laguerre filters $\{L_n(\omega)\}$ can be found also in continuous-frequency domain [6, 8] as in Equation (2.13).

$$
\begin{aligned}
L_0(\omega) &= \int_0^\infty l_0(t)e^{-i\omega t}dt = \frac{\sqrt{2p}}{2\pi}\frac{1}{(p+i\omega)} \\
L_1(\omega) &= \int_0^\infty l_1(t)e^{-i\omega t}dt = \frac{\sqrt{2p}}{2\pi}\frac{(p-i\omega)}{(p+i\omega)^2} \\
&\vdots = \vdots \\
L_n(\omega) &= \int_0^\infty l_n(t)e^{-i\omega t}dt = \frac{\sqrt{2p}}{2\pi}\frac{(p-i\omega)^n}{(p+i\omega)^{n+1}}
\end{aligned}
\tag{2.13}
$$

Applying Parseval's theorem to the set $\{l_n(t)\}$ and its transform $\{L_n(\omega)\}$, Equation (2.14) is obtained.

$$
\int_0^\infty l_m(t)l_n(t)dt = 2\pi \int_{-\infty}^\infty \overline{L}_m(\omega)L_n(\omega)d\omega
\tag{2.14}
$$

Because of the orthonormal properties of the set $\{l_n(t)\}$ follows that the filters transfer functions in Equation (2.13) satisfy the orthonormal properties in frequency domain of Equation (2.15).

$$
2\pi \int_{-\infty}^\infty \overline{L}_m(\lambda)L_n(\lambda)d\lambda =
\begin{cases}
1 & \text{if } m = n \\
0 & \text{if } m \neq n
\end{cases}
\tag{2.15}
$$

The Laguerre functions set can be also reformulated to pass in discrete time and discrete frequency domain. In the present work the formulation in Equation (2.16), given by [9], is used to construct a model in discrete time domain. Moreover, this is done for comparative purposes with the work in [20].

$$
g_n[k] = \alpha^{\frac{k-n}{2}}(1-\alpha)^{1/2}\sum_{i=0}^n(-1)^i\binom{k}{i}\binom{n}{i}\alpha^{n-i}(1-\alpha)^i \text{ for } k > 0
\tag{2.16}
$$

The discrete time formulation in Equation (2.16) can be passed in discrete frequency domain via z-transform, obtaining the relation in Equation (2.17).

$$
G_n(z) = \left(\frac{\sqrt{\alpha} - z^{-1}}{1 - \sqrt{\alpha}z^{-1}}\right)^n \left(\frac{\sqrt{1-\alpha}}{1-\sqrt{\alpha}z^{-1}}\right)
\tag{2.17}
$$

In discrete time, as in continuous time, the functions tend to zero for large values of k controlled by the decay parameter α as can be seen in Figure 2.3. However, the decay parameter in the formulation by [9] can assume only values in the range $0 < \alpha < 1$, and

to higher values corresponds a longer settling time as shown in Figure 2.4.

$$|G_n(z)| = \left| \frac{\sqrt{1-\alpha}}{1 - \sqrt{\alpha}z^{-1}} \right| \tag{2.18}$$

It can be noted from Equation (2.18) and from Figure 2.5 how the gain of these filters is independent from the filter order n and depends only on the decay parameter α [20].
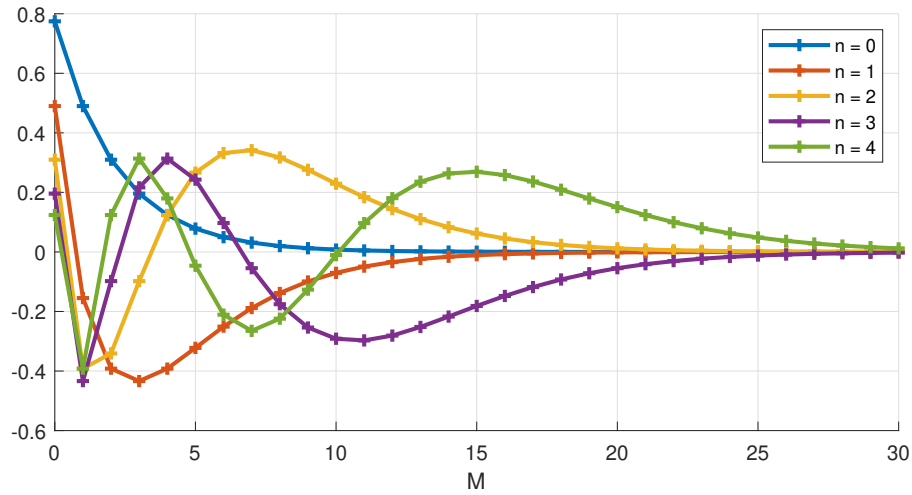

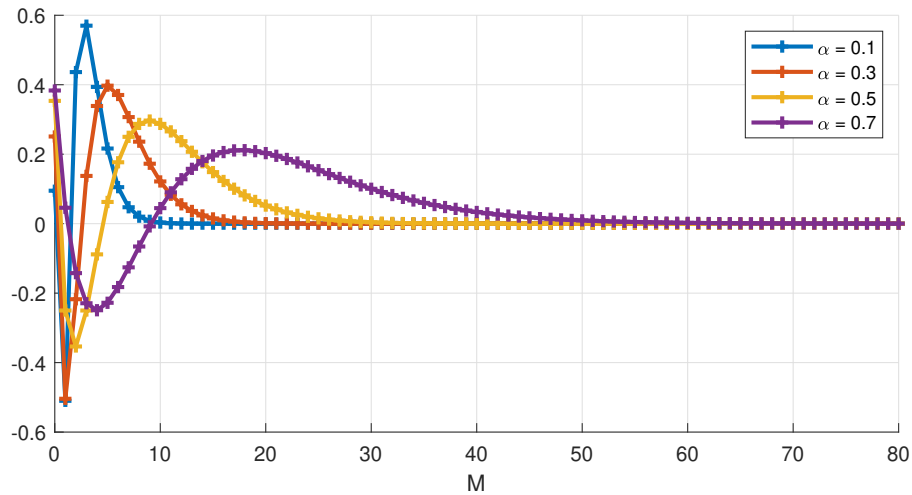Figure 2.3: Laguerre functions $g_n[k]$ $n = 0, 1, 2, 3, 4$, $\alpha = 0.4$.

Figure 2.4: Second order discrete Laguerre function $g_2[k]$ for different α values.
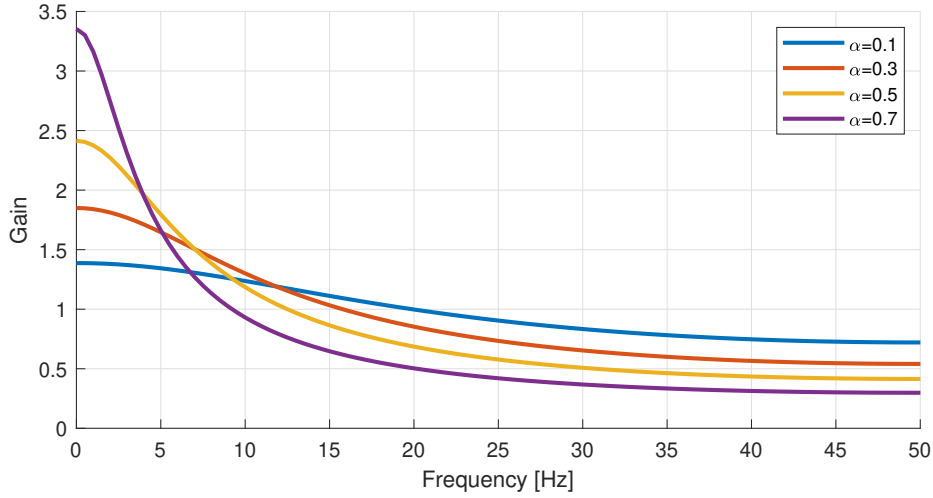
Figure 2.5: Gain of Laguerre functions $|G_n(z)|$ for different decay factors. The gain is independent from the filter order n and depends only on the decay factor α.

2.4. Laguerre Orthonormal Expansion in Bridge Aerodynamic

With the aim of characterize the bridge aerodynamic problem, if the hypothesis of small vibration is taken, a linear approximation of the system transfer functions can be considered. A general linear single-input-single-output system (SISO) can be written in continuous time-domain in terms of the well-known convolution integral:

$$F_n(t) = h_{nm0} + \int_0^t h_{nm}(\tau)r_m(t-\tau)\,d\tau \tag{2.19}$$

If this model is applied to a section of a bridge deck, the input, $r_m(t)$, will be either the horizontal, the vertical or the pitch motion. While the output, $F_n(t)$, will be either the self-excited drag, lift or pitch moment. The term h_{nm0} is the static contribution, while $h_{nm}(t)$ is the impulse response function relative to the specific combination of input motion and output force. If this model is used however, because of the linear approximation, all the non-linear effects of the self-excited forces cannot be captured.

The impulse response function can be rewritten as shown in Section 2.2 with a linear combination of infinite orthonormal Laguerre functions as in Equation (2.20).

$$F_n(t) = h_{nm0} + \int_0^t \sum_{j=0}^{\infty} c_j^{nm} l_j(\tau)r_m(t-\tau)\,d\tau \tag{2.20}$$

However, if a stable system with all poles strictly on the left-half complex plane is considered, the impulse response function can be approximated with a finite summation of L functions and the goodness of the approximation increases with the number of polynomials considered. Therefore Equation (2.21) is obtained.

$$F_n(t) = h_{nm0} + \int_0^t \sum_{j=0}^L c_j^{nm} l_j(\tau) r_m(t - \tau) \, d\tau \tag{2.21}$$

To identify the system with numerical methods the convolution integral must be rewritten in discrete time-domain. Introducing the assumption that the system has finite memory with length M, the Equation (2.19) can be rewritten in the form of Equation (2.22) in discrete time.

Then Equation (2.23) is obtained approximating the discrete impulse response with L discrete Laguerre functions according to the formulation by [20] (Equation (2.16)).

$$F_n[n] = h_{nm0} + \sum_{k=0}^M h_{nm}[k] r_m[n - k] \tag{2.22}$$

$$F_n[n] = h_{nm0} + \sum_{k=0}^M \sum_{l=0}^L c_l^{nm} g_l[k] r_m[n - k] \tag{2.23}$$

Identifying the impulse response functions of the system in time domain can be quite computationally expensive according to the memory length considered. However, comparing Equation (2.22) with Equation (2.23), it can be seen how expanding with orthonormal series the system first order kernel can reduce the computational burden of the problem. In the case of Equation (2.22), to characterize the system, M unknown coefficients ($h(k)$ $i = 1, ...M$) have to be determined. And this has to be done for each possible combination between input motion and output self-excited force. Considering a two dimensional deck section with three degrees of freedom, this means $3M$ coefficients for each of the three possible input motions, for a total of $9M$ coefficients to be determined.

Instead, an alternative is to expand the impulse response function $h(k)$ with the set of orthonormal function $\{g_l[k]\}$ with $l = 0, 1, ...L$ as in Equation (2.23). In this case the unknowns to determine will become the c_i coefficients with $i = 1, 2..., L$ for each degree of freedom: with a total of $3L$ coefficients for each of the three possible input motions. This results in a total of $9L$ coefficients to be determined.

If a good approximation can be obtained with $L < M$ filters, then the reduction of computational burden can be significant.

Moreover, all the Laguerre filters decay to zero because they have an inbuilt negative exponential, this makes them particularly suitable for the approximation of most mechanical

system impulse response functions. This property makes them also good low-pass filters suppressing higher-order noise, allowing for a smoother estimation of the response functions compared to other functions. Finally, if the training of the model is done with white noise input, the coefficients of the functions become orthogonal, which makes the identification process better conditioned.

As shown in Section 2.2, the approximation can be done also in frequency domain, expanding the system transfer functions as linear combination of orthonormal filters.

$$F_n(\omega) = h_{nm0}\delta(\omega) + H_{nm}(\omega)R_m(\omega) \tag{2.24}$$

For the convolution theorem the Fourier transform of the convolution integral in Equation 2.19 becomes the product of the Fourier transform of the input signal $R(\omega)$ and the transfer function $H(\omega)$, as in Equation 2.24. Then the transfer function can be approximated with a finite sum of filters as in Equation 2.25, where $G_j(\omega)$ are the Laguerre filters in frequency domain from Equation (2.17). It is interesting to notice that the coefficients of the expansion in time domain are the same in frequency domain, so the identification process can be done in either one of the two.

$$F_n(\omega) = h_{nm0}\delta(\omega) + \left(\sum_{j=1}^{\infty} c_j^{nm} G_j(\omega)\right) R_m(\omega) \tag{2.25}$$

In the following is shown with a simple example how the coefficients of the Laguerre filters can be found through least-squares identification in time domain and, once the model is trained, how it can be used to foresee the output for a generic input. Moreover, which is the influence of the model parameters on the goodness of the prediction.

2.5. 1 Dof example: Identification of First Order System

A simple example is created to give a clearer example of the Laguerre model identification procedure. The first order system in Equation (2.26) is considered, which has the typical transfer function in Equation (2.27). The input is the time series $u(t)$, while the output is $y(t)$ and τ is the time constant of the system which is set to $\tau = 0.15$.

$$\tau\dot{y}(t) + y(t) = u(t) \tag{2.26}$$

$$H(s) = \frac{1}{\tau s + 1} \tag{2.27}$$

Since the presented Laguerre expansion model is a discrete time model, the system in Equation (2.26)-(2.27) is discretised with time step $\Delta t = 0.005s$ as in Equation (2.28)-(2.29) with Tustin method.

$$y[k+1] = e^{-\frac{1}{\tau}\Delta t}y[k] + (1 - e^{-\frac{1}{\tau}\Delta t})u[k] \tag{2.28}$$

$$H(z) = \frac{\Delta t(z+1)}{(\Delta t + 2\tau)z + \Delta t - 2\tau} \tag{2.29}$$

To train the Laguerre model a sinusoidal training input $u_{train}(t)$ is created with six excitation frequencies at $0.5, 1, 1.5, 2, 2.5, 3Hz$ as shown in Figure 2.6. The system output $y_{train}(t)$ for the training input is simulated with the Matlab [23] function *lsim()*.
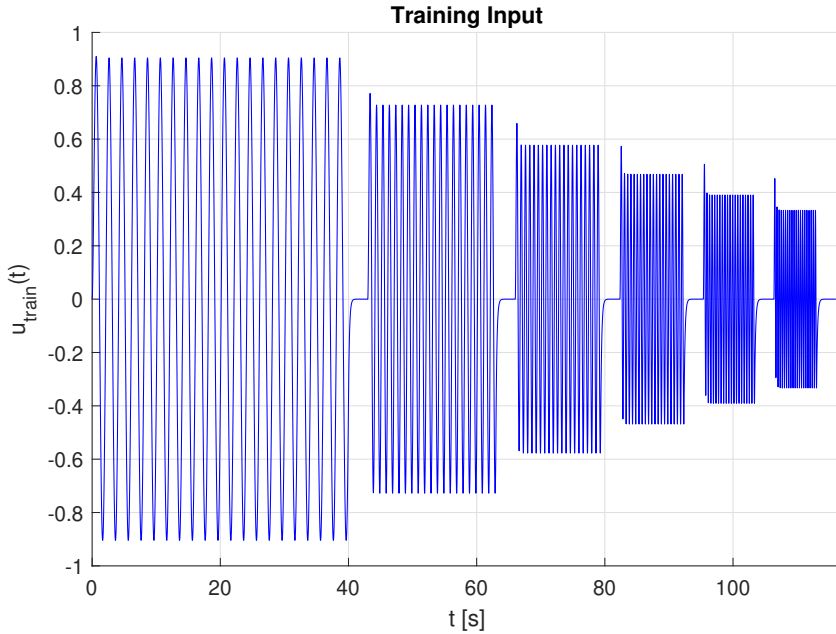
Figure 2.6: Training input time series with vibration frequencies at $0.5, 1, 1.5, 2, 2.5, 3Hz$. Used to train the Laguerre model.

The Laguerre model is defined reformulating Equation (2.23) in matrix form. The constant coefficient h_{nm0} is neglected because in this example the training signal is with null mean value. The time history of the input $\boldsymbol{u}$ is arranged in the matrix $\boldsymbol{A}$ to consider the absence of past memory as in Equation (2.32). The discrete values of the filters evaluated over the memory M are arranged in the matrix $\boldsymbol{G}$. The product between matrix $\boldsymbol{A}$ and matrix $\boldsymbol{G}$ gives the regression matrix $\boldsymbol{X}$, which is multiplied by the vector of coefficients $\boldsymbol{c}$ to give the approximated output time history $\boldsymbol{y}$ (Equation (2.30)).

To train the model, the matrix $\boldsymbol{X}_{train} = \boldsymbol{A}(\boldsymbol{u}_{train})\boldsymbol{G}$ is constructed with the training

input vector $\boldsymbol{u}_{train}$, then the coefficients vector $\boldsymbol{c}$ is found minimizing the sum of squared residuals with the training output $\boldsymbol{y}_{train}$ as in Equation (2.31).

$$\boldsymbol{y} = \boldsymbol{A} \ \boldsymbol{G} \ \boldsymbol{c} = \boldsymbol{X} \ \boldsymbol{c} \tag{2.30}$$

$$\boldsymbol{c} = (\boldsymbol{X}_{train}^T \boldsymbol{X}_{train})^{-1} \boldsymbol{X}_{train}^T \boldsymbol{y}_{train} \tag{2.31}$$

$$\boldsymbol{A} = \begin{bmatrix} u(0) & 0 & \dots & 0 \\ u(1) & u(0) & \dots & 0 \\ \vdots & & \ddots & \vdots \\ u(n) & u(n-1) & \dots & u(n-M) \end{bmatrix}, \boldsymbol{G} = \begin{bmatrix} g_0(0) & g_1(0) & \dots & g_l(0) \\ g_0(1) & g_1(1) & \dots & g_l(1) \\ \vdots & & & \\ g_0(M) & \dots & \dots & g_l(M) \end{bmatrix}, \boldsymbol{c} = \begin{bmatrix} c_1 \\ c_2 \\ \vdots \\ c_L \end{bmatrix}$$

$$\tag{2.32}$$

However, with this approach only M points are considered for the evaluation of the filters. The efficiency of the identification can be improved removing this truncation using the recursive relation in Equation (2.33) to directly construct the matrix $\boldsymbol{X}$ from the input time history [12]. In this way the length of the memory considered is determined by the longest stretching filter, that is also the one of highest order, as can be seen from Figure 2.1, and M is not anymore a parameter of the model.

$$x_0[k] = \sqrt{\alpha}x_0[k-1] + \sqrt{1-\alpha}v[k], \quad x_0[0] = 0$$
$$x_l[k] = \sqrt{\alpha}x_l[k-1] + \sqrt{\alpha}x_{l-1}[k] - x_{l-1}[k-1], \ l = 1,...L, \quad x_l[0] = 0 \tag{2.33}$$

Once the model is trained, the modelling performance can be verified foreseeing the output for a generic input. The model will best perform inside the identified frequency range $\omega \in [0.5, 3]Hz$: for instance it is considered a sinusoidal input $\boldsymbol{u}_{valid}$ with frequency $\omega_{valid} = 1.3Hz$. The regression matrix $\boldsymbol{X}_{valid}$ is constructed with the recursive relation in Equation (2.33), considering parameters $L = 3$ and $\alpha = 0.85$, and multiplied by the coefficients vector to obtain the corresponding output time history $\boldsymbol{y}_{valid}$ as in Equation (2.30). The result obtained is compared with the output simulated with the Matlab function *lsim()* in Figure 2.7.

The performance of the identification can be also checked in terms of system impulse response function in time $h_{lag}(k)$ and system transfer function $H_{lag}(z)$ in Equation (2.29) in frequency. The former is obtained as a linear combination of Laguerre functions with the identified coefficients, as shown in Equation (2.34). While the latter is obtained writing in matrix form the finite summation of Laguerre filters $G_j(\omega)$ multiplied by the identified

coefficients $\boldsymbol{c}$ as in Equation (2.35).

$$h_{lag}(k) = \sum_{l=1}^{L} c_l g_l(k) \tag{2.34}$$

$$H_{lag}(z) = \sum_{l=0}^{L} c_l G_l(z) = \begin{bmatrix} \boldsymbol{G}_0(z) & \boldsymbol{G}_1(z) & \dots & \boldsymbol{G}_L(z) \end{bmatrix} \boldsymbol{c} \tag{2.35}$$
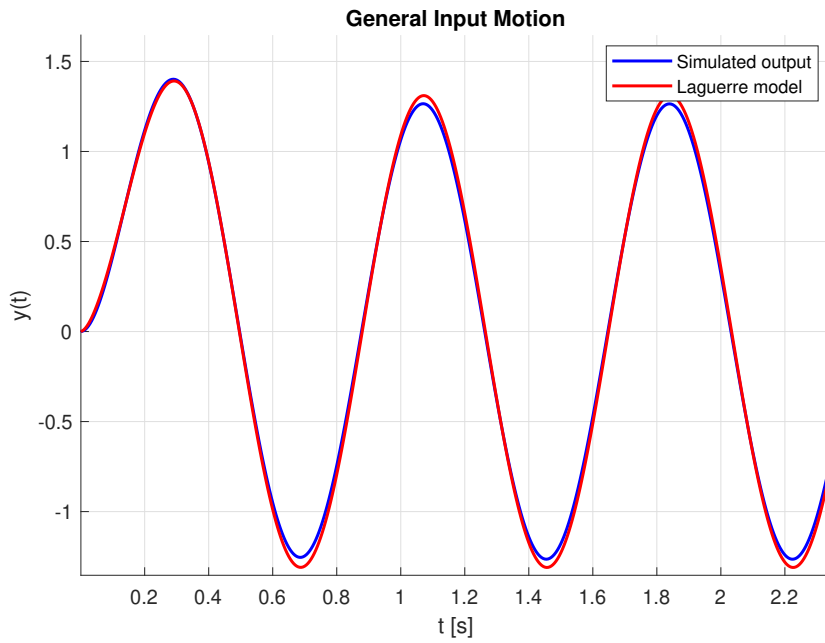

Figure 2.7: Comparison between the Laguerre model output and the output simulated with Matlab for sinusoidal input with frequency $\omega = 1.3Hz$. Identification parameters $L = 3$, $\alpha = 0.85$.
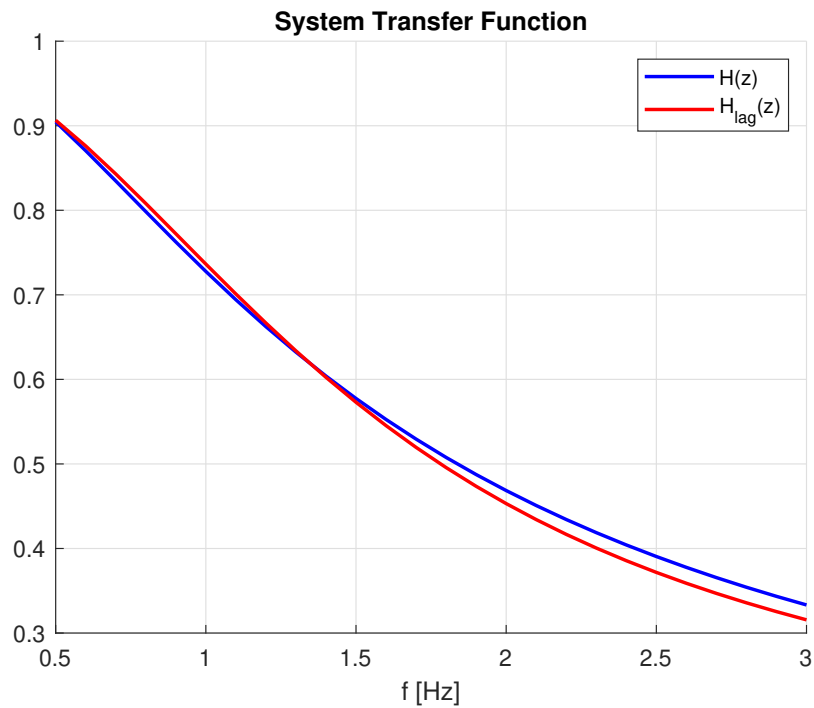
Figure 2.8: Comparison between the Laguerre model transfer function and the first order system transfer function. Identification parameters $L = 3$, $\alpha = 0.85$.
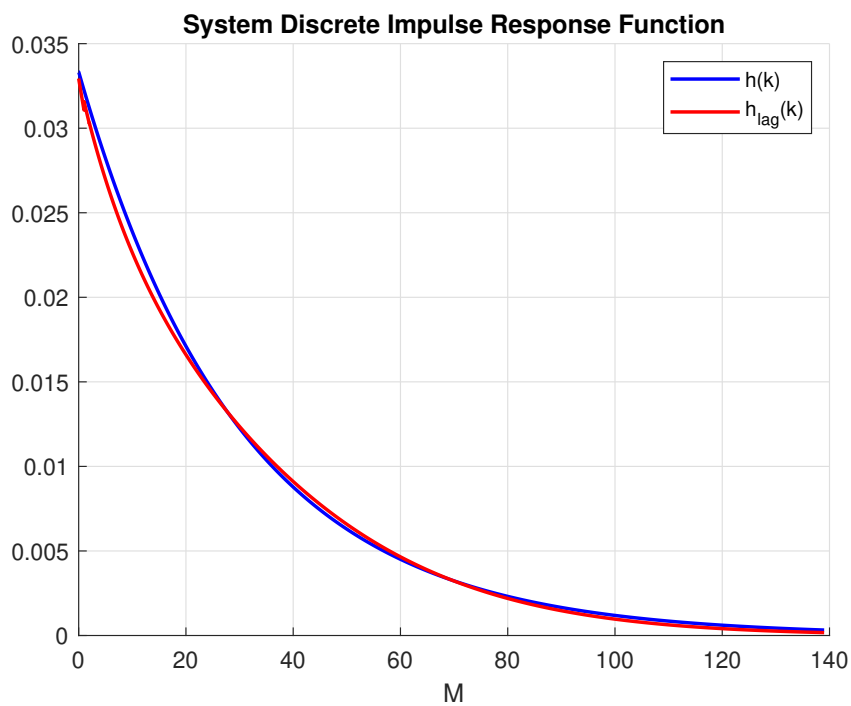
Figure 2.9: Comparison between the Laguerre model impulse response function and the first order system impulse response function. Identification parameters $L = 3$, $\alpha = 0.85$.

The system output is quite well reconstructed by the Laguerre model. Some differences can be noticed in time domain on the peaks of the curves and this is confirmed by the not exact correspondence between the two transfer functions in the selected excitation frequency. The identification can be improved with a better choice of model parameters as shown in Subsection 2.5.1.

2.5.1. Model parameters identification

The identified Laguerre model is ruled by two parameters: the highest order of the filters L to be included and the decay factor α. Considering the discrete formulation of the Laguerre filters in Equation (2.16), used in [20], α can have a value between 0 and 1. This parameter determines the speed of decay of the filter: higher values result in slower decay (see Figure 2.4). Therefore, a first indication for the choice of the α value is the length of the effective memory that the model is wanted to have. Analysing the filters in frequency domain, it can be seen from Figure 2.5, that higher alpha emphasizes more the lower frequencies.
Some guidelines for the choice of α are given in [9]. According to this guidelines a lower bound for α is set with Equation (2.36) where f_s is the sampling frequency. This suggestion is done with the intention of choosing a decay parameter such that the cutoff frequency of the highest filter is less than the highest input frequency of the system f_{max} [20]. While an upper bound (Equation (2.37)) is set to avoid overfitting: the final value of the highest order filter should be beneath an heuristic value, to capture the memory length precisely.

$$\alpha \geq (2 - \cos(\beta) - \sqrt{\cos(\beta)^2 - 4\cos(\beta) + 3})^2 \; with \; \beta = 2\pi\frac{f_{max}}{f_s} \qquad (2.36)$$

$$g_L(M) \leq 0.01 \qquad (2.37)$$

In the presented case the maximum frequency to be included in the model is the maximum training frequency: $f_{max} = 3Hz$. According to Equation (2.36) this leads to $\alpha_{min} = 0.8283$. While the maximum value for the parameter is set at $\alpha_{max} = 0.889$ because this causes the final value of the highest order filter to be $g_L(M) = 0.0096$. To have an experimental evidence of the validity of these guidelines, in Figure 2.10 is shown the system transfer function approximated with models trained with different values of the parameter α. The number of filters considered is set to $L = 3$. It is confirmed that values below and above the suggested limits give a bad approximation of the system transfer function. It is interesting to underline that among the values within the allowed range, values nearer to the upper bound give a better approximation.
It must be underlined that Equation (2.37) cannot be used if the recursive relation in

Equation (2.33) is used to define the model. Indeed, in this case the memory length M is embedded in the recursive relation and is not a parameter of the model anymore.
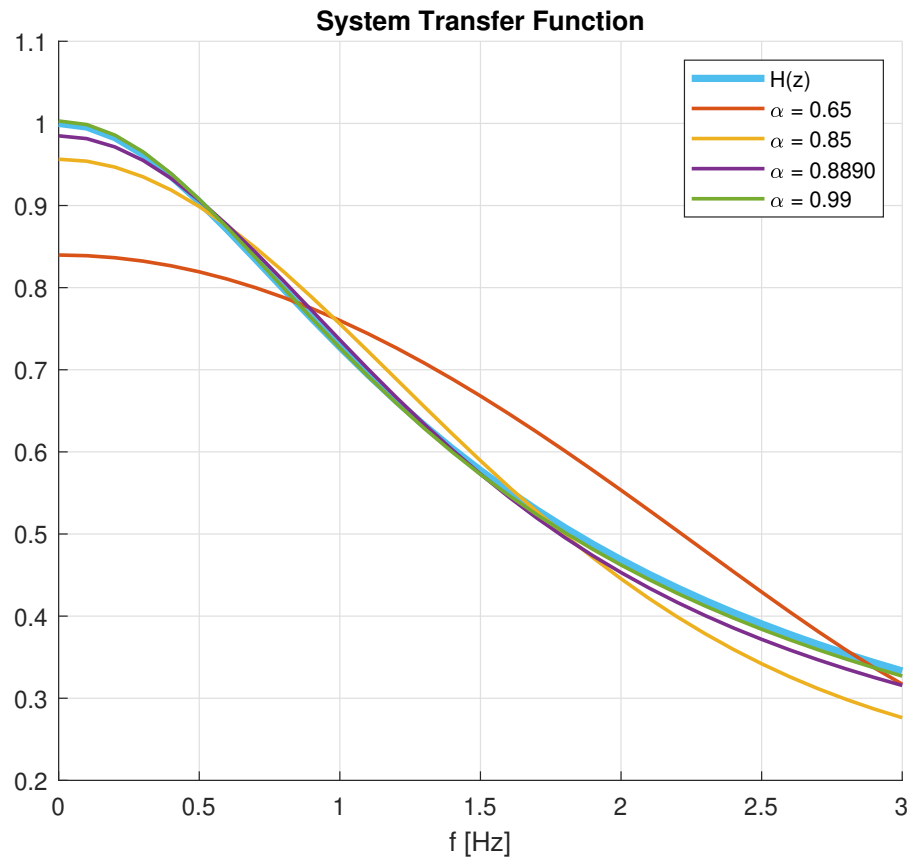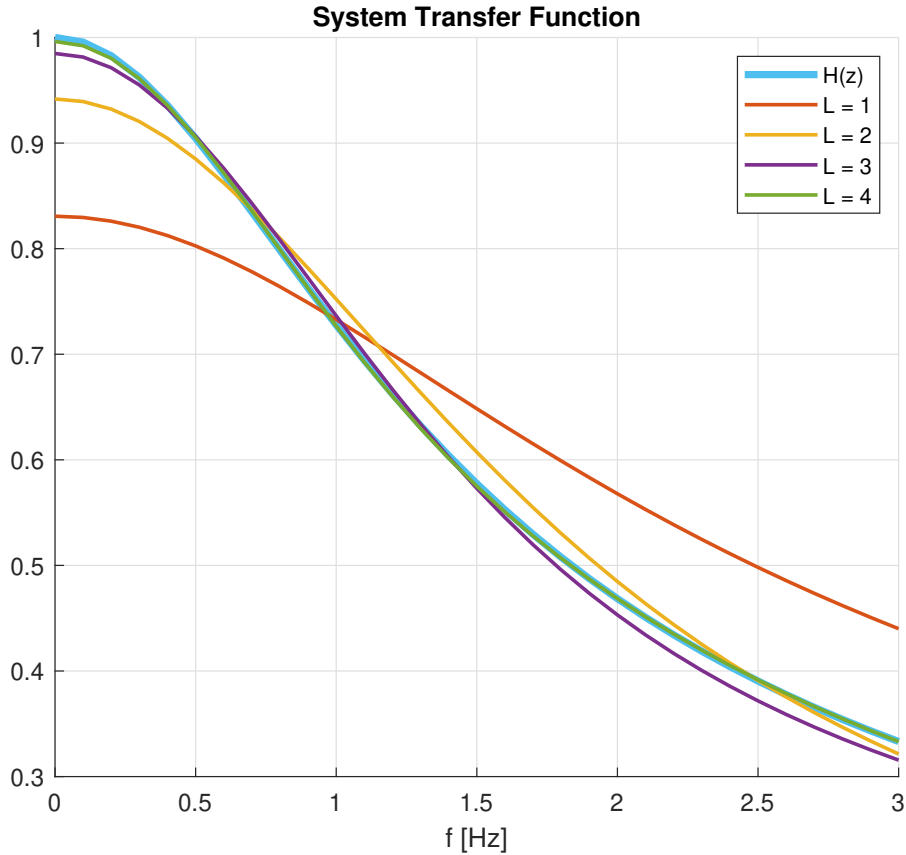

Figure 2.10: Comparison between the analytical transfer function and the Laguerre identified transfer functions with different values of the α parameter for the identification. Parameter L set to $L = 3$.

Figure 2.11: Comparison between the analytical transfer function and the Laguerre identified transfer functions with different values of the L parameter for the identification. Parameter α set to $\alpha = 0.889$.

The second parameter of the model is the number of filters to be considered. However, no specific guidelines have been mentioned in previous literature. As explained in Subsections 2.1 and 2.2, the approximation by orthonormal series expansion (Equation (2.11)) increases of accuracy as the number of considered terms L increases. This is shown in Figure 2.11, where the first order system transfer function is really precisely approximated already with four filters considered. However, increasing the number of filters has as a drawback the directly proportional increase of the unknowns to be identified during the model training, as it is shown in Section 2.3. Therefore, in more complex models training, a balance between accuracy and computational burden has to be found.

3 | Experimental Example on Langenuen Bridge Wind Tunnel Data

3.1. Langenuen Fjord Crossing Bridge

Figure 3.1: Langenuen suspension bridge as presented by Norconsult [10].

A first conceptual plan of the Langenuen bridge was presented by Norconsult in 2015. It consisted of a fjord crossing bridge, part of the project Coastal Highway Route E39, led by the Norwegian Public Roads Administration, to link Kristiansand and Trondheim with a continuous highway route [11]. This includes crossing two fjords: Bjørnafjorden and Langenuen. In Norconsult's report the bridge section was dimensioned with four road lanes, two shoulder lane and one pedestrian lane (Figure 3.2). The actual shape of the section was object of later studies with the aim of achieving good aerodynamic stability and also low construction cost [15].

The data used to test the model in the present work come from the wind tunnel characterization of different possible girder sections for the Langenuen bridge. The experimental

campaign was carried out in 2021 by Bergerund and Tørod for their Master Thesis work [1] in the wind tunnel of the Norwegian University of Science and Technology (NTNU) in Trondheim (see Section 3.2). Their aim was to investigate several girder shapes to estimate their aerodynamic stability limits to identify the best solution for the design of an innovative aluminium girder for the Langenuen. The different girder shapes were obtained deriving the section dimensions in function of two parameters: the height H and the angle θ as shown in Figure 3.3. These parameters were changed moving the section along a curve of constant torsional stiffness. This was decided based on the report of Dr. techn. Olav Olsen [15] where a sufficient aerodynamic stability limit was achieved mainly with an increase of torsional stiffness. For the analysis in the present work, the wind tunnel tests of four girder shapes reported in Table 3.1, were selected.
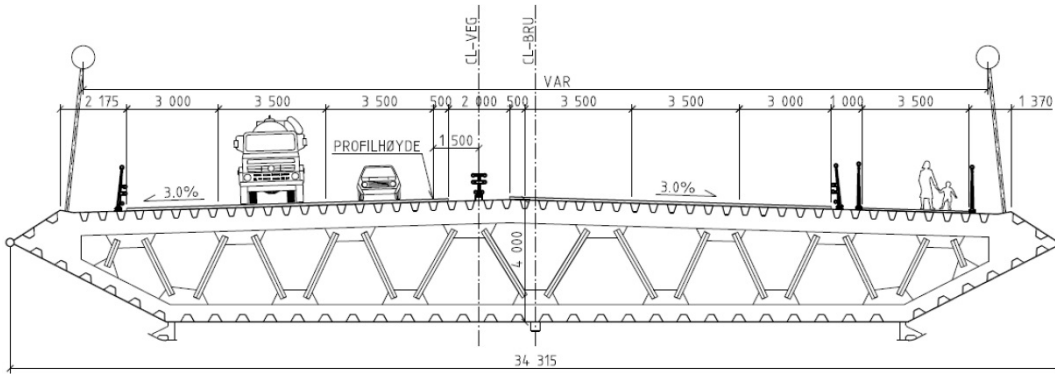
Figure 3.2: Steel box girder as presented by Norconsult in 2015 [10].
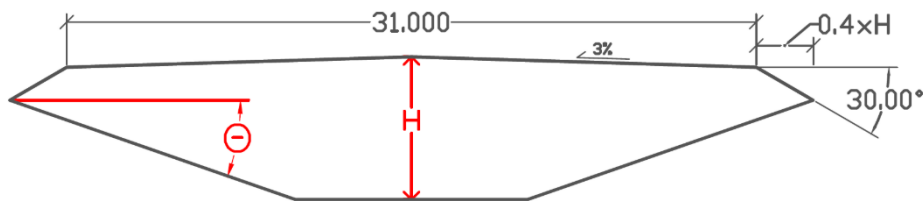
Figure 3.3: Parametric girder section [5].

Code	H [m]	$\theta[°]$	Girder Shape
LN21-5200	5.2	25.3	
LN21-5500	5.5	20.8	
LN21-5800	5.8	18.3	
LN21-6100	6.1	16.7	

Table 3.1: Experimental campaign girder shapes [1]

3.2. Experimental Setup

The main aim of wind tunnel testing of a bridge cross-section is to determine experimentally the aerodynamic derivatives (ADs). There are two kinds of wind tunnel tests: free vibration and forced vibration tests, better described in Subsections 1.2.1 and 1.2.2. The data used in this work come from a forced vibration test carried out NTNU wind tunnel which is provided with an enhanced forced vibration test rig capable of forcing the section model in nearly any desired motion [19].
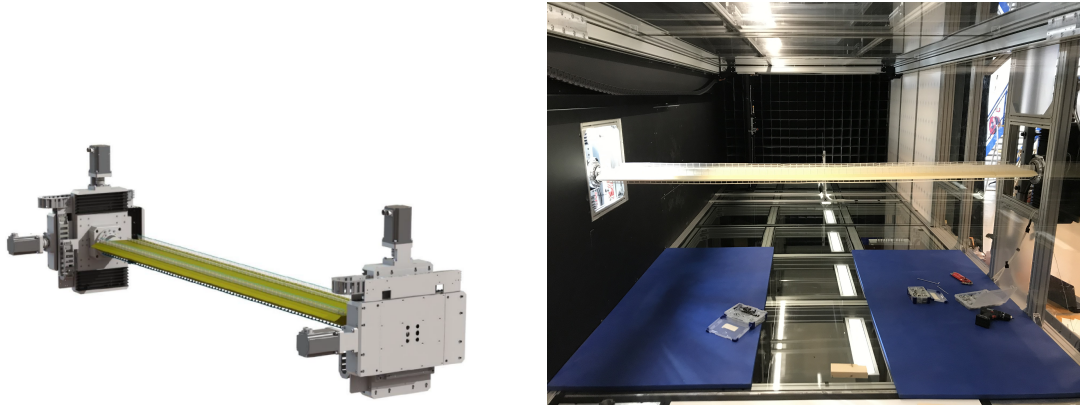
Figure 3.4: NTNU test vibration rig: 3D model and experiment preparation in the tunnel.

This forced vibration rig consists in two 3-DOF actuators that clamp the bridge model on both sides as shown in Figure 3.4. Between each actuator and the clamp holding the model its placed a 6-axis force/torque transducer as can be seen in Figure 3.5. These load cells can measure the self-excited forces acting on the model during the imposed motion. For the identifications of the aerodynamic derivatives the model has been forced with three different single-harmonic motions: horizontal, vertical and torsional, each at two different wind speeds. Each oscillatory motion was carried out at eight different oscillation frequencies, so to give 16 data points for each AD. Each motion has then also been tested in still air to be able to remove the inertia contribution from the measured forces during the data processing.
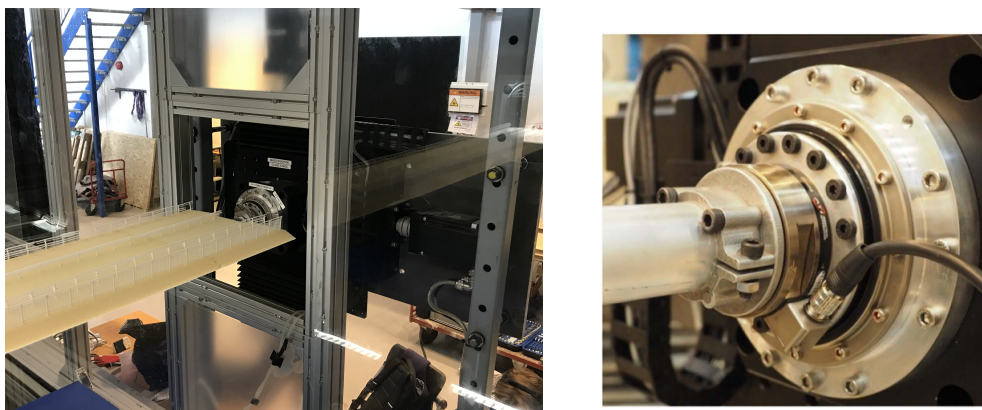
Figure 3.5: On the NTNU test rig actuators the load cells are placed between the clamp holding the model and the actuator.

An overview of testing setup parameters is given in Table 3.2.

The collected data have been used to test the Laguerrian model explained in Section 2.4.

To be used for effective model identification all input-output time series have been processed as explained in the next section.

Amplitude of vertical vibration:	$\pm 1cm$	Tested velocities:	Variable between models
Amplitude of horizontal vibration:	$\pm 2cm$	Tested frequencies:	0.25, 0.5, 0.8, 1.1, 1.4, 1.7, 2.0, 2.5 Hz
Amplitude of torsional vibration:	$\pm 1.0°$	Reduced velocity range:	From 0.72 up to 3.64
Sampling frequency:	$200Hz$	Duration of time series:	ca. 220s

Table 3.2: Induced motion characteristics. [5]

3.3. Data Processing

The measurement data from the load cells of the testing rig are given relative to local reference systems. Therefore all the measurements have been converted in global coordinates referred to a fixed reference system as shown in Figure 3.6. However, the measured forces are not yet the self-excited forces needed. In general the total force acting on a section model can be expressed as in Equation 3.1.

$$\boldsymbol{F}_{tot}(\boldsymbol{X}, \dot{\boldsymbol{X}}, \ddot{\boldsymbol{X}}, U, v, w) = \boldsymbol{F}_E + \boldsymbol{F}_G + \boldsymbol{F}_I(\dot{\boldsymbol{X}}) + \boldsymbol{F}_B(U, v, w) + \boldsymbol{F}_{Se}(U, \dot{\boldsymbol{X}}, \ddot{\boldsymbol{X}}) + \boldsymbol{F}_S(U)$$

(3.1)

Where $\boldsymbol{F}_E$ are the external forces due to clamping, those are cancelled out summing together forces measured on the same axis of the two load cells. $\boldsymbol{F}_G$ is the static gravitational load and $\boldsymbol{F}_S$ is the static wind load: these are removed subtracting their mean value to all the time series. $\boldsymbol{F}_I$ is the inertia contribution, which is removed subtracting the force measurements collected in still air. $\boldsymbol{F}_B$ is the buffeting response, function of the wind speed and the turbulence main components, in these case it can be neglected as the tests have been carried out in laminar flow. Therefore wind speed V_{Rel} relative to the deck is coincident with the mean wind speed U. What is left are the self-excited forces and moments $\boldsymbol{F}_{Se}$ which are considered positive as shown in Figure 3.7. All the named quantities have three components, namely the force in each degree of freedom.

Finally, all the time series have been filtered, removing all components higher than 3.0 Hz. Then the first half of the time series has been further filtered removing all components

higher than 0.8 Hz. This allowed to remove noise, but also the vibration contribution due to possible higher frequencies resonances of the model.

A check on the memory length for the initial part of the time series is been also carried out. Looking at Equation (2.32) it can be seen that the matrix of the input $\mathbf{A}$ is lower triangular because of lack of memory in the first $M-1$ points of the time history. To be sure that no data is lost, is been checked that the actual imposed motion starts after at least one memory length from the start of the recorded signal. In the considered Laguerrian model the length of the memory is indirectly determined by the higher order filter, which is also the one stretching further, as it is explained in Section 2.5.

With the values of the parameters L, α chosen for the analysis, as can be seen from Figure 3.10, the memory is about $M = 40$, that, with a sampling frequency of $200 Hz$, corresponding to a sampling time of $0.005s$, results in a memory length of $0.20s$. All the imposed motions start after $8s$ from the beginning of the recording, so there is no risk of data to be lost.

To have more data points for model identification, time series recorded at different wind velocities were stacked together. To be able to do this the recorded data were sent trough an adimensionalization process that made them independent from the wind speed. The quantities used to make the data dimensionless were the width of the section B, the length of the model $L = 2.68m$, the air density ρ and the wind mean velocity during the experiment V.

The time was made dimensionless with Equation 3.2. While force and momentum data were adimensionalized with Equation 3.3 and 3.4.

$$s = \frac{V}{B}t \tag{3.2}$$

$$f = F\frac{1}{\rho LBV^2} \tag{3.3}$$

$$m = M\frac{1}{\rho LB^2V^2} \tag{3.4}$$

The dimensionless time series from different wind velocity test on the same section can then be stacked together in a single input-output time series and could be used to train the model with Equation (3.5). However, after the adimensionalization with Equation (3.2), the Δs is different for each wind speed. To be able to stack the data together the lower wind speed data were re-sampled with a longer Δs, equal to the one of the highest wind speed data.

In this way a set of $3L$ coefficients $\mathbf{C}$ were found for each combination of degrees of freedom and knowing V, B, L, ρ of a specific section the dimensional output can be reconstructed.

In Figure 3.8 is reported the model flow chart: once the model for a section is trained, any input can be adimensionalized, the dimensionless output modelled, and finally the real output reconstructed.

In the present work the analysis is been limited to the modelling and evaluation of the self-excited lift and torque, disregarding the drag. Furthermore, as imposed motions, only vertical and torsional actions were considered.
This was done because the measured drag force was only 0.2% and 7% of the lift force in case of vertical and torsional imposed motions respectively. While, during the horizontal imposed motion the lift force was at least 80% smaller, and the torsional moment 86% smaller, than in the other two cases. Finally, the transfer functions related to drag force are highly nonlinear [20] and therefore not suitable for identification with a linear model.
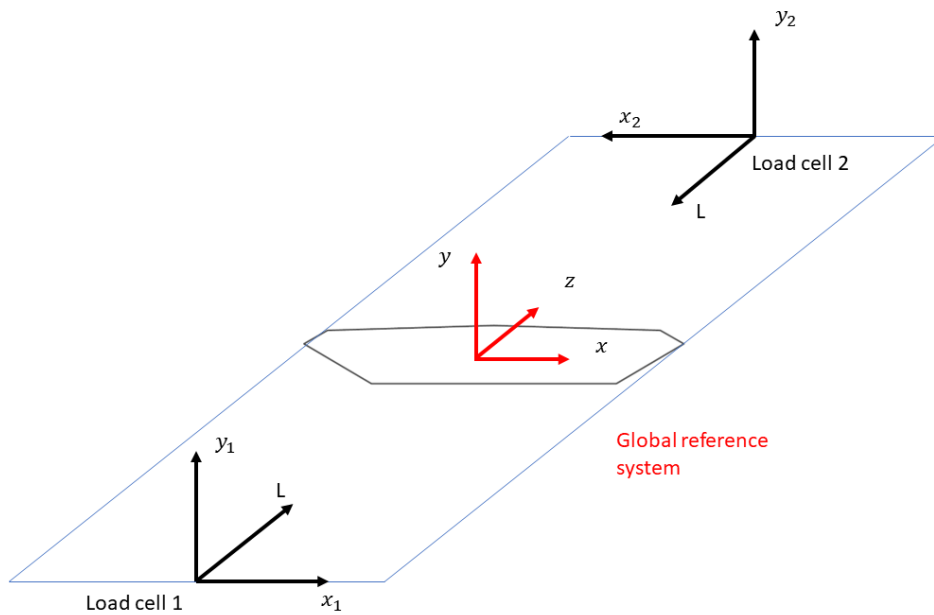
Figure 3.6: Reference system transformation from the local systems of the two load cells to a global system for the whole model (in red).
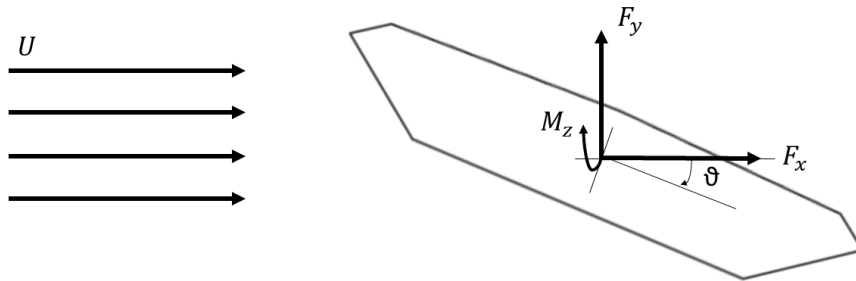
Figure 3.7: Self-excited forces on the section. U is the incoming wind flow, considered with negligible turbulence.
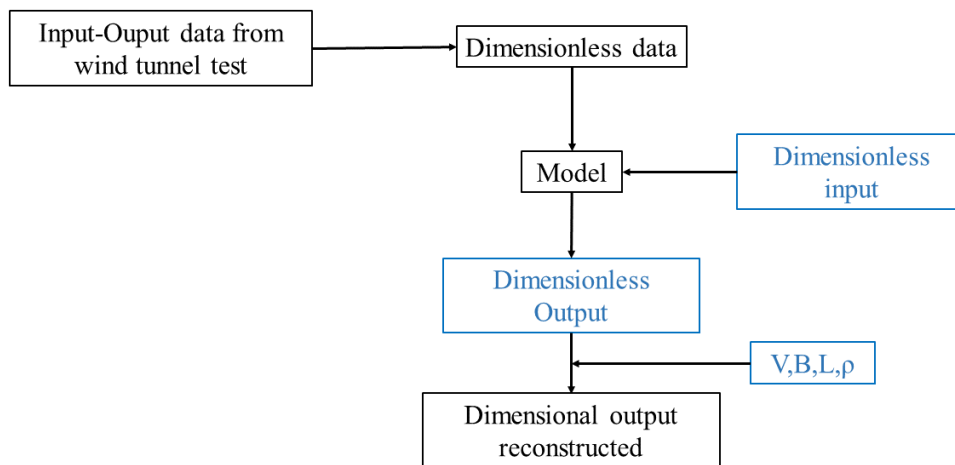
Figure 3.8: Laguerre self-excited prediction model flow chart

3.4.   Laguerre Model Training

A simple one degree of freedom example of the training phase of the Laguerrian model for self-excited forces identification was exposed in Section 2.5. A general three degrees of freedom training procedure has been developed in the present work expanding the model given in Equations (2.30)-(2.32). For each imposed motion vertical, horizontal and

torsional, the L coefficients relative to the transfer function to each degree of freedom need to be determined. This is done expanding the size of the matrices as in Equation (3.5). Here $\hat{\boldsymbol{X}}_v$ is a diagonal matrix, of which diagonal elements are equal regression matrices constructed with the recursive relation from Equation (2.33) with $v \in [y, x, \theta]$. Solving the linear least-squares problem in Equation (3.6) the vector $\boldsymbol{C}_v$ is identified, containing the $3L$ coefficients relative to the transfer functions from the generic input $v \in [y, x, \theta]$ to the three aerodynamic forces in $\boldsymbol{F}_v$. This procedure is repeated for all the three imposed motions, finding in total $9L$ coefficients $[\boldsymbol{C}_y, \boldsymbol{C}_x, \boldsymbol{C}_\theta]$ to fully characterize the system.

$$
\begin{bmatrix} \boldsymbol{F}_{yv} \\ \boldsymbol{F}_{xv} \\ \boldsymbol{F}_{\theta v} \end{bmatrix} = \begin{bmatrix} \boldsymbol{X}_v & 0 & \dots & 0 \\ 0 & \boldsymbol{X}_v & \dots & 0 \\ & & \ddots & \\ 0 & 0 & \dots & \boldsymbol{X}_v \end{bmatrix} \begin{bmatrix} \boldsymbol{c}_{yv} \\ \boldsymbol{c}_{xv} \\ \boldsymbol{c}_{\theta v} \end{bmatrix} = \hat{\boldsymbol{X}}_v \boldsymbol{C}_v \tag{3.5}
$$

$$
\boldsymbol{C}_v = (\hat{\boldsymbol{X}}_v^T \hat{\boldsymbol{X}}_v)^{-1} \hat{\boldsymbol{X}}_v^T \boldsymbol{F}_v \tag{3.6}
$$

Once the model of the system is characterized, it can be used to foresee the output from any input using the superposition principle.

$$
\boldsymbol{F}_x = \hat{\boldsymbol{X}}_x \, \boldsymbol{C}_x, \ \ \boldsymbol{F}_y = \hat{\boldsymbol{X}}_y \, \boldsymbol{C}_y, \ \ \boldsymbol{F}_\theta = \hat{\boldsymbol{X}}_\theta \, \boldsymbol{C}_\theta \tag{3.7}
$$

$$
\boldsymbol{F} = \boldsymbol{F}_x + \boldsymbol{F}_y + \boldsymbol{F}_\theta \tag{3.8}
$$

This forecast is done constructing a regression matrix for the input time history on each degree of freedom separately and, with the corresponding coefficients, its contribution to the output self-excited forces is determined as in Equation (3.7). Then the complete output of the system is calculated with Equation (3.8) summing together the contribution of each motion.

3.5.   Model Performance Evaluation

To assess the goodness of prediction of the above described model the input-output data relative to the tested girder section LN20-5500 have been considered. Firstly, the comparison has been done in time domain, comparing the measured forces time history with the aerodynamic forces calculated with the trained Laguerre model. This comparison has been carried out with the help of the Matlab [23] comparing toolbox `CompMet.m` [7] explained in detail in the following.

3.5.1.   Time series comparison toolbox

Considering the complexity of the identification is been decided to use a more quantitative procedure to analyse and display the identification results in time domain. The `CompMet.m` toolbox gives the possibility to compare time histories according to different metrics, the one chosen for this study are the phase shift, the peak values, the Root Mean Square (RMS) and the magnitude.

The phase shift M_ϕ is considered because linked to the ability of the aerodynamic model to capture the fluid memory effect. This specific indicator accounts for the mean phase discrepancy between the compared signals. The phase metric is calculated according to a user-defined parameter that represent a time that is considered to be a significant delay. In the present work a significant delay between two time histories is considered to be the one resulting in a phase lag of $5deg$.

The peak value metric M_p gives a global indication of the amplitude discrepancy between the signals. While, the RMS metric M_{rms} is related to the energy content of the signal, and gives an indication about the average amplitude discrepancies between the signals.

The mean metrics M_{muw} and M_{mw}, are time localized indicators for the difference of amplitude of the two signals. The exact amplitude of the aerodynamic forces is relevant as it is a design parameter for suspended bridges. The toolbox gives the possibility to calculate two distinct magnitude metrics, the difference among them is the application of the warping procedure. The not warped one (M_{muw}) is simply the RMS deviation of the two signals. This however, could give a very pessimistic result in case of phase shift between the compared signals.

This can be solved with the use of the dynamic time warping between the compared time histories to alleviate the local phase shifts at high frequency. This is done aligning the peaks of the compared time histories non linearly by stretching and not scaling as is shown, as an example, in Figure 3.9. This gives the possibility to give a good evaluation of local amplitude differences even if is present a phase shift between the signals.
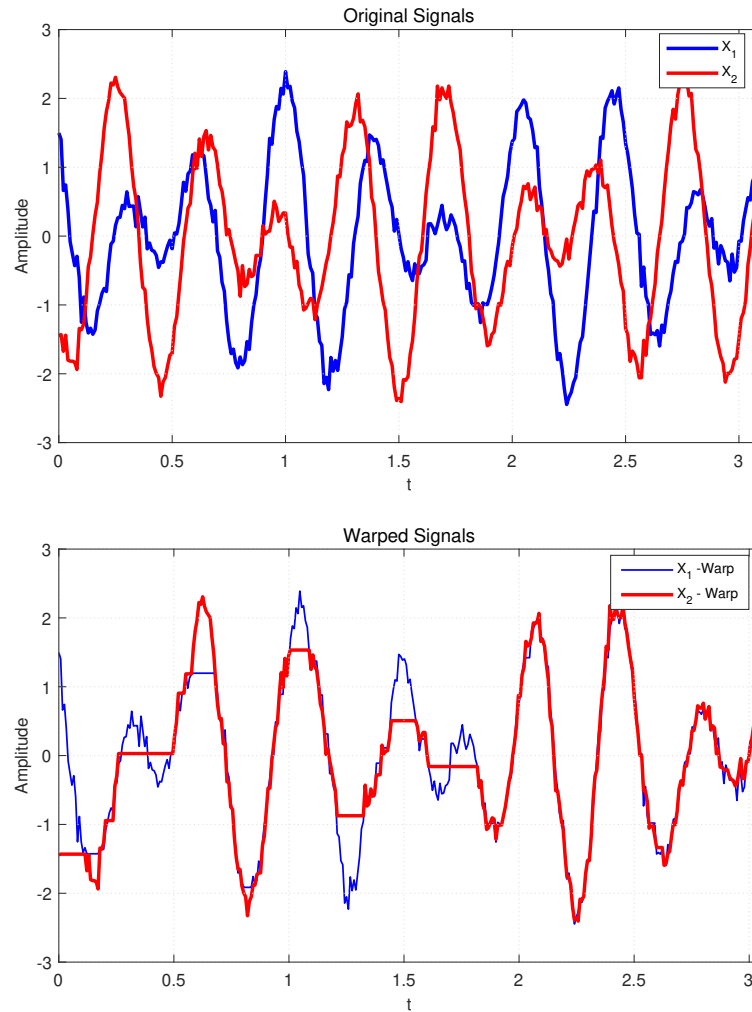
Figure 3.9: Example from [7] of Dynamic Time Warping of two generic signals.

3.5.2.   Results discussion in time domain

To have different metrics values for different excitation frequencies and also because of the high computational burden to calculate the magnitude warped metric M_{mw}, the comparison between the measured and the modelled time histories is been separated into intervals. The separation is been done according to the excitation frequencies, as shown in Figure 3.11. The metrics values for the two considered input motions for the section LN21-5200, with a mean wind velocity of 8.17 m/s, are shown in Figure 3.12 and 3.13.
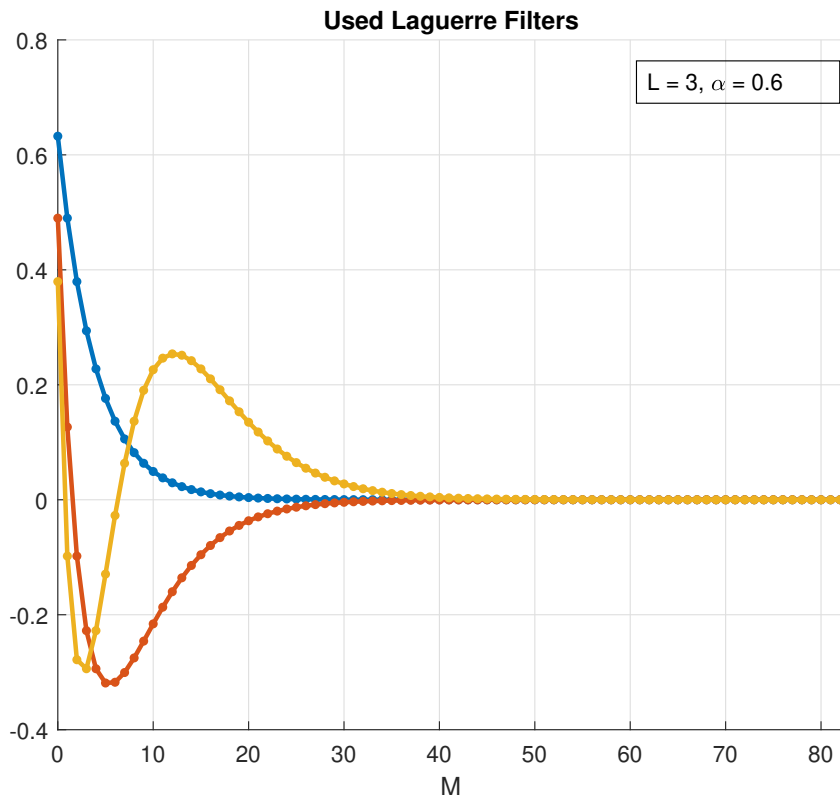
Figure 3.10: Laguerre filters used for the Langenuen data analysis.
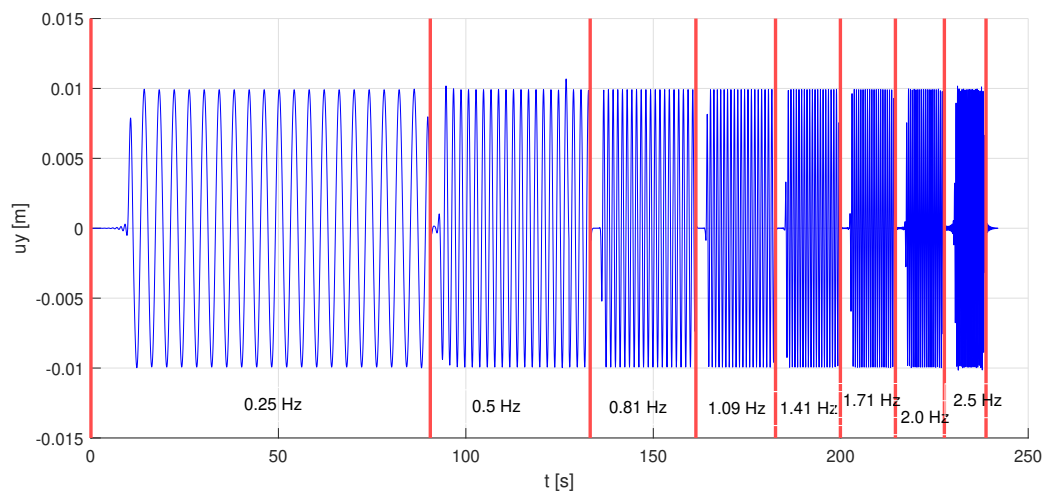
Figure 3.11: Time history cutting according to the different excitation frequencies $f \in [0.25, 0.5, 0.81, 1.09, 1.41, 1.71, 2.0, 2.5] Hz$.
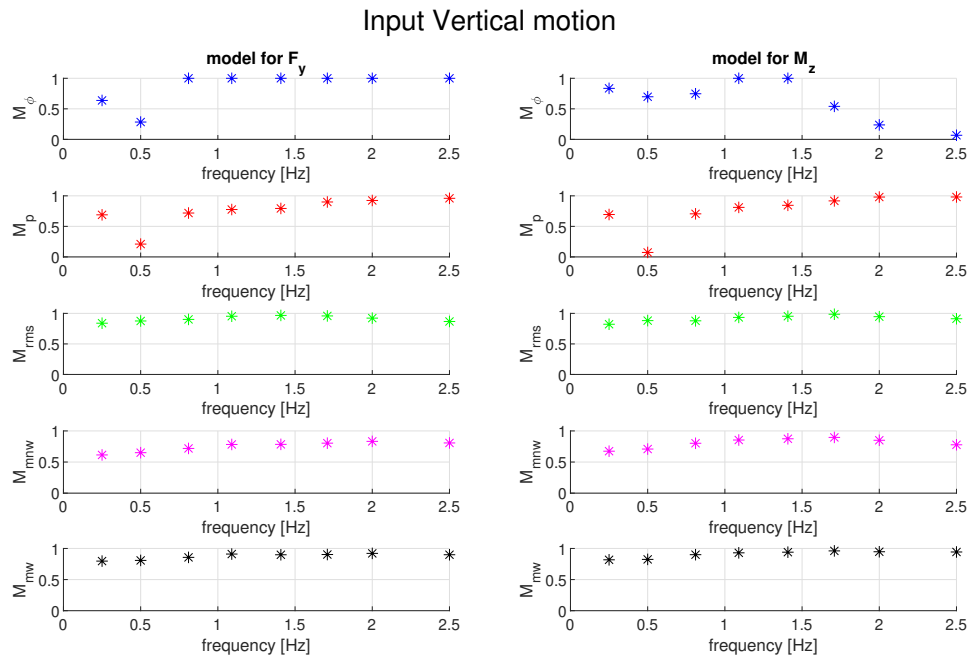
Figure 3.12: Values of goodness of fit metrics for vertical input motion and vertical and torsional output motions.
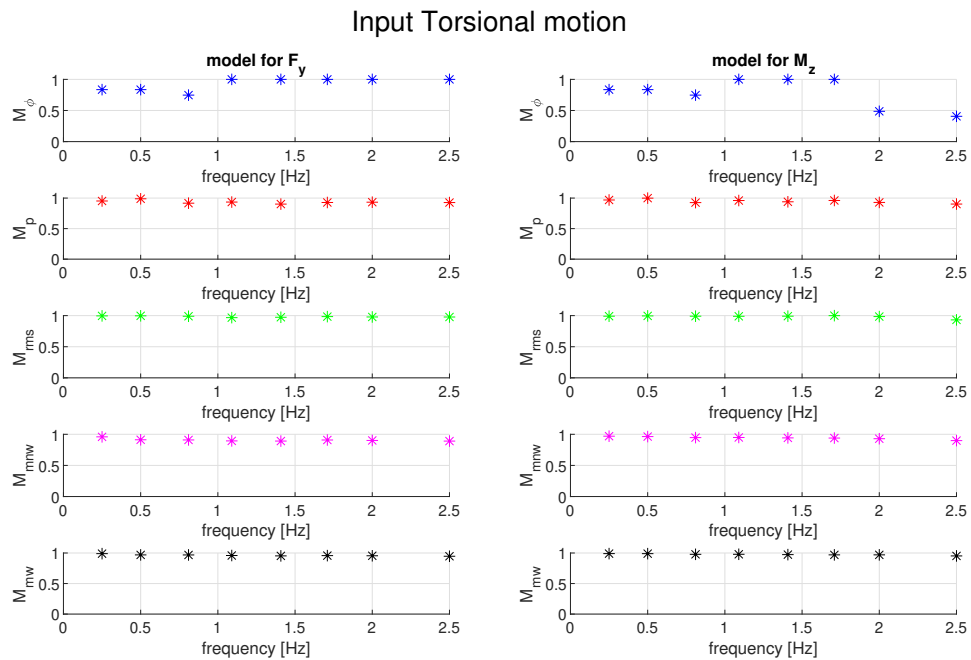
Figure 3.13: Values of goodness of fit metrics for torsional input motion and vertical and torsional output motions.

Overall the metrics values indicate a good fitting, specially for aerodynamic forces caused by input torsional motion. In particular the model has good capability of capturing the amplitude of the self-excited forces caused by a certain input motion. For some frequencies however, some metrics are quite low: in the following some representative cases are discussed to show if the low metrics values are attributable to limits of the comparing toolbox or lacks in the identification capabilities.

For instance it can be considered the output prediction for vertical and torsional excitation at 2.0 Hz, shown in Figures 3.14 and 3.15. Looking at the phase metric M_ϕ for the model of the self-excited torque in Figure 3.12 and Figure 3.13, at 2.0 Hz, it can be seen that it is quite low for both input motions. This is caused by the fact that the modelled time history is slightly out of phase compared to the measured one, as can be seen in Figure 3.14. In this case the delay between the two time histories is of 0.015 s that, at 2.0 Hz, corresponds to a phase difference of 10 deg. Because the sensitivity of the metric is of 5 deg this is evaluated as a considerable delay, leading to a low metric.
The phase is instead better reconstructed for the lift model at the same frequency (Figure 3.14); as it is confirmed by a higher M_ϕ metric, almost unitary.
For the same excitation frequency, it is interesting to notice the influence of the phase shift on the unwarped magnitude metric M_{mnw}. Looking at Figure 3.12, for the torque model at 2.0 Hz, it is visible how the M_{mnw} metric decreases together with the M_ϕ metric, even though the magnitude of the forces is quite correctly reconstructed (Figure 3.14, M_z time history). The dynamic time warping instead avoids the magnitude metric to be influenced by phase shifts, as can be seen from the M_{mw} metric, which remains high even in case of low phase metric.
The correctness of the magnitude warped metric is further confirmed by the fact that it mirrors the RMS metric (M_{rms}), showing that the model is capable of correctly reconstruct the energy content of the signal, even in case of phase shift.
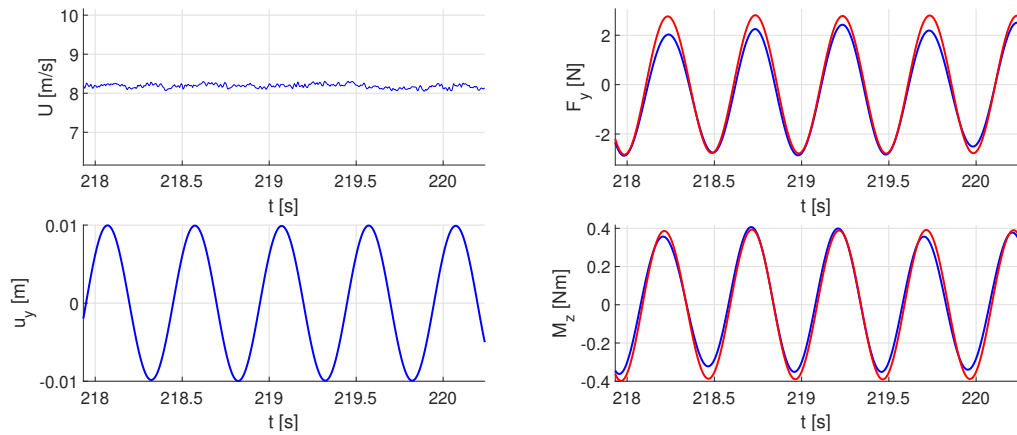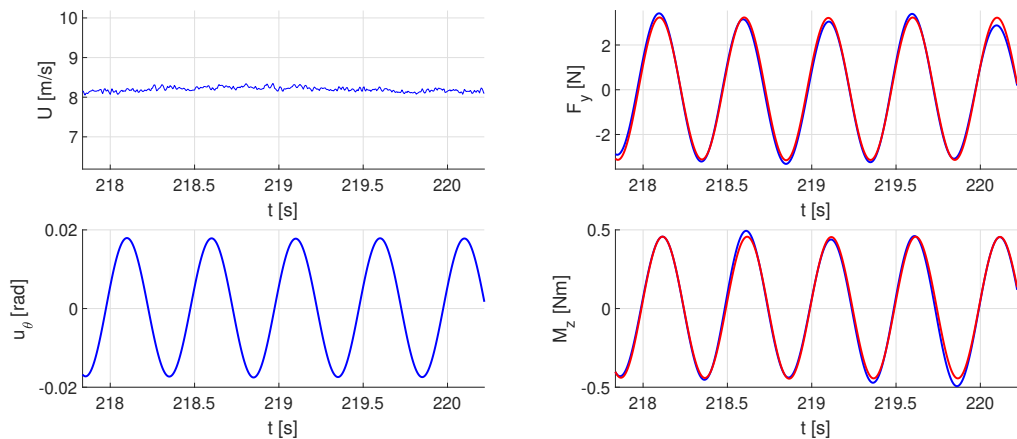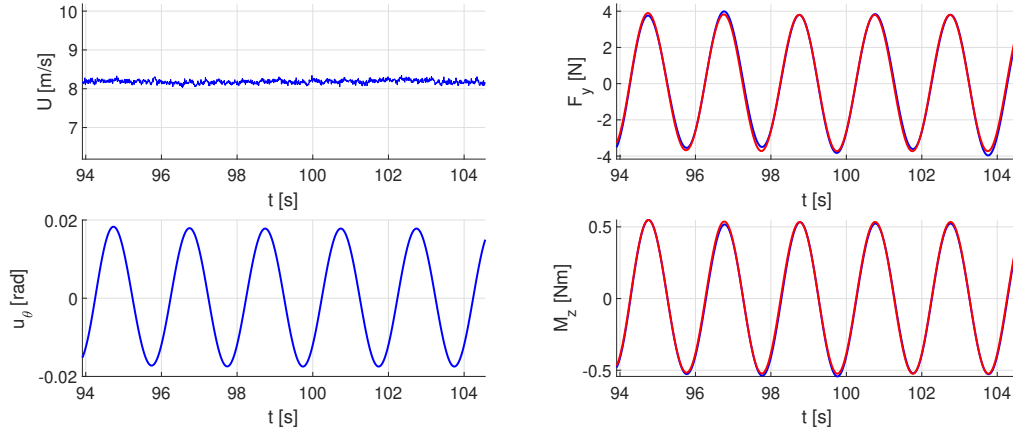
Figure 3.14: Particular of time histories. Blue = experimental data, Red = Laguerre model. Input vertical motion. Excitation frequency 2.0 Hz. Section LN21-5200. Good M_{mw} metric but poor M_ϕ due to phase shift.
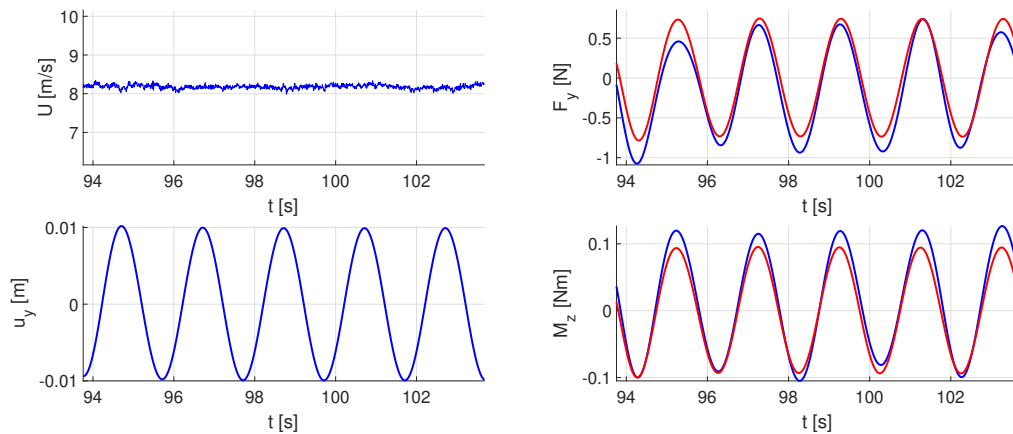

Figure 3.15: Particular of time histories. Blue = experimental data, Red = Laguerre model. Input torsional motion. Excitation frequency 2.0 Hz. Section LN21-5200. Good M_ϕ metric.

It can be noted from the metrics in Figures 3.13-3.12 that some of them are lower for low excitation frequencies, specially for the input vertical. This is mainly caused by low frequency noise that was not filtered out, that has particular influence on the metrics if the magnitude of the measured aerodynamic force is quite low, as it is the case of the lift and torque for vertical imposed motion, for instance at 0.5 Hz in Figure 3.17. Indeed, for the same frequency but with input torsional motion (Figure 3.16) the signals magnitude is way higher and the signal is almost perfectly reconstructed. This leads to almost all

unitary metrics for the torque model. Furthermore, during the experimental campaign some external action hit the model causing a peak in the measured force. This causes the peak metric M_p to drop for this frequency.

Figure 3.16: Particular of time histories. Blue = experimental data, Red = Laguerre model. Input torsional motion. Excitation frequency 0.5 Hz. Section LN21-5200.

At the same frequency with vertical imposed motion in Figure 3.17 it can be seen the case of bad reconstruction of the magnitude of the force, in particular the modeled force underestimates the real one. This is mirrored by a slight decrease in the magnitude metric, specially for the lift model in Figure 3.12.

Figure 3.17: Particular of time histories. Blue = experimental data, Red = Laguerre model. Input vertical motion. Excitation frequency 0.5 Hz. Section LN21-5200. Model underestimates the force, leading to poor M_{mw}.

In conclusion, the most representative metrics to evaluate the identification correctness

can be reduced to a couple. The phase metric M_ϕ to assess the mean phase difference between the time histories. And the magnitude warped metric M_{mw} to assess the magnitude reconstruction independently from the phase. Also the peak metric M_p, however, is useful to have a global indication of the capability of the model to capture the maximum amplitude of the forces.

3.5.3. Experimental parameters identification

The model exposed in Section 2.4 depends on two parameters: the number of filters considered L and the decay parameter α. In the present work is been investigated how the goodness of the prediction model depends on the value of these two parameters. Since the computational burden of training of the model is very low, the investigation is carried out with a numerical method. This is done predicting the system output for different values of the parameters and comparing the result with the actual measured output with the help of the comparing toolbox `CompMet.m` [7] (Subsection 3.5.1). This analysis has been carried out on the same section considered above, but considering just the portion of time histories corresponding to the excitation frequency at 1.09 Hz. The results are reported in the following figures.
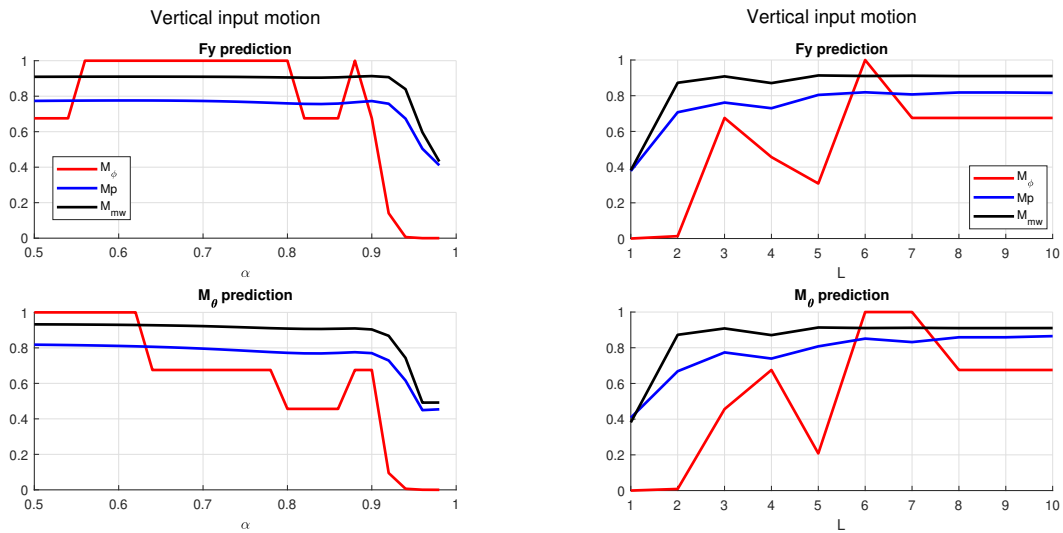
Figure 3.18: Vertical input motion at $1.09 Hz$ parameters identification.
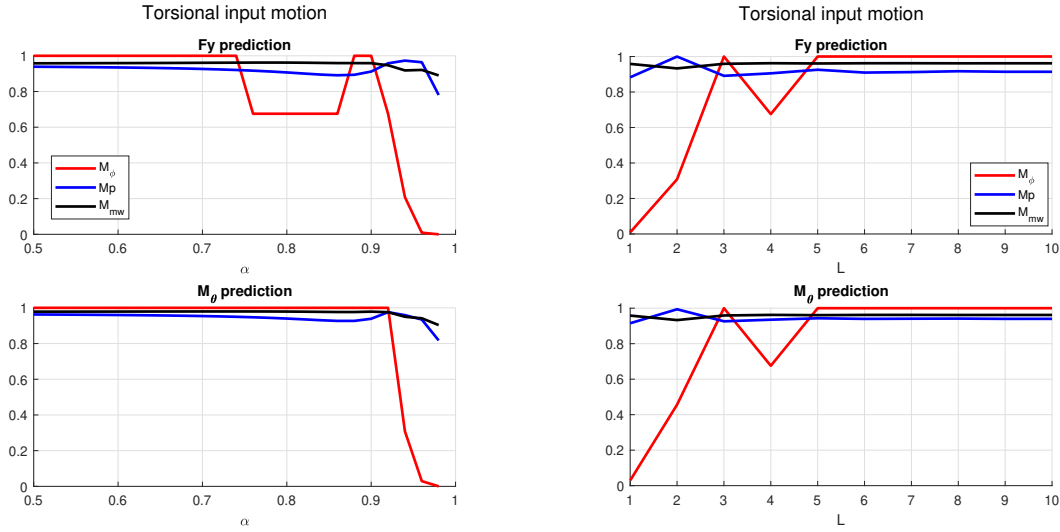
Figure 3.19: Torsional input motion at $1.09Hz$ parameters identification.

Looking at Figures 3.18-3.19, the Magnitude Warped metric (M_{mw}) stays quite constant for any value of α smaller than 0.9. The same holds for the Peak Metric (M_p). The Phase Metric (M_ϕ) instead seems to have some dependency on α specially for the vertical input motion. In particular the results suggest that the model performs better for values of $\alpha < 0.65$. Which means faster decaying filters (Figure 2.4). Therefore, the optimal value for the decay parameter in the present work is set to $\alpha = 0.60$.

For what concerns the number of filters to consider, in general the goodness of the approximation with Laguerrian expansion basis increases with the number of terms included. However, also the number of unknowns to determine has the same trend. The results obtained show, in Figure 3.19, that for the torsional input good metrics are obtained already with three filters, and the results become invariant respect to parameter L from $L > 5$. The trend of the metrics for the vertical input in Figure 3.18 in function of L is less clear. The peak and magnitude metrics stabilize after three filters, however the Phase metric settles only for $L > 8$.

In the present work, it is concluded that three filters $(L = 3)$ are an acceptable compromise between keeping very low computational burden and acceptable quality of the results. Following what the experimental results suggest, the decay parameter is been set to $\alpha = 0.60$.

3.5.4. Multiple section testing

To prove the independence of the Laguerre expansion basis model for self-excited forces prediction on the girder geometry, it has been tested on different girder shapes. The parameters for the model have been selected, according to Subsection 3.5.3, as $\alpha = 0.6, L = 3$ and the phase metric sensitivity is left on 5 deg. For this experimental test four section geometries tested at $8m/s$ were considered among all the girder geometries in Table 3.1 tested by [1].

As shown in Section 3.5.2, the most representative metrics for results evaluation are the phase metric (M_ϕ), the peak metric (M_p) and the magnitude warped metric (M_{mw}). Therefore only these three metrics were calculated for the different geometries model evaluation. An overview of the results with torsional motion as input is shown in Figure 3.20.
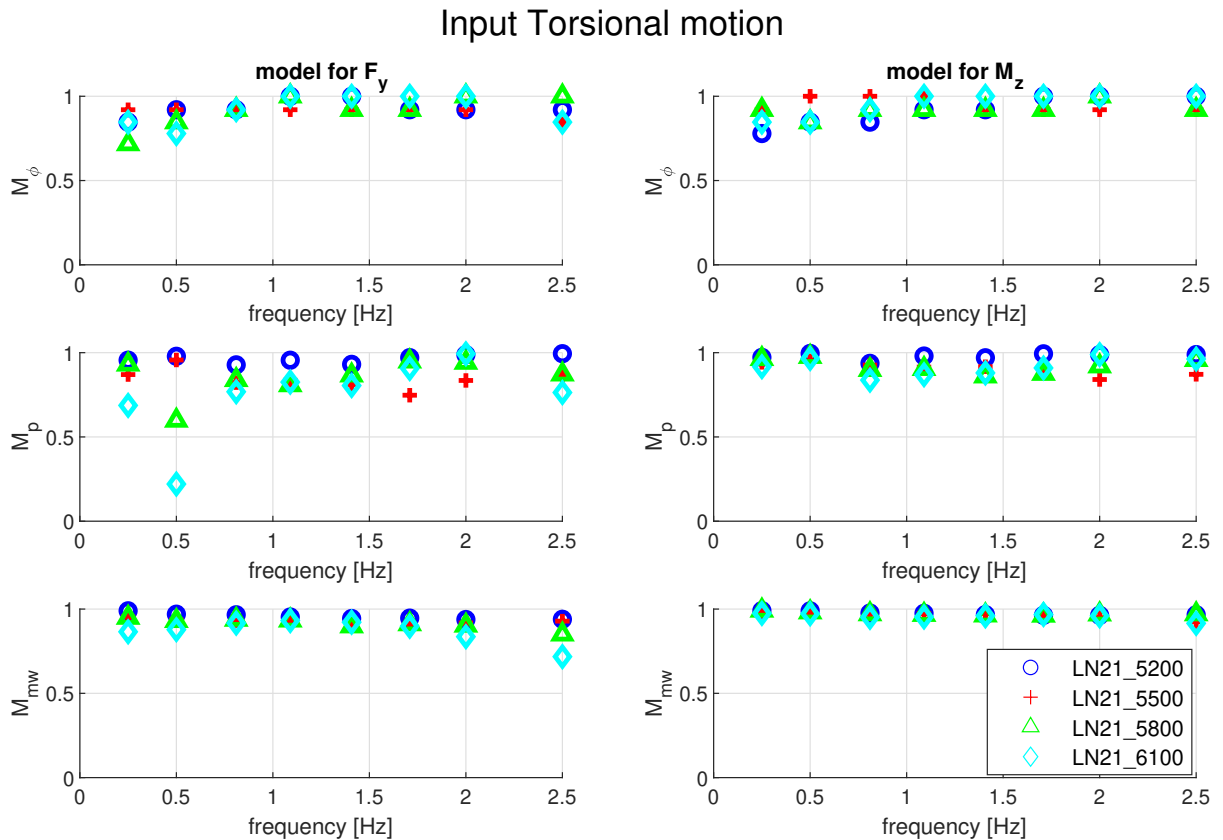
Figure 3.20: Assessment of model performance on different girder geometries. The graphs display values of goodness of fit metrics for torsional input motion to vertical and torsional output motions, for different excitation frequencies. The average wind speed of the test is $8m/s$. Model parameters are $L = 3$ and $\alpha = 0.6$.

Overall, very similar indexes values are obtained for different geometries with small discrepancies. Most of the deviations are observed in the lift model, in particular for section LN21-6100 for the first and last excitation frequencies. In these cases the model overestimate or underestimate the real force. The plunging of the peak metric at 0.5 Hz for sections LN21-6100 and LN21-5800 is caused by an error during the measurement campaign and is not relevant for the present discussion.

In general the presented model is proved not to have specific dependency on the girder geometry.

3.5.5.   Results discussion in frequency domain

For a complete assessment of the model, a comparison also in frequency domain is been carried out. In particular the system transfer functions from the two main inputs, vertical and torsional, to the lift and torque, have been determined with aerodynamic derivatives (Section 1.2) and Laguerre filters approximation. The comparison between the results gives an interesting overview of the Laguerre identification model underlining strengths and weaknesses.

The transfer functions between the different degrees of freedom can be expressed with couples of aerodynamic derivatives as shown in Equation 1.17. Their values for discrete reduced frequencies are found experimentally for the girder geometries considered in the present work by Bergerud and Torød [1].

The transfer functions can be also expressed as linear combination of Laguerre filters in frequency domain as shown in Equation (2.35).

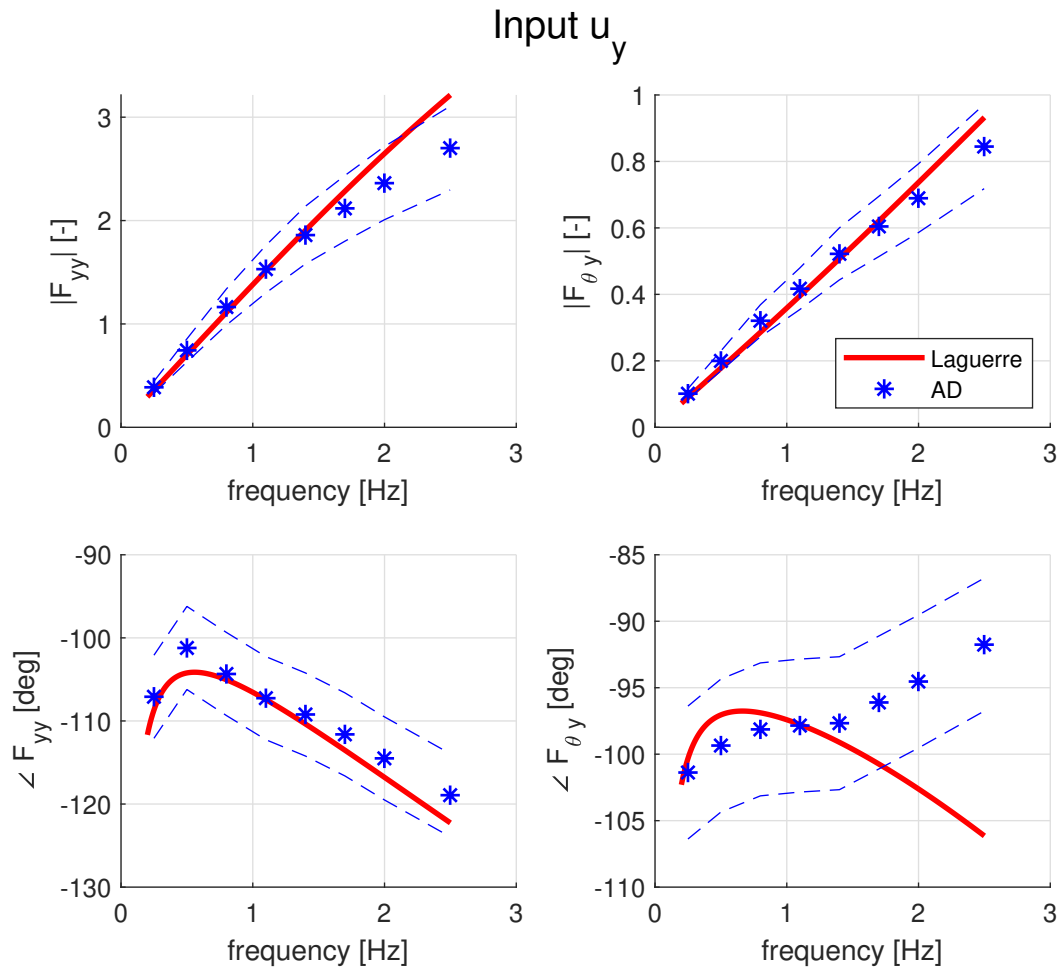The results are shown in Figures 3.21-3.22.

Figure 3.21: Module and phase of the transfer functions linking the vertical motion to the lift and the torque. Dashed lines show intervals of $\pm 15\%$ for the module and $\pm 5deg$ for the phase respect to the transfer function calculated with experimental aerodynamic derivatives.

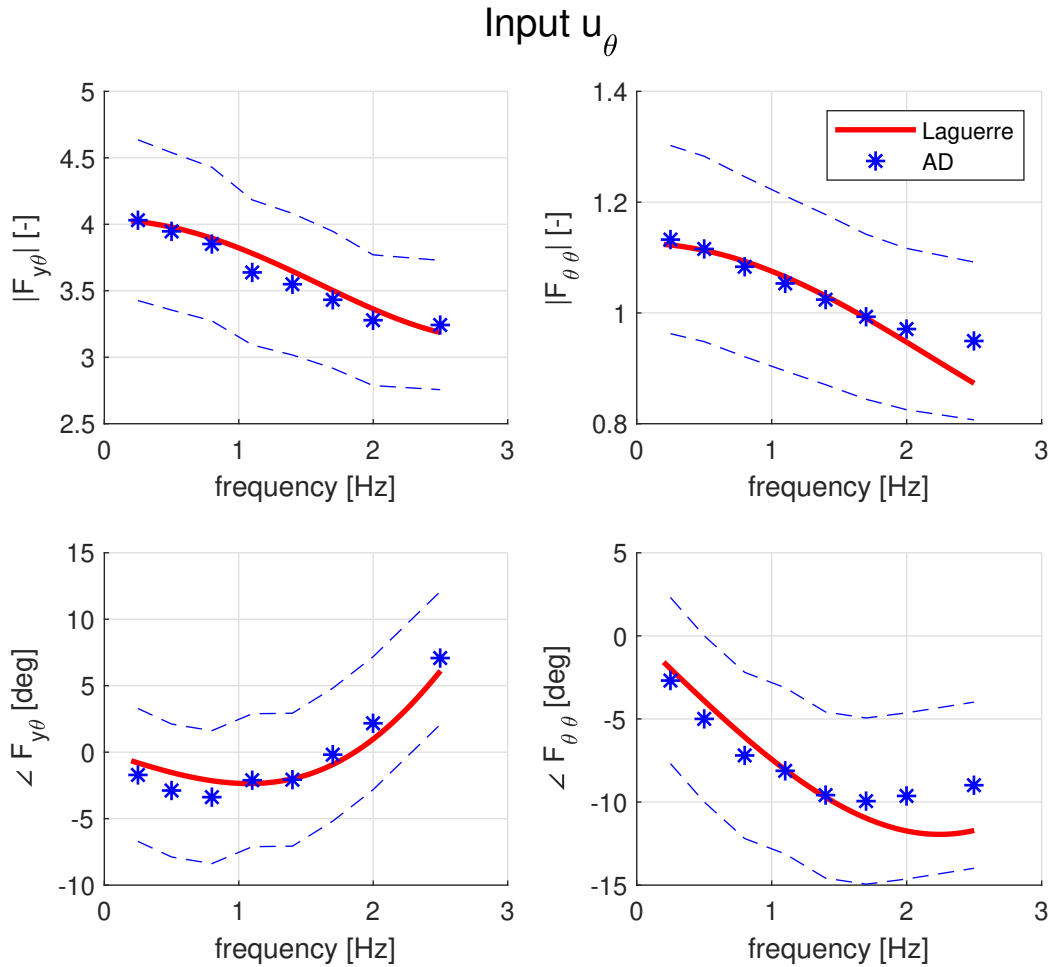Figure 3.22: Module and phase of the transfer functions linking the torsional motion to the lift and the torque. Dashed lines show intervals of $\pm 15\%$ for the module and $\pm 5 deg$ for the phase respect to the transfer function calculated with experimental aerodynamic derivatives.

For what concerns the aerodynamic forces deriving from a vertical motion in input (Figure 3.21) the module is quite well caught, however, it is slightly overestimated for the lift force at high frequency. Also the phase is well reconstructed for the vertical input motion on the lift force: it never exceeds a phase difference of more than 5 deg from the aerodynamic derivative model. For the torque model however the phase is badly reconstructed for frequencies greater than 1.4 Hz.

This issue in the identification of the transfer function which links the vertical motion to the torsional force will cause some uncertainty in the estimation of the bridge section aeroelastic behavior by the Laguerre expansion model, exposed in Chapter 4.

Regarding the forces caused by a torsional imposed motion, the module is inside the $\pm 15\%$ band for the whole tested frequency range. The phase is reconstructed better than with the other input motion and fits in the band of $\pm 5deg$ from the experimental data for the whole tested excitation frequencies. Also in this case however, for the model of the torque, the phase is slightly underestimated compared to the value of the aerodynamic derivative.

3.5.6.   Comparison with rational functions identification method

It is interesting to compare identification capabilities in time domain of the presented method with methods commonly used to represent wind action on bridge decks. As presented in Section 1.3, a rational function approximation is been frequently used in literature [13, 18], to interpolate experimental wind tunnel data.

In this section rational functions have been fitted to the experimental aerodynamic derivatives from wind tunnel tests. The curve fit is been done in two steps. First the coefficients are determined with a first guess set of lag coefficients d_n and linear least squares. Then non linear least squares is performed to find a better set of lag coefficients [14]. In the present work, only one lag coefficient d_1 is been considered. Therefore it can be seen from Equation (1.23a) that the rational function model has three unknown coefficients $(a_1^{nm}, a_2^{nm}, a_4^{nm})$ to be determined for each transfer function considered. Therefore, if three filters $(L = 3)$ for the Laguerre expansion model are considered, the computational burden of the two models is comparable. However, the rational functions model might perform better because of the presence of the two feed-through terms, a_1^{nm} and a_2^{nm}, which multiply the position and the velocity vector respectively, and are not present in the here presented Laguerre expansion model.

The result of the fitting on the ADs relative to lift and torque is shown in Figures 3.25-3.24. In the same figures, the rational functions fit is been compared with the approximation of the aerodynamic derivative given by the Laguerre model.

Then, using the fitted rational functions coefficients and the state-space model shown in Equation 1.29, the aerodynamic wind load is been represented.
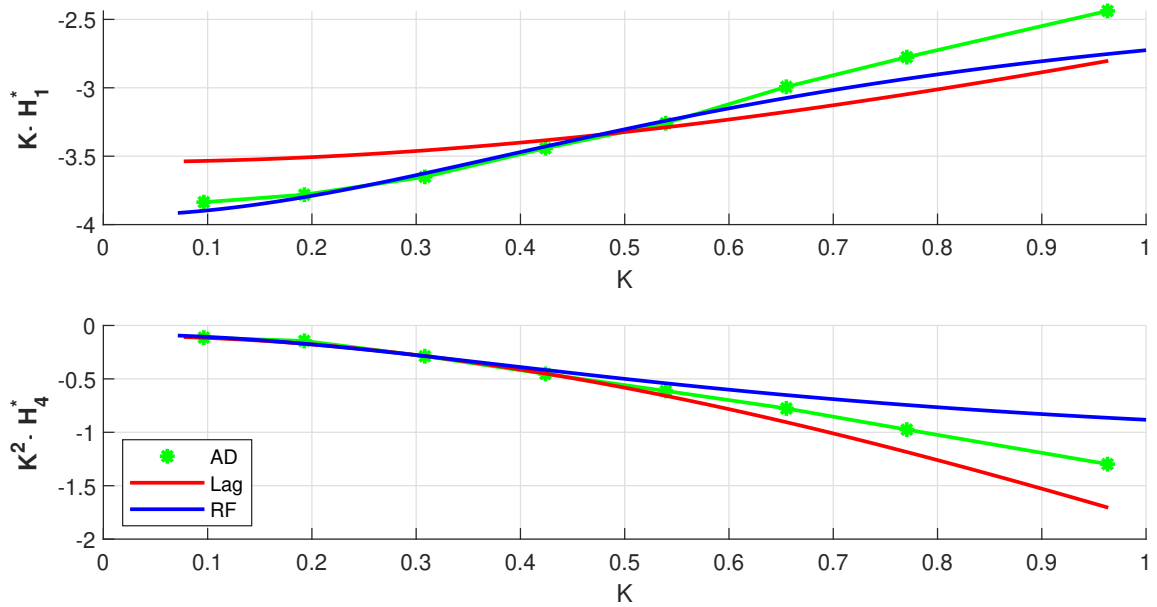
Figure 3.23: Aerodynamic derivatives in function of reduced frequency. Relative to lift because of vertical motion. Comparison between Rational Function fit and Laguerre model.
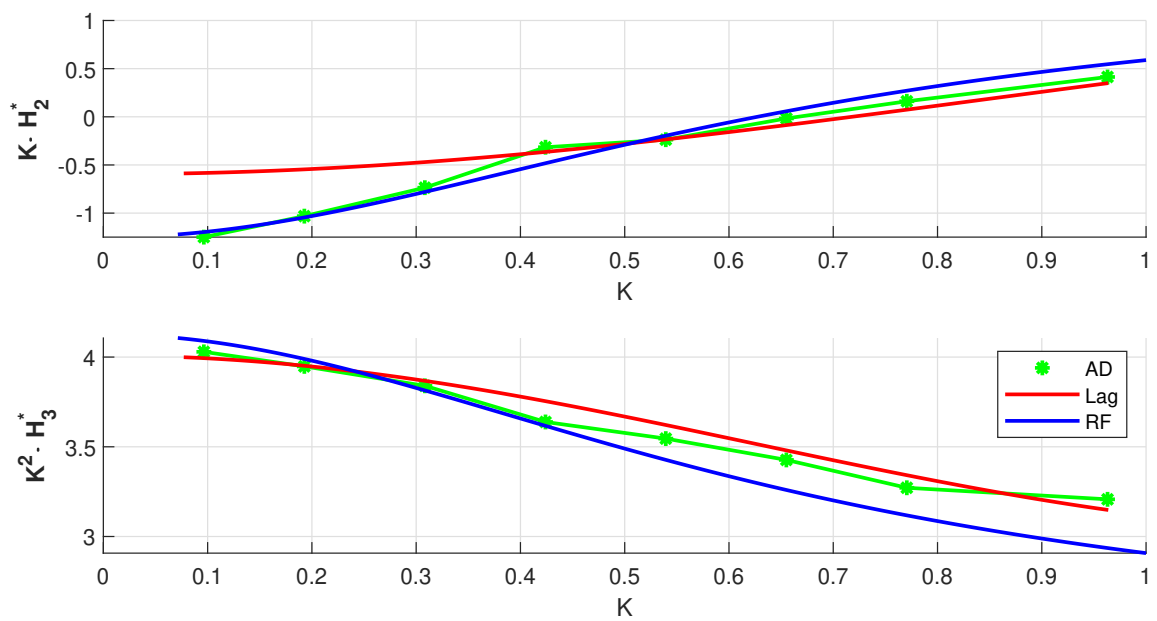

Figure 3.24: Aerodynamic derivatives in function of reduced frequency. Relative to lift because of torsional motion. Comparison between Rational Function fit and Laguerre model.
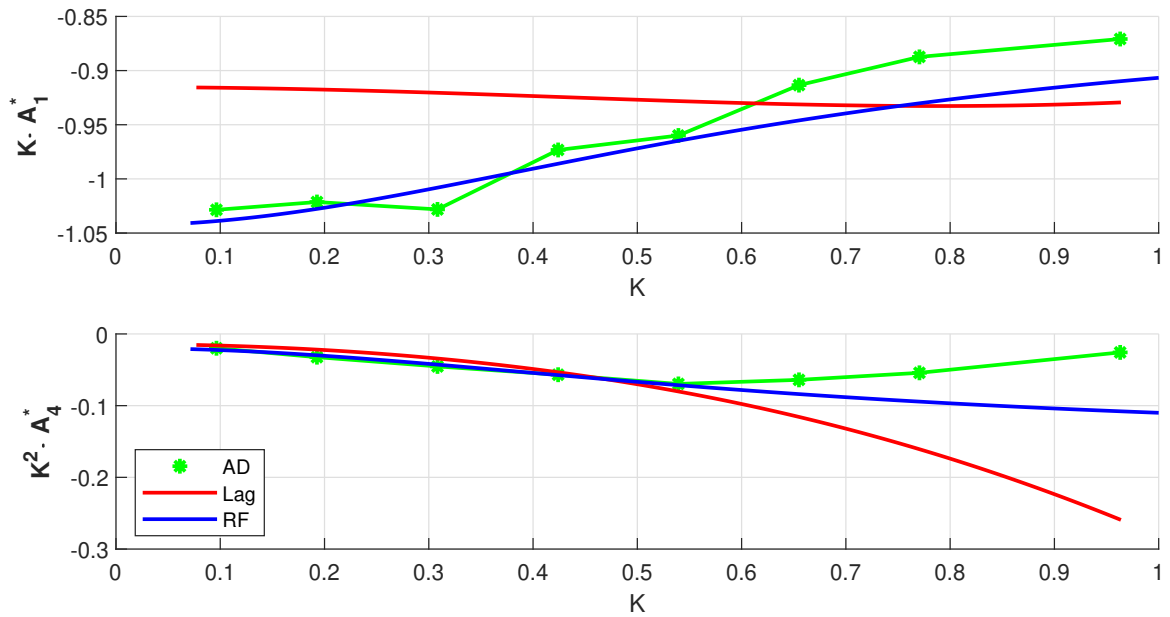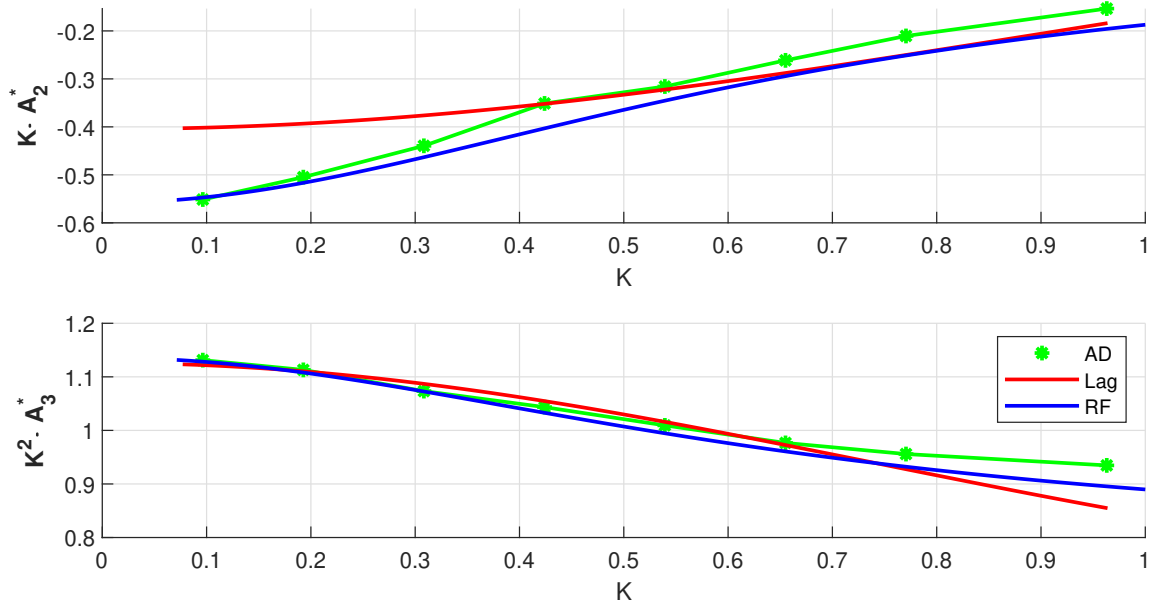
Figure 3.25: Aerodynamic derivatives in function of reduced frequency. Relative to torque because of vertical motion. Comparison between Rational Function fit and Laguerre model.

Figure 3.26: Aerodynamic derivatives in function of reduced frequency. Relative to torque because of torsional motion. Comparison between Rational Function fit and Laguerre model.

The comparison in frequency domain shows that both model perform well in the approximation of transfer functions related to lift action, as can be seen from Figures 3.23-3.24. Some discrepancies are shown in the aerodynamic derivatives relative to torque action because of vertical motion as can be seen from Figure 3.25 and as was already shown by the transfer functions in Figure 3.21.

In time domain instead, the aerodynamic forces approximation obtained with rational functions has been compared both with the data collected in the wind tunnel and the estimate obtained with the Laguerre expansion model. To evaluate numerically the similarities the phase metric (M_ϕ), the peak metric (M_p) and the magnitude warped metric (M_{mw}) were evaluated between the two models and the measured forces (refer to Subsection 3.5.1 for details about the comparison toolbox). The results are shown in Figures 3.27 and 3.28.
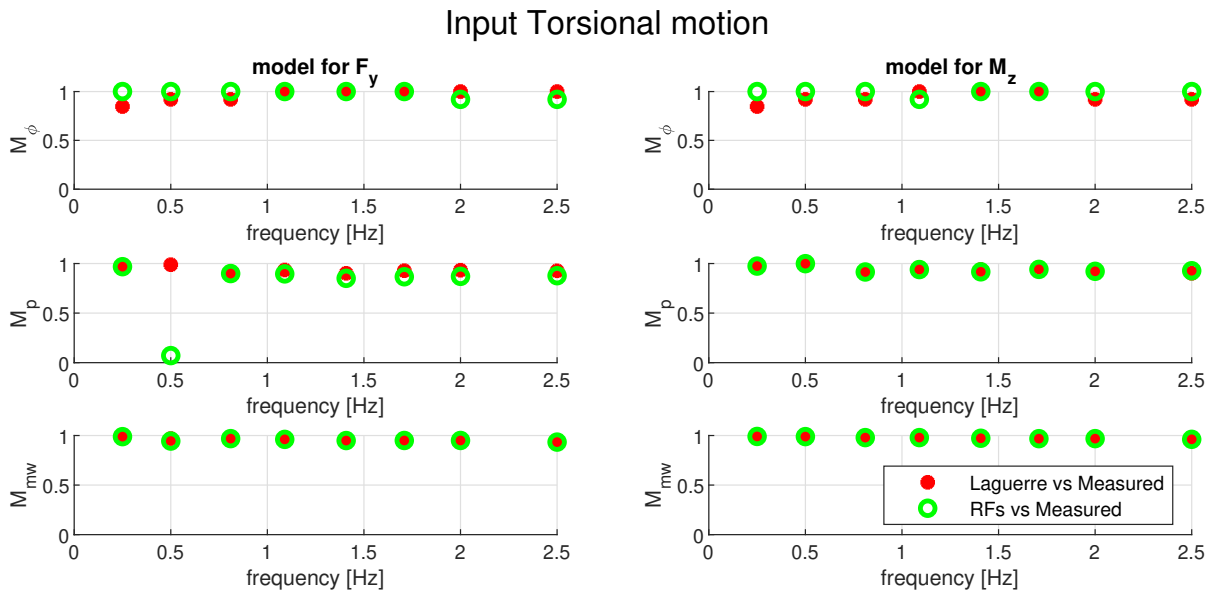

Figure 3.27: Assessment of model performance compared to rational function approximation. The graphs display values of goodness of fit metrics comparing rational function model and Laguerre filters model to measured forces. This is done in case of torsional input motion and for different excitation frequencies.
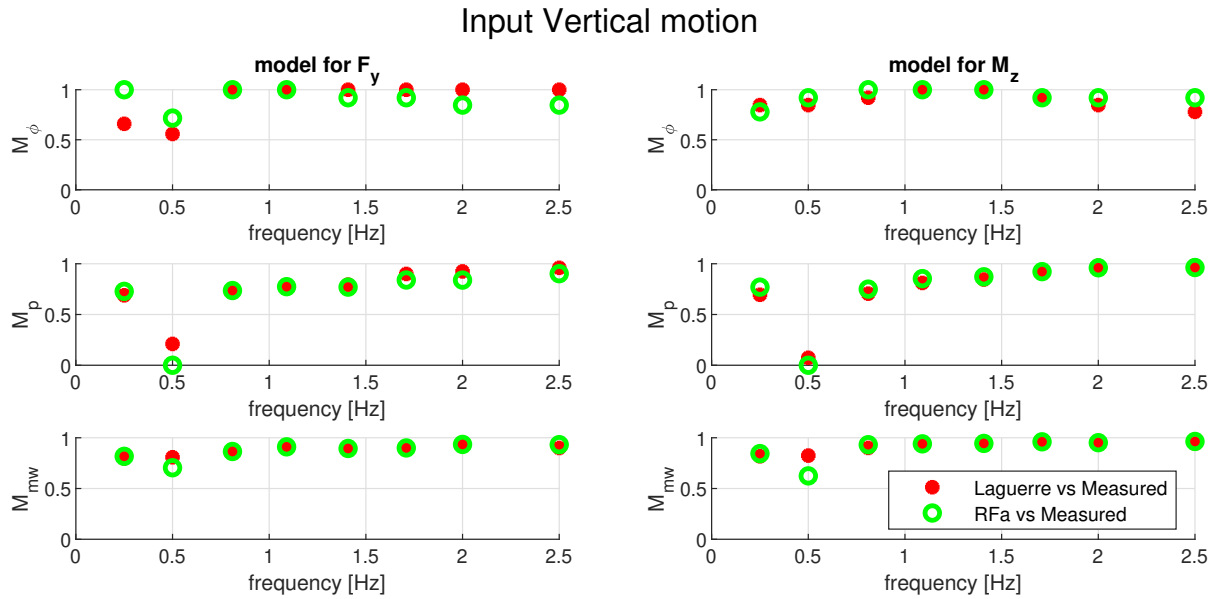
Figure 3.28: Assessment of model performance compared to rational function approximation. The graphs display values of goodness of fit metrics comparing rational function model and Laguerre filters model to measured forces. This is done in case of vertical input motion and for different excitation frequencies.

Overall the results show that both models have really similar capability to foresee the experimental results in time domain. In Figures 3.30-3.32 the same excitation frequencies of Subsection 3.5.2 are displayed to have a visual comparison of the two models in time domain.

For both the input motions at $0.5 Hz$ the rational functions approximation is able to guess slightly better the phase of the forces. However, both modelling methods give really similar results, that differs from the measured one because of the presence of the above-mentioned low frequency noise. Both model are evaluated with very low peak metric at this frequency only because of an error during the measurement campaign that causes a spike in the measured forces.

Also at 2.0 Hz the Laguerre model is proved to be as good as the rational functions model to foresee the wind action. According to the metrics, for the lift model, the Laguerre expansion method even outdoes the rational functions for what concerns the phase prediction. However, the difference is small and it is not clearly visible from the plotted time series.
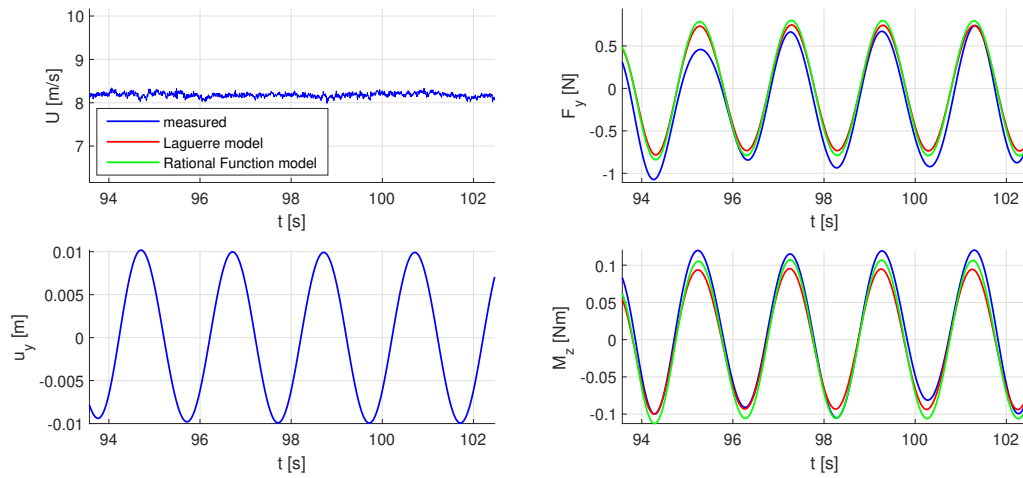
Figure 3.29: Particular of time histories. Input vertical motion. Excitation frequency 0.5 Hz. Section LN21-5200.Comparison between rational functions identification and Laguerre model identification.
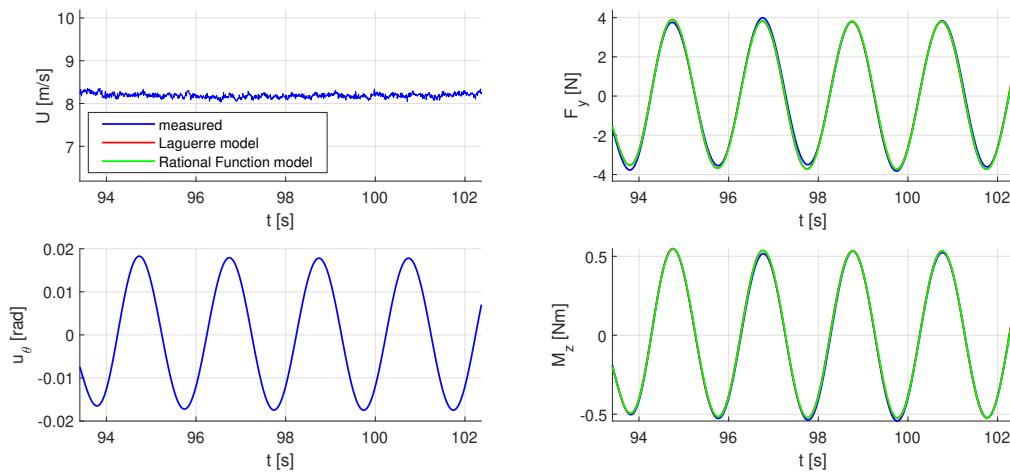

Figure 3.30: Particular of time histories. Input torsional motion. Excitation frequency 0.5Hz. Section LN21-5200. Comparison between rational functions identification and Laguerre model identification.
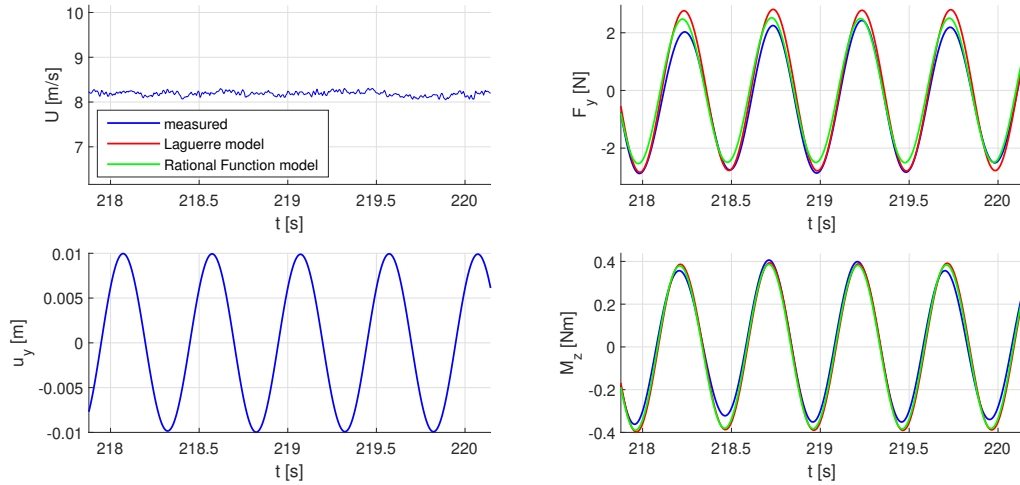
Figure 3.31: Particular of time histories. Input vertical motion at 2.0 Hz. Section LN21-5200. Comparison between rational functions and Laguerre model.
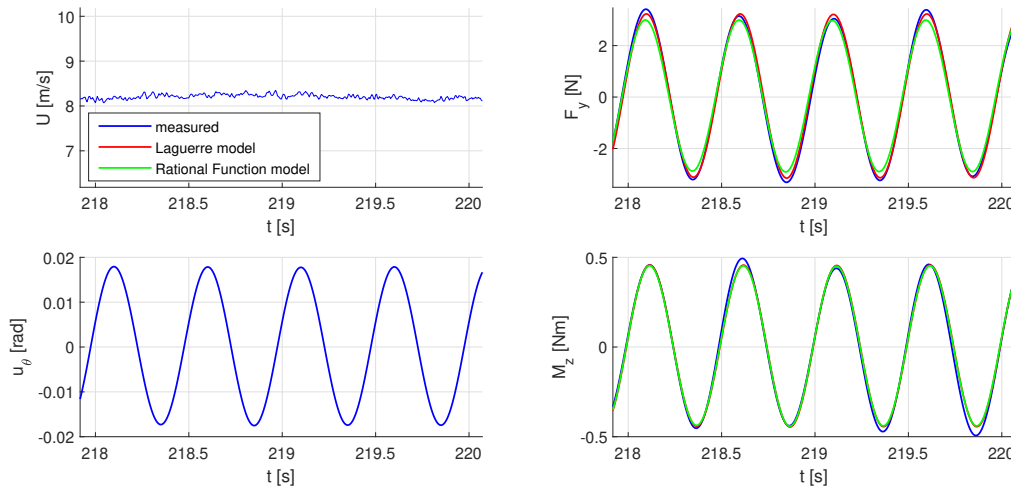

Figure 3.32: Particular of time histories. Input torsional motion at 2.0Hz. Section LN21-5200. Comparison between rational functions and Laguerre model.

It can be concluded that the presented model performs as good as the rational function model to represent the self-excited forces on a bridge deck in time domain. Furthermore this is done with only three unknown coefficients ($L = 3$) per transfer function to be determined, because only three Laguerre filters are considered. This allows the Laguerre model to have a comparable computational burden to the rational functions model, where three coefficients need to be determined for each transfer function as can be seen from Equation (1.23a).

4 | Laguerre Expansion Model to Estimate Bridge Aeroelastic Behaviour

In the previous sections it has been proved that the Laguerre expansion model is able to predict self-excited forces on a bridge deck with sufficient accuracy and low computational burden if compared with other identification methods commonly used in literature.

The defined model is here introduced in a two degrees of freedom dynamic model of bridge deck to test its capability to identify the girder dynamic behaviour.

Only vertical and torsional degrees of freedom are considered. This is because the most problematic kind of instability in long span bridges is two degrees of freedom flutter instability, which occurs because of the coupling of vertical and torsional motions.

A simplified scheme of the here considered two degrees of freedom model is shown in Figure 4.1. It is then checked if the Laguerre identification gives stability limits similar to other identification methods like rational functions.

To perform these checks a numerical simulation has been performed on a virtual model of girder section. To effectively run the numerical simulation a state space-model of the system has been developed.
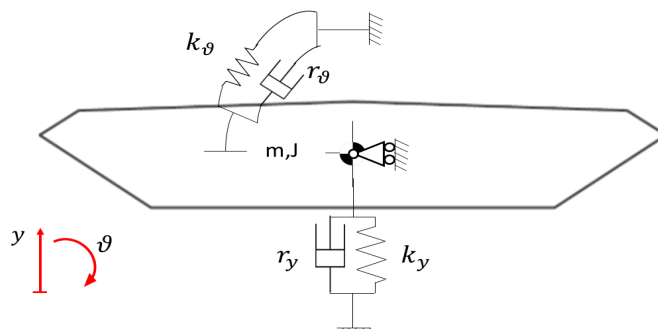

Figure 4.1: Two degrees of freedom elastically suspended deck section.

4.1. Laguerre State Space Model

As it has been shown for the rational functions method in Section 1.3, a state-space model can be defined also for the Laguerre expansion model. This is achieved writing in matrix form the recursive relation shown in Equation (2.33). This relation was used to construct the regression matrix $\boldsymbol{S}_v$ which represent the input motion convoluted with the Laguerre filters evaluated over the memory length. The obtained state-space model for self-excited forces prediction with Laguerre expansion model is shown in Equation (4.1).

$$\boldsymbol{S}_v(k+1) = \boldsymbol{A}_L \boldsymbol{S}_v(k) + \boldsymbol{B}_L v(k+1) \tag{4.1a}$$

$$\boldsymbol{F}_{nv}(k) = \boldsymbol{c}_{nv} \boldsymbol{S}_v(k) \tag{4.1b}$$

Where $\boldsymbol{v} \in [\boldsymbol{y}, \boldsymbol{x}, \boldsymbol{\theta}]$ is the input motion time history and $\boldsymbol{A}_L, \boldsymbol{B}_L$ are the Laguerre matrices constructed as shown in Equation (4.2). While $\boldsymbol{c}_{nv}$ are the identified filters coefficients relative to the transfer function between the input along $v \in [y, x, \theta]$ and the output along $n \in [y, x, \theta]$. Finally, $\boldsymbol{F}_{nv}$ is the corresponding aerodynamic force.

$$\boldsymbol{A}_L = \begin{bmatrix} \sqrt{\alpha} & 0 & 0 & \dots & 0 \\ \alpha - 1 & \sqrt{\alpha} & 0 & \dots & 0 \\ \sqrt{\alpha}(\alpha - 1) & \alpha - 1 & \sqrt{\alpha} & \dots & 0 \\ \vdots & & & \ddots & 0 \\ (\sqrt{\alpha})^{n-2}(\alpha - 1) & & & & \sqrt{\alpha} \end{bmatrix}, \quad \boldsymbol{B}_L = \sqrt{1-\alpha} \begin{bmatrix} 1 \\ \sqrt{\alpha} \\ (\sqrt{\alpha})^2 \\ \vdots \\ (\sqrt{\alpha})^{n-1} \end{bmatrix} \tag{4.2}$$

With the system in Equation (4.1), given an input motion time history and a set of L coefficients relative to the transfer function between that motion and an aerodynamic action between lift, drag or torque, the specific force time history can be modelled.

4.2. 2 Dof Girder Section Laguerre Model

The aerodynamic action calculated with the state space Laguerre model has to be introduced in a two degrees of freedom dynamic model to calculate the dynamic response of the system in an in-wind condition. The equations of motion of the section in Figure 4.1 are shown in Equation (4.3). The equation can be rewritten in a compact form calling the mass matrix $\boldsymbol{M}$, the damping matrix $\boldsymbol{R}$ and the stiffness matrix $\boldsymbol{K}$ and the state is defined as $\boldsymbol{X} = [y(t), \theta(t), \dot{y}(t), \dot{\theta}(t)]^T$. This compact form is then reformulated in the

state space form in Equation (4.4).

$$
\begin{bmatrix} m_y & 0 \\ 0 & J \end{bmatrix} \begin{bmatrix} \ddot{y}(t) \\ \ddot{\theta}(t) \end{bmatrix} + \begin{bmatrix} r_y & 0 \\ 0 & r_\theta \end{bmatrix} \begin{bmatrix} \dot{y}(t) \\ \dot{\theta}(t) \end{bmatrix} + \begin{bmatrix} k_y & 0 \\ 0 & k_\theta \end{bmatrix} \begin{bmatrix} y(t) \\ \theta(t) \end{bmatrix} = \begin{bmatrix} F_y(t) \\ F_\theta(t) \end{bmatrix} = \boldsymbol{F}(t) \tag{4.3}
$$

$$
\begin{aligned}
\dot{\boldsymbol{X}}(t) &= \begin{bmatrix} \boldsymbol{0} & \boldsymbol{I} \\ -\boldsymbol{M}^{-1}\boldsymbol{K} & -\boldsymbol{M}^{-1}\boldsymbol{R} \end{bmatrix} \boldsymbol{X}(t) + \begin{bmatrix} \boldsymbol{0} \\ \boldsymbol{M}^{-1} \end{bmatrix} \boldsymbol{F}(t) \\
&= \boldsymbol{A}_c \boldsymbol{X}(t) + \boldsymbol{B}_c \boldsymbol{F}(t)
\end{aligned} \tag{4.4}
$$

$$
\boldsymbol{A} = e^{\boldsymbol{A}_c \Delta t}, \ \boldsymbol{B} = [\boldsymbol{A} - \boldsymbol{I}]\boldsymbol{A}_c^{-1}\boldsymbol{B}_c \tag{4.5}
$$

Since the model presented in this work is a discrete model, the continuous time matrices $\boldsymbol{A}_c$ and $\boldsymbol{B}_c$, are discretised to the discrete time matrices $\boldsymbol{A}$ and $\boldsymbol{B}$ with time step $\Delta t = \Delta s \frac{B}{V}$, where Δs is the adimensional time step used in the training, B is the width of the model and V is the wind speed. The time discretisation of the matrices is done as it is shown in Equation (4.5).

The discrete Laguerre model to represent the aerodynamic forces $\boldsymbol{F}$ is shown in Equation (4.7) and it is obtained augmenting the model in Equation (4.1b). It is then inserted in the equations of motion.

$$
\hat{\boldsymbol{A}}_L = \begin{bmatrix} \boldsymbol{A}_L & & & \\ & \boldsymbol{A}_L & & \\ & & \boldsymbol{A}_L & \\ & & & \boldsymbol{A}_L \end{bmatrix}, \hat{\boldsymbol{B}}_L = \begin{bmatrix} \boldsymbol{B}_L & \boldsymbol{0} \\ \boldsymbol{0} & \boldsymbol{B}_L \\ \boldsymbol{B}_L & \boldsymbol{0} \\ \boldsymbol{0} & \boldsymbol{B}_L \end{bmatrix} \tag{4.6}
$$

Also the regression matrix Equation (4.1a) needs to be augmented and inserted in the system. This is done expanding the Laguerre matrices as shown in Equation (4.6) and then obtaining Equation (4.8b).

$$
\boldsymbol{F}(k) = \begin{bmatrix} c_{yy} & c_{y\theta} & \boldsymbol{0} & \boldsymbol{0} \\ \boldsymbol{0} & \boldsymbol{0} & c_{\theta y} & c_{\theta\theta} \end{bmatrix} \begin{bmatrix} \boldsymbol{S}_y(k) \\ \boldsymbol{S}_\theta(k) \\ \boldsymbol{S}_y(k) \\ \boldsymbol{S}_\theta(k) \end{bmatrix} = \boldsymbol{C}\hat{\boldsymbol{S}}(k) \tag{4.7}
$$

$$
\boldsymbol{X}(k+1) = \boldsymbol{A}\boldsymbol{X}(k) + \boldsymbol{B}\boldsymbol{C}\hat{\boldsymbol{S}}(k) \tag{4.8a}
$$

$$
\hat{\boldsymbol{S}}(k+1) = \hat{\boldsymbol{A}}_L\hat{\boldsymbol{S}}(k) + \begin{bmatrix} \hat{\boldsymbol{B}}_L & \boldsymbol{0} \end{bmatrix} \boldsymbol{X}(k+1) \tag{4.8b}
$$

Finally, the system in Equation (4.8) is rearranged to a correct discrete time state space formulation shown in Equation (4.9). With the latter formulation the system response to

a certain wind speed can be calculated and also the poles of the system, to assess stability, can be easily calculated.

$$\begin{bmatrix} \boldsymbol{X}(k+1) \\ \hat{\boldsymbol{S}}(k+1) \end{bmatrix} = \begin{bmatrix} \boldsymbol{A} & \boldsymbol{BC} \\ \begin{bmatrix} \hat{\boldsymbol{B}}_L & \boldsymbol{0} \end{bmatrix} \boldsymbol{A} & \hat{\boldsymbol{A}}_L + \begin{bmatrix} \hat{\boldsymbol{B}}_L & \boldsymbol{0} \end{bmatrix} \boldsymbol{BC} \end{bmatrix} \begin{bmatrix} \boldsymbol{X}(k) \\ \hat{\boldsymbol{S}}(k) \end{bmatrix} \tag{4.9}$$

The system in Equation (4.1) calculates self-excited forces for the specific wind speed used in the training to identify the coefficients $\boldsymbol{c}_{nv}$. In the present work, to identify a model independent from the wind speed, the training has been carried out with adimensional data. The dimensions are then given back at the end according to the specific wind speed (see flow-chart Figure 3.8). Therefore the state-space model used in the Matlab code written for this work is slightly different from the one shown in Equation (4.9). For further details see Appendix B.

Width	0.50 m	f_v	$2 Hz$
Length	2.68 m	f_t	$5 Hz$
m	15 Kg/m	ρ_{air}	1.19 Kg/m^3
J	0.6 Kgm^2/m	ξ	3 ‰
$V \in [17, 18, 19, ..., 40]$ m/s			

Table 4.1: Simulation data for 2 Dof aeroelastic model.

4.3.   Critical Flutter Velocity Identification

As explained in Section 1.4 one of the most critical issues for long span bridges is represented by flutter instability. This kind of instability occurs when, with the increase of the wind speed, the first torsional frequency of vibration decreases and gets nearer to the vertical one. This causes the real part of the eigenvalues to became positive and hence gives rise to instability [16]. The wind speed at which the instability occurs is called flutter critical velocity.

In this work a numerical simulation on an example of bridge section, with data shown in Table 4.1, has been performed to test the capability of the Laguerre expansion model to foresee flutter critical speed. To have a comparison, the same dynamical simulation has been performed with rational functions model using the state-space model in Equation (1.34). The system response has been evaluated for different values of wind speed, until unstable behaviour has been observed. The transition to unstable behaviour can be seen from the time histories in Figure 4.2. At each calculation step the eigenvalues of

the problem have been calculated. Since the here presented model is been developed in discrete time domain, the calculated poles are discrete-time poles. For clarity the system eigenvalues corresponding to the first torsional and vertical modes have been converted back to continuous time domain an plotted in Figure 4.3, for wind speeds range shown in Table 4.1.
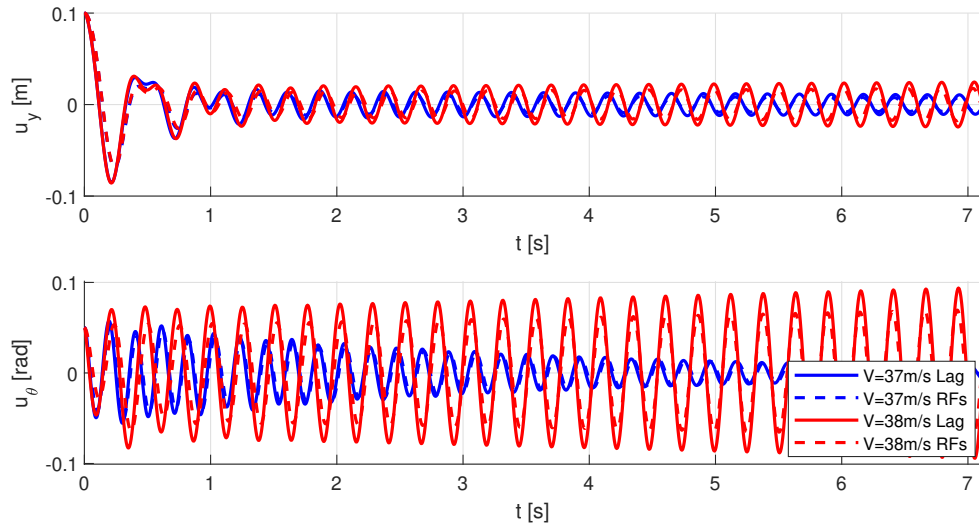

Figure 4.2: The coupled dynamic model has been simulated for different speeds until instability was observed. Flutter speed $V = 37.6 m/s$.
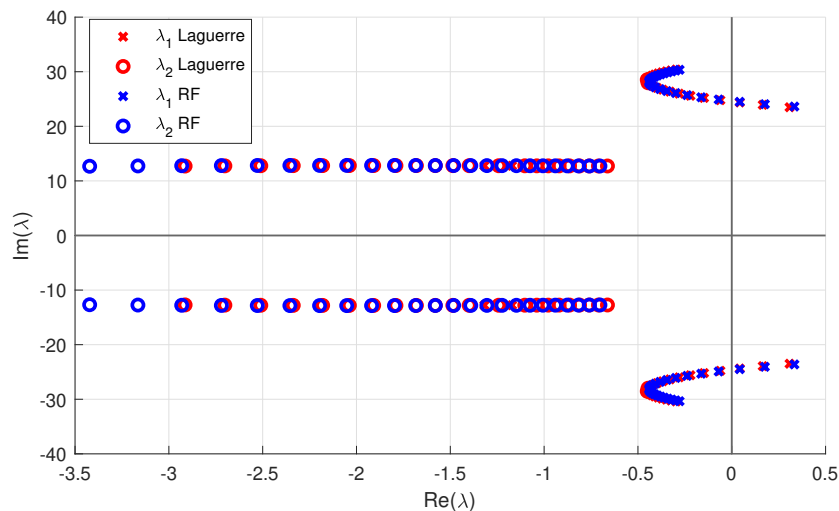
Figure 4.3: Continuous time 2 Dof system eigenvalues corresponding to first vertical and torsional vibration modes. Moving towards the right-half complex plane as wind speed increases $V \in [30, 31, ...40] m/s$. Calculated with Laguerre expansion model and Rational Functions model. Instability reached at 37.6 m/s.

As the wind speed increases the poles of the system move towards the unstable region: when they gain positive real part the system becomes unstable. From the simulation results it is proved that the presented Laguerre model is able to foresee the system's dynamic behaviour as good as the rational function model.
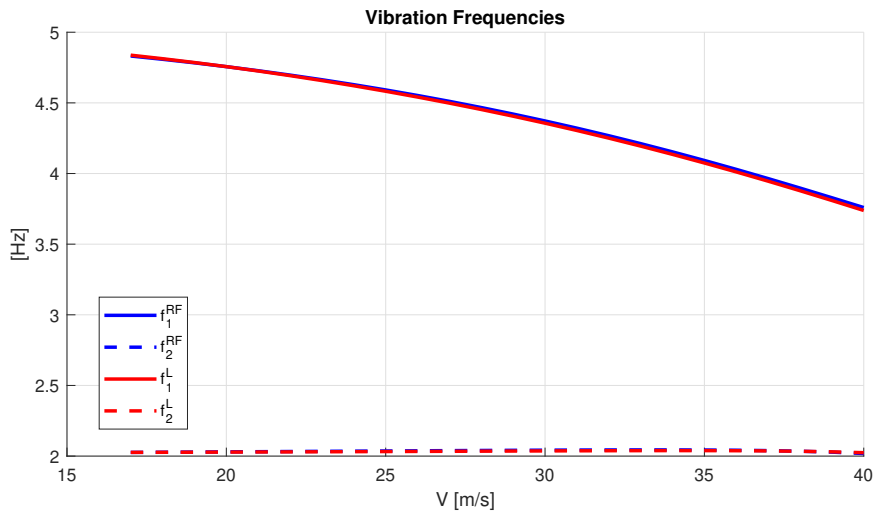
Figure 4.4: 2 Dof system first vertical and torsional vibration frequencies in function of wind speed. Comparison between Laguerre and Rational Functions models.
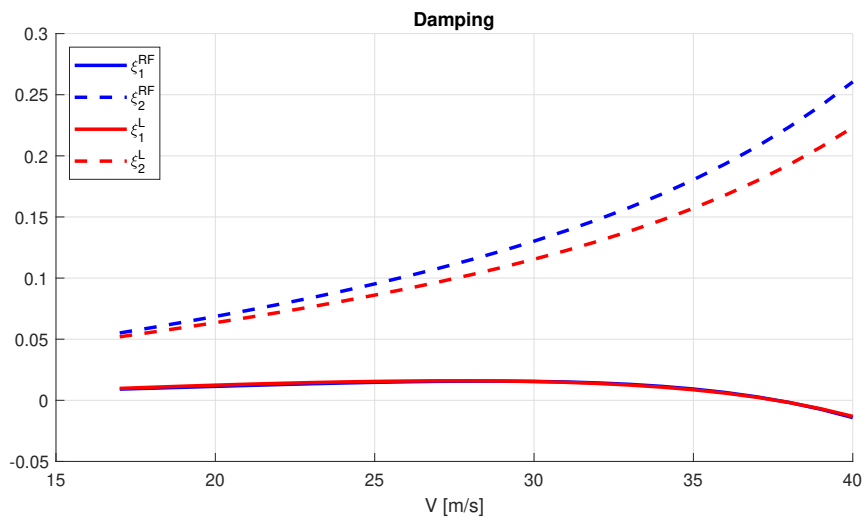

Figure 4.5: 2 Dof system vertical and torsional damping coefficient as function of wind speed. Comparison between Laguerre and Rational Functions models.

From Figure 4.4 it can be seen that as the wind speed increases the first torsional vibration frequency gets nearer to the vertical one and risks to cause flutter instability. Finally, the simulation results in Figure 4.5 show how both models foresee the torsional damping

coefficient to decrease and become negative as the wind speed increases. Instability is reached when the torsional damping is not anymore able to dissipate energy, this happens for both models around $V = 37.6 m/s$. The Laguerre model is therefore proved to be able to correctly depict the aeroelastic behaviour of a two degrees of freedom deck section.

5 | Conclusions and Future Developments

The aim of the present work was to develop an effective linear model for suspended bridge aerodynamic identification. The elaborated model proved to be effective for force identification and system dynamics modelling. The aerodynamic forces were approximated using a linear combination of orthonormal functions with particular properties.

This work started as a derivation of the innovative work by Skyvulstad et al. [20] who used a Volterra series model with parameterized kernels expanded with Laguerre basis functions to approximate non linear drag force. Laguerre filters proved to be a well behaved basis for least squares identification. Moreover, they have low-pass filter properties and an inbuilt exponential decay, ideal to approximate mechanical systems' impulse response functions.

In the present work, a linear Laguerre expansion model has been developed and a training procedure has been established. First, it has been tested on a simple first order system, showing good approximation capabilities and the possibility to optimize the calibration of the parameters. Then the training procedure has been performed on state-of-the-art wind tunnel data, collected in the wind tunnel of the Norwegian University of Science and Technology (NTNU) in Trondheim. The identified Laguerre model has been used to foresee the self-excited forces in time domain and they have been compared with the measured data with the help of a time domain comparison toolbox by Kavrakov et al.[7]. The toolbox has been also used for a trial and error procedure for the calibration of the model.

Once optimal parameter values have been found, the Laguerre model showed good modelling performance in time domain. The goodness of the approximation has also been tested in frequency domain showing small discrepancy from the experimental data.

The model performance has also been proved to be independent of small variations in the geometry of the deck section tested.

The here identified model has been then compared to a well established bridge aerodynamic model: the rational functions model. The two models have been compared both

in time domain and in frequency domain and the Laguerre model proved to be able to foresee wind induced forces on deck sections in time domain as good as rational functions model. In frequency domain, some discrepancies have been observed for $A1^*$ and $A4^*$ aerodynamic derivatives approximation. Moreover, the Laguerre model has also a comparable computational burden in the training phase compared to the rational functions. Finally, the identified model for wind induced lift and torque has been introduced in a complete two degrees of freedom dynamic section model. A time series simulation has been carried out for increasing wind speeds until unstable behaviour has been observed. The model proved to be able to correctly model the dynamic of the section and to determine the stability limits of the girder. The flutter critical speed calculated with the Laguerre model coincides with the result found with rational function model.

The presented Laguerre model gave interesting results with low computational burden and has room for further improvement. Possible future development is to improve the impulse response approximation including two feed-through terms relative to speed and displacement. The absence of these two terms is one of the main causes of the difference in performances between the rational functions model and the Laguerre expansion model. Furthermore, in the presented work the same value of the two parameters of the model has been used for the approximation of all the identified transfer functions between the forces and the deck degrees of freedom. The training of the model could be improved by considering calibrating a different set of parameters for the identification of each transfer function. This might solve the differences in performance observed between the approximation of the different aerodynamic derivatives.

A further alternative which is worth testing would be to reformulate the model starting from a continuous time formulation of Laguerre filters instead of a discrete one. Finally, it would be interesting to investigate the eventual differences in performances of the model using white noise as training data instead of a single harmonic motion.

Bibliography

[1] J. P. Bergerud and H. M. Torød. Shape optimization of an aluminium girder for a long-span suspension bridge. Master's thesis, NTNU, 2021.

[2] B. Cao and P. P. Sarkar. Identification of Rational Functions using two-degree-of-freedom model by forced vibration method. *Engineering Structures*, 43:21–30, oct 2012. ISSN 01410296. doi: 10.1016/J.ENGSTRUCT.2012.05.003.

[3] G. Diana, M. Falco, S. Bruni, A. Cigada, G. L. Larose, A. Darnsgaard, and A. Collina. Comparisons between wind tunnel tests on a full aeroelastic model of the proposed bridge over Stretto di Messina and numerical results. *Journal of Wind Engineering and Industrial Aerodynamics*, 54-55(C):101–113, 1995. ISSN 01676105. doi: 10.1016/0167-6105(94)00034-B.

[4] G. Diana, F. Resta, A. Zasso, M. Belloli, and D. Rocchi. Forced motion and free motion aeroelastic tests on a new concept dynamometric section model of the Messina suspension bridge. *Journal of Wind Engineering and Industrial Aerodynamics*, 92(6): 441–462, may 2004. ISSN 01676105. doi: 10.1016/J.JWEIA.2004.01.005.

[5] E. Ekern and D. Bang. Aerodynamic Stability of a Suspension Bridge with an Aluminum Girder-Wind Tunnel Testing and Numerical Predictions. Master's thesis, Norwegian University of Science and Technology, 2020.

[6] W. H. Kautz. Transient Synthesis in the Time Domain. *Transactions of the IRE Professional Group on Circuit Theory*, 1(3):29–39, 1952. ISSN 01976389. doi: 10.1109/TCT.1954.1083588.

[7] I. Kavrakov, A. Kareem, and G. Morgenthal. Comparison Metrics for Time-Histories: Application to Bridge Aerodynamics. *Journal of Engineering Mechanics*, 146(9): 04020093, 2020. ISSN 0733-9399. doi: 10.1061/(asce)em.1943-7889.0001811.

[8] Y. W. Lee. Statistical Theory of Communication. In L. John Wiley & Sons, editor, *Statistical Theory of Communication*, chapter 18-19, pages 459–501. John Wiley & Sons, Ltd, New York, 1960. doi: 10.2307/2282273.

[9] V. Z. Marmarelis. Identification of Nonlinear Biological Systems Using Laguerre Expansions of Kernels. *Annals of Biomedical Engineering*, 21:573–589, 1993.

[10] Norconsult AS. E39 Stord - Tysnes: Bru over Langenuen og Søreidsvika, Skissepros. Technical report, Norconsult AS, 2015. URL `https://www.norconsult.no/`.

[11] Norwegian Pubblic Roads Administration. The E39 Coastal Highway Route | Statens vegvesen, 2022. URL `https://www.vegvesen.no/en/road-projects/european-road/e39coastalhighwayroute/`.

[12] H. Ogura. Estimation of Wiener kernels of a nonlinear system and a fast algorithm using digital Laguerre filters. In *25th NIBB Conference*, pages 14–62, 1986.

[13] O. Øiseth, A. Rönnquist, and R. Sigbjörnsson. Time domain modeling of self-excited aerodynamic forces for cable-supported bridges: A comparative study. *Computers and Structures*, 89(13-14):1306–1322, 2011. ISSN 00457949. doi: 10.1016/j.compstruc.2011.03.017.

[14] O. Øiseth, A. Rönnquist, and R. Sigbjörnsson. Finite element formulation of the self-excited forces for time-domain assessment of wind-induced dynamic response and flutter stability limit of cable-supported bridges. *Finite Elements in Analysis and Design*, 50:173–183, 2012. ISSN 0168874X. doi: 10.1016/j.finel.2011.09.008.

[15] O. Olsen. Report Langenuen Suspension Bridge - Aluminium Bridge Girder Alternative. Technical report, Norwegian Public Roads Administration, 2020.

[16] D. Rocchi. Lecture notes in Wind Engineering. 2020.

[17] R. Scanlan and J. Tomko. Airfoil and bridge deck flutter derivatives. *J. Eng. Mech.*, 97:1717–37, 1971. URL `https://www.scopus.com/record/display.uri?eid=2-s2.0-2242449120{&}origin=inward`.

[18] B. Siedziako and O. Øiseth. An enhanced identification procedure to determine the rational functions and aerodynamic derivatives of bridge decks. *Journal of Wind Engineering and Industrial Aerodynamics*, 176(November 2017):131–142, 2018. ISSN 01676105. doi: 10.1016/j.jweia.2018.03.025.

[19] B. Siedziako, O. Øiseth, and A. Rønnquist. An enhanced forced vibration rig for wind tunnel testing of bridge deck section models in arbitrary motion. *Journal of Wind Engineering and Industrial Aerodynamics*, 164 (December 2016):152–163, 2017. ISSN 01676105. doi: 10.1016/j.jweia.2017.02.011. URL `http://dx.doi.org/10.1016/j.jweia.2017.02.011https://sci-hub.yncjkj.com/10.1016/j.jweia.2017.02.011`.

[20] H. Skyvulstad, Ø. W. Petersen, T. Argentini, A. Zasso, and O. Øiseth. The use of a Laguerrian expansion basis as Volterra kernels for the efficient modeling of nonlinear self-excited forces on bridge decks. *Journal of Wind Engineering and Industrial Aerodynamics*, 219(February), 2021. ISSN 01676105. doi: 10.1016/j.jweia.2021.104805.

[21] J. H. Son and Y. Kim. Parametric Estimation of Volterra Kernel for the Dynamic Response of an Offshore Structure Using Laguerre Polynomials. *Journal of Offshore Mechanics and Arctic Engineering*, 142(6):1–13, 2020. ISSN 1528896X. doi: 10.1115/1.4046675.

[22] J. H. Son and Y. Kim. Probabilistic time series prediction of ship structural response using Volterra series. *Marine Structures*, 76(November 2020):102928, 2021. ISSN 09518339. doi: 10.1016/j.marstruc.2020.102928. URL `https://doi.org/10.1016/j.marstruc.2020.102928`.

[23] The Mathworks Inc. MATLAB, 2021.

[24] T. Theodorsen. General theory of aerodynamic instability and the mechanism of flutter. Technical report, NACA report no. 496, Washington DC, 1934.

[25] V. Volterra and E. T. Whittaker. *Theory of functionals and of integral and integro-differential equations*. Dover publications, 1959.

A | Linearisation of QST

To linearise different terms of the force components in Equations 1.6, 1.7 around x_0, y_0, θ_0. Some assumptions can be done. The mean wind velocity can be assumed larger than the turbulence components: $V_m >> w$, $V_m >> v$. Also the horizontal velocity of the structure can be considered smaller than the mean wind speed $V_m >> \dot{x}$. Finally, the angle of attack of the relative wind speed is usually sufficiently small that $tan(\psi) \simeq \psi$. With these assumptions the relations in Equation A.1 are obtained:

$$
\begin{aligned}
\psi &= \frac{w - \dot{\bar{y}} - B_{1i}\dot{\bar{\theta}}}{V_m} \\
\bar{\alpha} &= \alpha - \alpha_0 \\
V_{Rel}^2 &= V_m^2 + 2V_m v - 2V_m \dot{x} \\
\alpha &= \theta + \psi = \bar{\theta} + \theta_0 + \frac{w - \dot{\bar{y}} - B_{1i}\dot{\bar{\theta}}}{V_m} \\
C_D(\alpha) &= C_{D0} + \left.\frac{\partial C_D}{\partial \alpha}\right|_0 \alpha = C_{D0} + C_D'\alpha \\
C_L(\alpha) &= C_{L0} + \left.\frac{\partial C_L}{\partial \alpha}\right|_0 \alpha = C_{L0} + C_L'\alpha \\
C_M(\alpha) &= C_{M0} + \left.\frac{\partial C_M}{\partial \alpha}\right|_0 \alpha = C_{M0} + C_M'\alpha
\end{aligned}
\tag{A.1}
$$

Where C_{D0}, C_{L0}, C_{M0} are the values of C_D, C_L, C_M in $\alpha = \alpha_0$. With the assumption of small angle of attack it can be also assumed that $sin(\psi) = \psi$ and $cos(\psi) = 1$. Then, the expression of the self-excited forces from Equation 1.5 can be rewritten in a vector from:

$$
\begin{bmatrix} F_x \\ F_y \\ F_\theta \end{bmatrix} = \begin{bmatrix} F_D(\alpha) - \psi F_L(\alpha) \\ \psi F_D(\alpha) - F_L(\alpha) \\ M(\alpha) \end{bmatrix} = \begin{bmatrix} F_D \\ F_L \\ M \end{bmatrix} + \psi \begin{bmatrix} -F_L \\ F_D \\ 0 \end{bmatrix}
$$

Substituting the linearised expression of F_D, F_L and M it can be obtained:

$$\begin{bmatrix} F_x \\ F_y \\ F_\theta \end{bmatrix} = \frac{1}{2}\rho B L V_{Rel}^2 \left(\begin{bmatrix} C_{D0} \\ C_{L0} \\ BC_{M0} \end{bmatrix} + \alpha \begin{bmatrix} C_D' \\ C_L' \\ BC_M' \end{bmatrix} + \psi \begin{bmatrix} -C_{L0} \\ C_{D0} \\ 0 \end{bmatrix} + \psi\alpha \begin{bmatrix} -C_L' \\ C_D' \\ 0 \end{bmatrix} \right) \quad (A.2)$$

The product $\psi\alpha$ is very small compared to the other terms, it can thus be neglected. Substituting the linearised expression of V_{Rel}, α and ψ, Equation A.2 becomes:

$$\begin{aligned} \begin{bmatrix} F_x \\ F_y \\ F_\theta \end{bmatrix} = \frac{1}{2}\rho B L (V_m^2 + 2V_m v - 2V_m\dot{x}) &\left(\begin{bmatrix} C_{D0} \\ C_{L0} \\ BC_{M0} \end{bmatrix} \right. \\ &+ \begin{bmatrix} (\bar{\theta} + \frac{w-\dot{y}-B_{1x}\dot{\theta}}{V_m})C_D' \\ (\bar{\theta} + \frac{w-\dot{y}-B_{1y}\dot{\theta}}{V_m})C_L' \\ (\bar{\theta} + \frac{w-\dot{y}-B_{1\theta}\dot{\theta}}{V_m})BC_M' \end{bmatrix} + \frac{1}{V_m} \left. \begin{bmatrix} -(w-\dot{y}-B_{1x}\dot{\theta})C_{L0} \\ (w-\dot{y}-B_{1y}\dot{\theta})C_{D0} \\ 0 \end{bmatrix} \right) \end{aligned} \quad (A.3)$$

Therefore, the linearised expression of the quasi-steady forces is rewritten in matrix form as in Equation (A.4).

$$\boldsymbol{F}_{QST} = \boldsymbol{F}_{QST}^{st} + \boldsymbol{R}_{ae}\dot{\bar{\boldsymbol{X}}} + \boldsymbol{K}_{ae}\bar{\boldsymbol{X}} + \boldsymbol{A}_m\boldsymbol{b} \quad (A.4)$$

Here the state vector $\bar{\boldsymbol{X}} = [\bar{x}, \bar{y}, \bar{\theta}]^T$ is defined. The matrices $\boldsymbol{R}_{ae}$, $\boldsymbol{K}_{ae}$ and $\boldsymbol{A}_m$ are respectively the damping, stiffness and admittance matrices shown in Equation (A.5).

$$\boldsymbol{F}_{QST}^{st} = \frac{1}{2}\rho B L V_m^2 \begin{bmatrix} C_{D0} \\ C_{L0} \\ BC_{M0} \end{bmatrix} \quad (A.5a)$$

$$\boldsymbol{R}_{ae} = -\frac{1}{2}B L V_m \begin{bmatrix} 2C_{D0} & C_D' - C_{L0} & B_{1x}(C_D' - C_{L0}) \\ 2C_{L0} & C_L' - C_{D0} & B_{1y}(C_L' - C_{D0}) \\ 2C_{M0}B & BC_M' & B_{1\theta}BC_M' \end{bmatrix} \quad (A.5b)$$

$$\boldsymbol{K}_{ae} = \frac{1}{2}\rho B L V_m^2 \begin{bmatrix} 0 & 0 & C_D' \\ 0 & 0 & C_L' \\ 0 & 0 & BC_M' \end{bmatrix} \quad (A.5c)$$

$$\boldsymbol{A}_m = \frac{1}{2}\rho B L V_m \begin{bmatrix} 2C_{D0} & C_D' - C_{L0} \\ 2C_{L0} & C_L' - C_{D0} \\ 2C_{M0}B & BC_M' \end{bmatrix} \quad (A.5d)$$

B | Laguerre Expansion Model - Training and Evaluation

The Laguerre expansion model shown in Equation (4.1) gives the aerodynamic forces for the specific wind speed used during the training to identify the coefficients $\boldsymbol{c}_{nv}$. However, in this way the model can foresee correct self-excited only for that specific wind velocity. To build a model independent from the wind speed, in the present work all the training input-output time histories have been adimensionalised, as shown in Section 3.3, respect to the speed of the stream. Then, with the trained model, the adimensional forces can be calculated and the dimensions are given back according to the specific wind speed. A flow chart of the model is shown in Figure 3.8.

The training procedure is here reported for clarity:

1. To train the model a sinusoidal input motion is imposed for each degree of freedom separately and the self-excited forces time histories are recorded.

2. Each input or output time history is adimensionalised with the used wind speed. Also the time vector of the simulation is made dimensionless.

3. The Laguerre expansion model is trained with the dimensionless time histories and a set of $\boldsymbol{C}$ coefficients is identified. These coefficients are specific of the girder section tested.

4. With the identified coefficients dimensionless self-excited forces can be calculated.

5. The dimensionless forces are then made dimensional with the specific wind speed.

When the present model is converted to state-space to be coupled with the equations of motion of the system (Section 4.1), the re-dimensioning part must be included. The state-space model for the Laguerre expansion model shown in Equation (4.1) becomes, in case of vertical motion input, like is shown in Equation (B.1) , where B is the width of

the model, ρ is the air density and V is the wind speed.

$$\boldsymbol{S}_v(k+1) = \boldsymbol{A}_L\boldsymbol{S}_v(k) + \boldsymbol{B}_Ly(k+1)/B \tag{B.1a}$$

$$F_{nv}(k) = \boldsymbol{c}_{nv}\boldsymbol{S}_v(k)(\frac{1}{2}\rho BV^2) \tag{B.1b}$$

To insert the Laguerre state-space in a complete two degrees of freedom dynamic system, the matrices must be expanded as shown in Section 4.2. The system in Equation (B.2) is therefore obtained, where the matrices $\boldsymbol{U}_1$ and $\boldsymbol{U}_2$ shown in Equation (B.3) are used to give the correct dimensions to the forces.

$$\boldsymbol{X}(k+1) = \boldsymbol{A}\boldsymbol{X}(k) + \boldsymbol{B}\boldsymbol{U}_1\boldsymbol{C}\hat{\boldsymbol{S}}(k) \tag{B.2a}$$

$$\hat{\boldsymbol{S}}(k+1) = \hat{\boldsymbol{A}}_L\hat{\boldsymbol{S}}(k) + \begin{bmatrix} \hat{\boldsymbol{B}}_L\boldsymbol{U}_2 & \boldsymbol{0} \end{bmatrix} \boldsymbol{X}(k+1) \tag{B.2b}$$

$$\boldsymbol{U}_1 = \frac{1}{2}\rho V^2 \begin{bmatrix} B & 0 \\ 0 & B^2 \end{bmatrix}, \boldsymbol{U}_2 = \begin{bmatrix} \frac{1}{B} & 0 \\ 0 & 1 \end{bmatrix} \tag{B.3}$$

Finally, the system in Equation (B.2) is rewritten in correct state-space form as in Equation (B.4).

$$\begin{bmatrix} \boldsymbol{X}(k+1) \\ \hat{\boldsymbol{S}}(k+1) \end{bmatrix} = \begin{bmatrix} \boldsymbol{A} & \boldsymbol{B}\boldsymbol{U}_1\boldsymbol{C} \\ \begin{bmatrix} \hat{\boldsymbol{B}}_L\boldsymbol{U}_2 & \boldsymbol{0} \end{bmatrix} \boldsymbol{A} & \hat{\boldsymbol{A}}_L + \begin{bmatrix} \hat{\boldsymbol{B}}_L & \boldsymbol{0} \end{bmatrix} \boldsymbol{B}\boldsymbol{C} \end{bmatrix} \begin{bmatrix} \boldsymbol{X}(k) \\ \hat{\boldsymbol{S}}(k) \end{bmatrix} \tag{B.4}$$

With the obtained system, once the model is trained for a specific section, its dynamic behaviour can be obtained for any wind velocity inside the identified range.

C | Aerodynamic Derivatives Notation

Aerodynamic derivatives are used to express self-excited aerodynamic forces when the reduced velocity V^* is to low to use the Quasi Steady Theory. They are also function of the external geometry of the girder and need to be determined experimentally by wind tunnel tests. There are different possible notations to give a theoretical formulation for the ADs. Here it is presented the comparison between the Scanlan's notation used in this paper and another notation commonly used in Politecnico di Milano.

C.1. Scanlan's notation

The self-excited forces per unit length, drag F_D, lift F_L and moment F_M acting on bridge decks are expressed through the use of flutter derivatives P^*_{1-6}, H^*_{1-6}, A^*_{1-6}. Assuming harmonic vibrations at a frequency f, and using the Scanlan's notation (see [17]), the self-excited wind loads on the structure are given by:

$$F_L = \frac{1}{2}\rho V^2 B \left((2\pi f)H_1^* \frac{\dot{z}}{V} + (2\pi f)H_2^* \frac{B\dot{\theta}}{V} + (2\pi f)^2 H_3^* \theta + (2\pi f)^2 H_4^* \frac{z}{B} + (2\pi f)H_5^* \frac{\dot{y}}{V} + (2\pi f)^2 H_6^* \frac{y}{B} \right)$$

$$F_M = \frac{1}{2}\rho V^2 B \left((2\pi f)A_1^* \frac{\dot{z}}{V} + (2\pi f)A_2^* \frac{B\dot{\theta}}{V} + (2\pi f)^2 A_3^* \theta + (2\pi f)^2 A_4^* \frac{z}{B} + (2\pi f)A_5^* \frac{\dot{y}}{V} + (2\pi f)^2 A_6^* \frac{y}{B} \right)$$

$$F_D = \frac{1}{2}\rho V^2 B \left((2\pi f)P_5^* \frac{\dot{z}}{V} + (2\pi f)P_2^* \frac{B\dot{\theta}}{V} + (2\pi f)^2 P_3^* \theta + (2\pi f)^2 P_6^* \frac{z}{B} + (2\pi f)P_1^* \frac{\dot{y}}{V} + (2\pi f)^2 P_4^* \frac{y}{B} \right)$$

$$(C.1)$$

Where H_i^*, A_i^* and P_i^* with $i \in [1-6]$ are aerodynamic derivatives for lift force, pitching moment and drag force respectively.

C.2.   Polimi notation

The self-excited forces per unit length, drag F_D, lift F_L and moment F_M acting on bridge decks are expressed through the use of flutter derivatives p^*_{1-6}, h^*_{1-6}, a^*_{1-6}. Assuming harmonic vibrations at a frequency f, the self-excited wind loads on the structure can be given by:

$$
F_L = \frac{1}{2}\rho V^2 B \left(-h^*_1 \frac{\dot{z}}{V} - h^*_2 \frac{B\dot{\theta}}{V} + h^*_3 \theta + \frac{2\pi^3}{V^{*2}} h^*_4 \frac{z}{B} - h^*_5 \frac{\dot{y}}{V} + \frac{2\pi^3}{V^{*2}} h^*_6 \frac{y}{B} \right)
$$

$$
F_M = \frac{1}{2}\rho V^2 B \left(-a^*_1 \frac{\dot{z}}{V} - a^*_2 \frac{B\dot{\theta}}{V} + a^*_3 \theta + \frac{2\pi^3}{V^{*2}} a^*_4 \frac{z}{B} - a^*_5 \frac{\dot{y}}{V} + \frac{2\pi^3}{V^{*2}} a^*_6 \frac{y}{B} \right) \qquad \text{(C.2)}
$$

$$
F_D = \frac{1}{2}\rho V^2 B \left(-p^*_1 \frac{\dot{z}}{V} - p^*_2 \frac{B\dot{\theta}}{V} + p^*_3 \theta + \frac{2\pi^3}{V^{*2}} p^*_4 \frac{z}{B} - p^*_5 \frac{\dot{y}}{V} + \frac{2\pi^3}{V^{*2}} p^*_6 \frac{y}{B} \right)
$$

Where V is the mean wind velocity and $V^* = \frac{V}{\omega B}$ is the reduced velocity of motion. Here h^*_i, a^*_i and p^*_i with $i \in [1-6]$ are aerodynamic derivatives for lift force, pitching moment and drag force respectively.

C.3.   Main differences between formulations

The two formulations are equivalent in practice. The first difference is how the ADs relative to drag are associated to the velocity/displacement:
Polimi:

- p^*_1 and p^*_4 are referred to the vertical velocity/displacement

- p^*_5 and p^*_6 are referred to the lateral velocity/displacement

Scanlan:

- P^*_1 and P^*_4 are referred to the lateral velocity/displacement

- P^*_5 and P^*_6 are referred to the vertical velocity/displacement

Furthermore, there is a difference of a factor function of the reduced velocity, as shown in Equation (C.3), between the two formulations.

$$
\begin{aligned}
h_1^* &= -\frac{2\pi}{V^*}H_1^*, \quad h_2^* = -\frac{2\pi}{V^*}H_2^*, \quad h_5^* = -\frac{2\pi}{V^*}H_5^*, \\
h_4^* &= \frac{2}{\pi}H_4^*, \quad h_3^* = \left(\frac{2\pi}{V^*}\right)^2 H_3^*, \quad h_6^* = \frac{2}{\pi}H_6^*, \\
a_1^* &= -\frac{2\pi}{V^*}A_1^*, \quad a_2^* = -\frac{2\pi}{V^*}A_2^*, \quad a_5^* = -\frac{2\pi}{V^*}A_5^*, \\
a_4^* &= \frac{2}{\pi}A_4^*, \quad a_3^* = \left(\frac{2\pi}{V^*}\right)^2 A_3^*, \quad a_6^* = \frac{2}{\pi}A_6^*, \\
p_1^* &= -\frac{2\pi}{V^*}P_1^*, \quad p_2^* = -\frac{2\pi}{V^*}P_2^*, \quad p_5^* = -\frac{2\pi}{V^*}P_5^*, \\
p_4^* &= \frac{2}{\pi}P_4^*, \quad p_3^* = \left(\frac{2\pi}{V^*}\right)^2 P_3^*, \quad p_6^* = \frac{2}{\pi}P_6^*
\end{aligned}
\tag{C.3}
$$

List of Figures

List of Tables

Acknowledgements

This work is the dissertation for the M. Sc. degree in Mechanical Engineering at Politecnico di Milano. It is the conclusion of 30 weeks of work executed in collaboration with the Norwegian University of Science and Technology (NTNU).

I would like to thank my advisor Prof. Tommaso Argentini at PoliMi and my co-advisor Prof. Ole Andre Øiseth at NTNU, for their guidance and feedback throughout all the work. I wish for any future Master's student to be as lucky as I have been having them as advisors. I would like to thank Postdoc Øyvind Wiig Petersen for his advice and support during the definition of the model.

Moreover, I wish to thank all my family and friends for their support during these intense years that lead to this achievement. In particular, Daniela and Giovanni always believed in me and encouraged me to aim high.

A final thank goes to Laura.

Her tireless cheering and endless patience gave me the motivation and energy to achieve this goal.